DEGRADATION OF METHYLENE BLUE WITH CU(II)-QUINOLINE COMPLEX IMMOBILIZED ON SILICA SUPPORT AS A PHOTO-FENTON-LIKE CATALYST

TEERAWAT KHUDKHAM

A Thesis Submitted to the Graduate School of Naresuan University
in Partial Fulfillment of the Requirements
for the Master of Science in Chemistry (Type A 2)
2022

DEGRADATION OF METHYLENE BLUE WITH CU(II)-QUINOLINE COMPLEX IMMOBILIZED ON SILICA SUPPORT AS A PHOTO-FENTON-LIKE CATALYST

TEERAWAT KHUDKHAM

A Thesis Submitted to the Graduate School of Naresuan University
in Partial Fulfillment of the Requirements
for the Master of Science in Chemistry (Type A 2)
2022

Thesis entitled "Degradation of methylene blue with Cu(II)-quinoline complex immobilized on silica support as a photo-Fenton-like catalyst"

By TEERAWAT KHUDKHAM

has been approved by the Graduate School as partial fulfillment of the requirements for the Master of Science in Chemistry (Type A 2) of Naresuan University

Oral Defense Committee

..... Chair
(Associate Professor Weekit Sirisaksoontorn, Ph.D.)

..... Advisor
(Assistant Professor Ratanon Chotima, Ph.D.)

..... Co Advisor
(Associate Professor Duangdao Channei, Ph.D.)

..... Internal Examiner
(Assistant Professor Bussaba Pinchaipat, Ph.D.)

Approved

.....
(Associate Professor Krongkarn Chootip, Ph.D.)
Dean of the Graduate School

Title	DEGRADATION OF METHYLENE BLUE WITH CU(II)-QUINOLINE COMPLEX IMMOBILIZED ON SILICA SUPPORT AS A PHOTO-FENTON-LIKE CATALYST
Author	TEERAWAT KHUDKHAM
Advisor	Assistant Professor Ratanon Chotima, Ph.D.
Co-Advisor	Associate Professor Duangdao Channei, Ph.D.
Academic Paper	M.S. Thesis in Chemistry (Type A 2), Naresuan University, 2022
Keywords	Schiff base, Copper, Quinoline, Immobilization, Silica, Methylene Blue, Photo-Fenton-like reaction, Photocatalytic degradation

ABSTRACT

A Cu(II)-quinoline complex immobilized on silica support was prepared to enhance the degradation of dyes. Mesoporous silica functionalized with this Cu(II) complex was turned into a photo-Fenton-like catalyst. Various techniques were used to characterize the resulting material and the catalytic activity was determined by the degradation of methylene blue (MB) under UV light irradiation. The Cu(II) ion was successfully coordinated to the quinoline ligand on a silica support. The dye degradation investigation has shown that 95% of the dye was degraded in 2.5 h. The active radical species involved in the reaction were $OH^{\bullet}$ and $O_2^{\bullet-}$, suggesting that a peroxo complex intermediate might be formed during the degradation processes.

ACKNOWLEDGEMENTS

I wish to express gratitude to my advisor, Assistant Professor Ratanon Chotima, Ph.D. and co-advisor, Associate Professor, Duangdao Channei, Ph.D. for their invaluable guidance and unwavering support throughout the duration of my graduate study and research.

Without the financial support of Promotion of Science and Technology Talents Project (DPST) which offered me a scholarship for graduate studies, this work would not have been possible. I would like to thank all lecturers in Department of Chemistry for teaching me all Chemistry topics and granting me that rare opportunity.

I would like to thank scientists in Science Lab Center, Faculty of Science, Naresuan University for their help with the instruments in this work.

Finally, special thanks are extended to my family for their encouragement and financial assistance and I would like to thank my friends for their support and unconditional friendship

TEERAWAT KHUDKHAM

TABLE OF CONTENTS

Page

LIST OF TABLE

Page

LIST OF FIGURES

Page

LIST OF SCHEMES

Page

CHAPTER I

INTRODUCTION

1. Synthetic Dyes

A dye is usually an organic or inorganic compound giving color to substrates such as food, fabric, textile cloth, paper, and plastic [1]. The color of a dye applied in an aqueous solution depends on its structure to absorb light within a visible region (400-700 nm) [2]. There is a limit of natural colorant obtained from plants, animals, and minerals, therefore a synthetic dye becomes mandatory. The synthetic dye is produced in a huge production and a large number of colorants. There are different names in a single dye. For example, there are three names of Rose Red dye viz. Rosaniline, Magenta, and Fuchsine. The Color Index (C.I.) is applied to avoid this difficulty. It consists of a generic name, and a chemical number described by application type, color, and identifying number. Reactive red 22, which is a member of azo dyes, is given as an example to illustrate the color index classification (**Scheme 1**) [3].

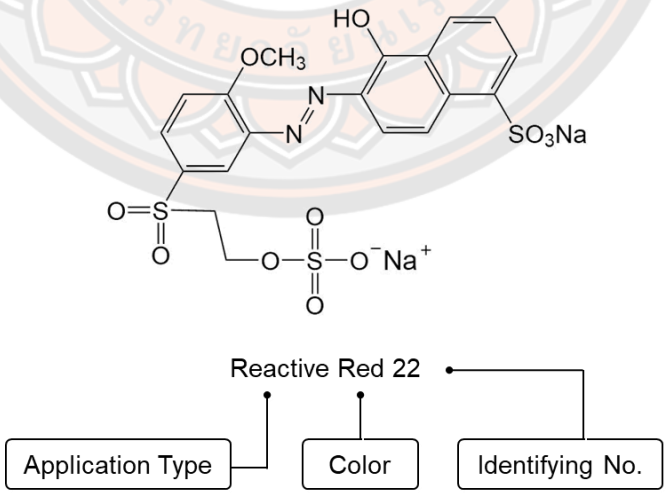

Scheme 1 The representative example for the color index classification

The worldwide production of dyes is over 700,000 tons per year [4-6]. Over 10,000 dyes are used in textile manufacturing. Unfortunately, not all dyes are fixed on the fabrics. There is always a portion of these dyes that remains unfixed and gets washed out. The investigation reported that 10-12% of synthetic dyes were lost during synthesis and processing operation [7-10]. Those dyes enter into water and cause chemical contamination. Some of the contaminations are non-biodegradable and carcinogenic and pose a major threat to health and the environment. However, there is no proof to inform that most of the dyestuffs at the present used in textile dyeing are risky to human health at the levels of exposure that workers generally face in the factories. They are likely to be health hazards with long-term or accidental over-exposure. Therefore, the impact of dyes discharged into the environment has been widely studied. One of the most concern in environmental and health effects is azo dyes [11, 12].

Azo dyes (-N=N-) are an important class of synthetic compounds used as a coloring agent in the dyeing industry. 70% of all organic dyes produced in the world are these azo dyes. The dyeing process is successful due to its simple synthetic procedure, great diversity, and moderately high colorfastness to light and water. However, the presence of these dyes in the ecosystem causes serious environmental and health concerns. The Ecological and Toxicological Association of the Dyestuffs Manufacturing Industry (ETAD) was founded to minimize the adverse impact of organic colorants. According to the survey, the lethal dose (LD) of over 4000 dyes was estimated. Around 90% of them have LD_{50} (Lethal Dose) values greater than 2 g kg^{-1} [13]. Thus, the acute toxicity of azo dyes is rather low, but it still causes a variety of other chronic effects. There was the report showed that the toxicity was generally not because of the dye itself, but its degradation products [14]. The azo linkage is labile in the presence of Azoreductase, which is found in various microorganisms and humans. This results in the release of constituent aromatic amines, which are very high levels of acute and chronic toxicity, and carcinogenicity (**Scheme 2**).

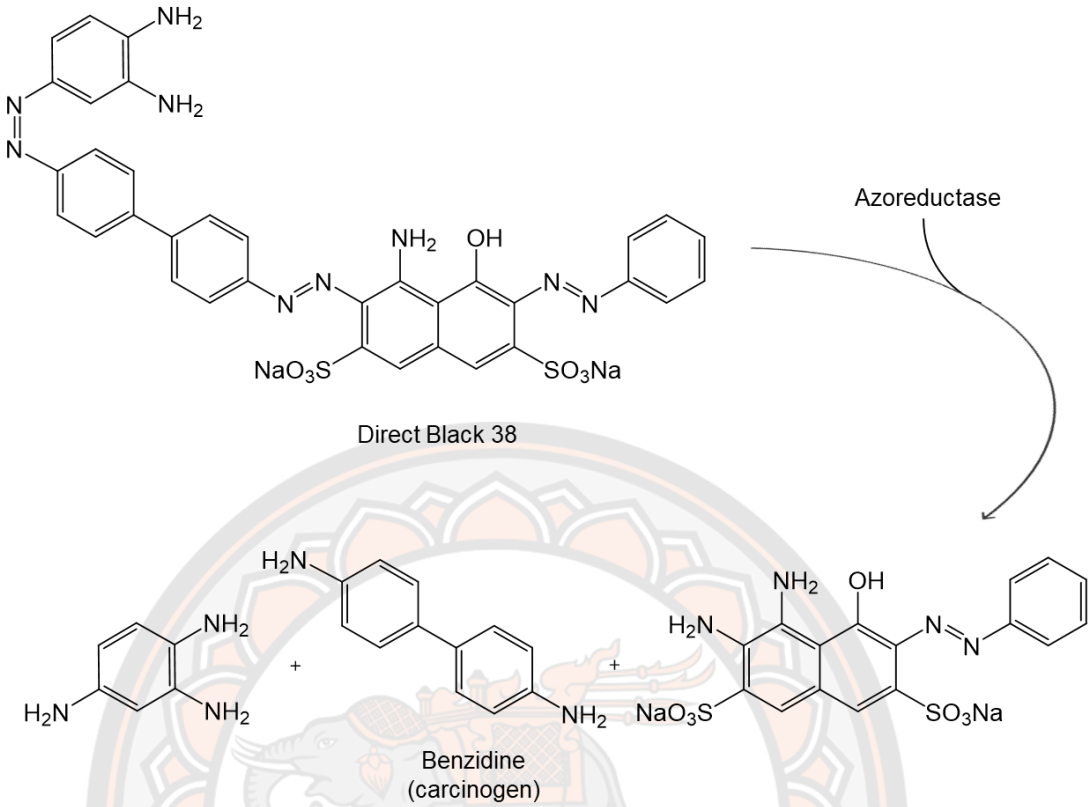

Scheme 2 A typical Azoreductase-catalyzed reaction

2. Wastewater Treatment Processes

The technologies used in the removal of contaminants include physical, chemical, and biological processes. However, drawbacks and limitations are found in each approach differently. For example, high temperatures for calcination and regeneration of catalysts are required in a physical process. There is a cost of reagents used in a chemical process and some of them are unsustainable. In a biological process, microbiological or enzymatic decomposition can occur [15]. Consequently, it is highly demanded to develop an efficient technology for the decontamination of dyes in wastewater.

2.1 Advanced Oxidation Processes (AOPs)

In recent years, AOPs have been studied as a promising organic wastewater treatment method. The AOPs are reactions based on the in-situ generation of hydroxyl

radicals ($HO^{\bullet}$), which have a strong oxidation capacity (standard potential = 2.8 V versus standard hydrogen electrode) [16, 17]. The processes are an effective tool to degrade a wide range of organic pollutants [18, 19]. Most of them are quickly and non-selectively oxidized by $HO^{\bullet}$ to smaller organics or completely mineralized to carbon dioxide (CO_2) and water (H_2O) [20-23]. Many organic wastewater treatment methods are based on $HO^{\bullet}$ generation can be called AOPs. The processes are operated by additional physical phenomena such as UV photolysis, ozonation, electrochemical treatment, ultrasound irradiation, non-thermal plasma, ɣ-ray, and electron beam irradiation. The UV photolysis includes Fenton-based reagent (Fe^{2+}/H_2O_2), ozonation (O_3), O_3/H_2O_2, H_2O_2/UV, TiO_2/UV, *etc.* [24-29]. The mentioned processes are listed in **Table 1** [30].

Table 1 Summary of AOPs involving in the generation of HO•

Type of AOPs	Brief description of overall process and operating conditions	Typical examples and key reaction pathways
UV Photolysis (direct & indirect)	UV photons (150-400 nm) irradiate aqueous solutions with high fluences (500-4000 mJ/cm^2). Homogeneous and heterogeneous chemical species present in water then absorb the incident UV light and undergo photo-transformation reactions to generate free hydroxyl radicals.	<u>UV/Water Photolysis</u> $H_2O + h\nu\ (<190\ nm) \rightarrow H^{\bullet} + HO^{\bullet}$ <u>UV/Ozone</u> $O_3 + H_2O + h\nu\ (254\ nm) \rightarrow 2HO^{\bullet} + O_2$ <u>UV/H_2O_2</u> $H_2O_2 + h\nu\ (254\ nm) \rightarrow 2HO^{\bullet}$ <u>UV/Fenton</u> $Fe^{3+} + H_2O_2 + h\nu \rightarrow Fe^{2+} + OH^{\bullet} + HO^{-}$ <u>TiO_2</u> $TiO_2 + h\nu\ (>300\ nm) \rightarrow e^{-}_{cb} + h^{+}_{vb}$ $2e^{-}_{cb} + O_2 + 2H^{+} \rightarrow H_2O_2$ $e^{-}_{cb} + H_2O_2 \rightarrow HO^{\bullet} + HO^{-}$ $h^{+}_{vb} + HO^{-} \rightarrow HO^{\bullet}$

Table 1 cont.

Type of AOPs	Brief description of overall process and operating conditions	Typical examples and key reaction pathways
Ozonation	Using high voltage alternating current (6-20 kV) across a dielectric discharge gap containing pure oxygen or dry air, O_2 molecules are dissociated into oxygen atoms to form ozone (O_3). This ozone gas stream is bubbled into water for decomposition into free hydroxyl radical	Ozone/H_2O_2 $2O_3 + H_2O_2 \rightarrow 2HO^{\bullet} + 3O_2$
Electrochemical Treatment	Using indirect and/or direct anodic reactions, electrical energy vector drives the in-situ formation of oxidants.	Anodic Oxidation $H_2O_2 \rightarrow H^+ + HO^{\bullet}$
Ultrasound (US) Irradiation	High frequency sound waves (20 kHz - 1 MHz) generate transient or stable acoustic cavitation in water solution. The cavitation involves formation of pressure bubbles with inducing thermal dissociation of water into hydroxyl radicals.	US/Hydrogen Peroxide $H_2O_2 +))) \rightarrow 2HO^{\bullet}$
Non-thermal Plasma	An electric discharge in water initiates collisions of charged particles and excitation-ionization of neutral molecules. This generates a non-thermal plasma containing energetic electrons (e^{-*}) and radicals.	Electrical Discharge $\rightarrow e^{-*}$ $H_2O + e^{-*} \rightarrow HO^{\bullet} + H^{\bullet} + e^-$
ɣ-Ray and Electron Beam Irradiation	Using ionizing radiation from radioactive ɣ-sources (^{60}Co) or particle accelerators, radiolysis of water produces both reducing and oxidizing radical species.	$H_2O \text{—}\wwvy\rightarrow H^*, HO^{\bullet}, e^-, H_2, H_2O_2, H_3O^+, HO^-$

One of the most frequently used AOPs is the Fenton reaction where Fe^{2+} is used as the catalyst and H_2O_2 as the oxidant. In general, the $HO^{\bullet}$ can be generated through the catalytic decomposition of H_2O_2. Its advantages were reported as high performance and simplicity by operating at room temperature and atmospheric pressure [31, 32]. Moreover, the reaction is non-toxicity and H_2O_2 can be broken down into environmentally safe like H_2O and O_2.

2.2 Fenton reaction

Fenton's reaction was developed in the 1890s and named after Henry John Horstman Fenton. In the presence of Fe^{2+} ions and H_2O_2 in an acidic solution, it can produce radicals without additional energy. The reaction sequence is given in Eq. (1)-(5) [33].

$$Fe^{2+} + H_2O_2 \longrightarrow FeOH^{2+} + {}^{\bullet}OH \text{ (or } Fe^{3+} + {}^{\bullet}OH + {}^{-}OH) \quad (1)$$

$$Fe^{2+} + {}^{\bullet}OH \longrightarrow FeOH^{2+} \text{ (or } Fe^{3+} + {}^{-}OH) \quad (2)$$

$$H_2O_2 + {}^{\bullet}OH \longrightarrow {}^{\bullet}OH_2 + H_2O \quad (3)$$

$$FeOH^{2+} + {}^{\bullet}OH_2/O_2^{\bullet-} \longrightarrow Fe^{3+} + O_2 + H_2O/OH^{-} \quad (4)$$

$$FeOH^{2+} + H_2O_2 \longrightarrow Fe^{2+} + H_2O + {}^{\bullet}OH_2 \quad (5)$$

The Fenton reaction and its modification have been used for decomposing various dyes [34]. However, Fenton's reagent can work only in a narrow acidic pH range (pH 2-4) and is not able to completely decompose some dyes [35]. These drawbacks limited its applications.

To overcome these disadvantages, the enhancement of the Fenton reaction has been attracted attention. There were reports found that Fe^{2+} was replaced by the others, such as iron (Fe^{3+}), chromium (Cr^{3+}/Cr^{6+}), cobalt (Co^{2+}/Co^{3+}), and copper (Cu^{+}/Cu^{2+}) [36-38]. Those reactions were performed as hetero- and homogeneous catalysts. Therefore, the reactions that other metal ions, instead of Fe^{2+}, with H_2O_2 are Fenton-like reactions. The key equations of $HO^{\bullet}$ generation using Fe^{3+} are given in Eq. (6)-(8) [39].

$$Fe^{3+} + H_2O_2 \rightarrow [Fe^{III}O_2H]^{2+} + H^+ \quad (6)$$

$$[Fe^{III}O_2H]^{2+} \rightarrow Fe^{2+} + HO_2^{\bullet} \quad (7)$$

$$[Fe^{III}O_2H]^{2+} \rightarrow [Fe^{IV}O]^{2+} + HO^{\bullet} \quad (8)$$

Furthermore, the incorporation of light irradiation into the basic Fenton process can dramatically increase the $^{\bullet}OH$ generation. The reactions correspond to the photo-Fenton/Fenton-like reactions. The reaction sequence is given in Eq. (9)-(16) [30].

Photo-Fenton (UV or Solar light);

$$Fe^{3+} + H_2O_2 + h\nu \rightarrow Fe^{2+} + OH^{\bullet} + HO^- \quad (9)$$

$$Fe^{2+} + H_2O_2 \rightarrow Fe^{3+} + OH^{\bullet} + HO^- \quad (10)$$

$$H_2O_2 + h\nu \rightarrow 2OH^{\bullet} \quad (11)$$

Photo-Fenton (Visible light);

$$H_2O_2 + h\nu\ (< 310\ nm) \rightarrow 2HO^{\bullet} \quad (12)$$

$$Fe(OH)^{2+} + h\nu\ (< 580\ nm) \rightarrow Fe^{2+} + HO^{\bullet} \quad (13)$$

$$Dye + h\nu \rightarrow Dye^* \quad (14)$$

$$Fe^{3+} + Dye^* \rightarrow Fe^{2+} + Dye^{\bullet+} \quad (15)$$

$$Fe^{2+} + H_2O_2 \rightarrow Fe^{3+} + OH^{\bullet} + HO^- \quad (16)$$

As seen in the given equations, the sources of light are UV or Solar light and visible light. The use is dependent on the proper energy to the Fenton catalyst. For example, visible light at 580 nm was used in the photo-Fe^{3+}-H_2O_2 system (Eq. (13)). The photo-generated intermediates, such as Fe^{2+}, Fe^{3+}, Dye^*, and $Dye^{\bullet+}$, can enter the Fenton system and simultaneously produce more $HO^{\bullet}$. It finally improves the degradation rate of the organic pollutants.

For the study of Fenton-based reactions mentioned above, significant effects on oxidation performance including pH, H_2O_2 dosage, catalyst loading, and reaction temperature have been widely studied. In addition, various organic compounds were chosen as selected contaminants such as dyes, drugs, and pesticides [36, 37, 40]. The study of concentration range was always from hundreds of µg/L to hundreds of mg/L. The complete decomposition of them was found in a short reaction time [41].

3. Photo-Fenton-like Catalysts

The photo-Fenton-like catalysts are the catalyst which is facilitated by photochemistry to perform in Fenton reaction. The role of photochemistry is to provide energy of UV and/or visible light to enhance the formation of $HO^{\bullet}$. This is followed by the huge catalytic capacity. As a result, the other parameters involved in the catalysis such as catalyst loading and H_2O_2 dosage are reduced. The performance in the Fenton reaction is depended on the natural form of each catalyst, which can be a homogeneous and heterogeneous system. The main difference between those processes is the positions of catalytic reactions. In the homogeneous system, the catalysis process is performed in the whole liquid phase (**Scheme 3a**). On the other hand, a heterogeneous system always occurs on the surface of the catalyst (**Scheme 3b**). The diffusion and adsorption processes of H_2O_2 and other reactants to the surface of the catalyst could be significant for the catalysis process.

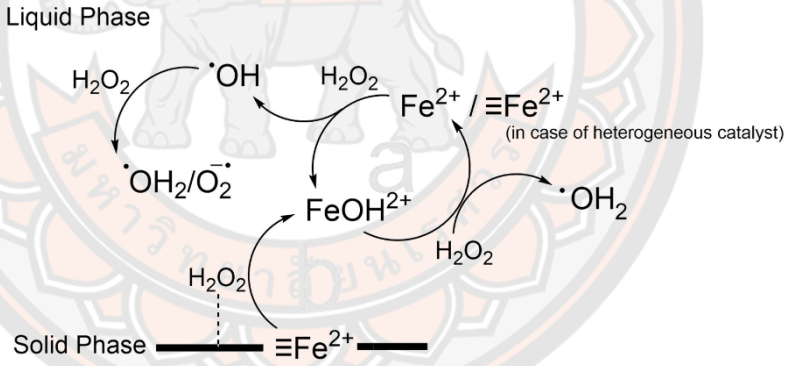

Scheme 3 (a) Homogeneous and (b) heterogeneous Fenton reactions

There still are some disadvantages in homogeneous and heterogeneous Fenton-based catalysts. The finding of the practical catalyst has been focused on. Basically, multiple oxidation states should be allowed for the ideal catalyst. The active species with a specific oxidation state can be easily regenerated from an inactive form through a simple redox cycle. For example, cerium is a rare earth element. The oxidation states of +3 and +4 are exhibited in an aqueous solution. While Ce^{3+} form is a strong reducing agent and easily oxidized by O_2 in alkaline

conditions, Ce^{4+} species is a strong oxidant under acidic conditions. Thus, cerium can easily cycle between the Ce^{3+} and Ce^{4+} oxidation states. The use of Ce^{4+}/Ce^{3+} redox cycle is applied as a Fenton-like catalyst. The generation of $HO^{\bullet}$ is given in Eq. (19)-(20) [42].

$$Ce^{3+} + H_2O_2 \rightarrow Ce^{4+} + HO^- + HO^{\bullet} \quad (19)$$

$$Ce^{4+} + H_2O_2 \rightarrow Ce^{3+} + HO_2^{\bullet} + H^+ \quad (20)$$

The nonferrous metal ions can perform hydrogen peroxide decomposition. It results in the production of reactive oxygen species in a unique environment. Besides the use of cerium, the active species with a specific oxidation state has been focused to replace iron, including chromium (Cr^{3+}/Cr^{6+}), cobalt (Co^{2+}/Co^{3+}), manganese (Mn^{2+}/Mn^{4+}), copper (Cu^{+}/Cu^{2+}), and ruthenium (Ru^{3+}, Ru^{4+}). The proposed key step for the generation of $HO^{\bullet}$ is displayed in **Scheme 4** [30].

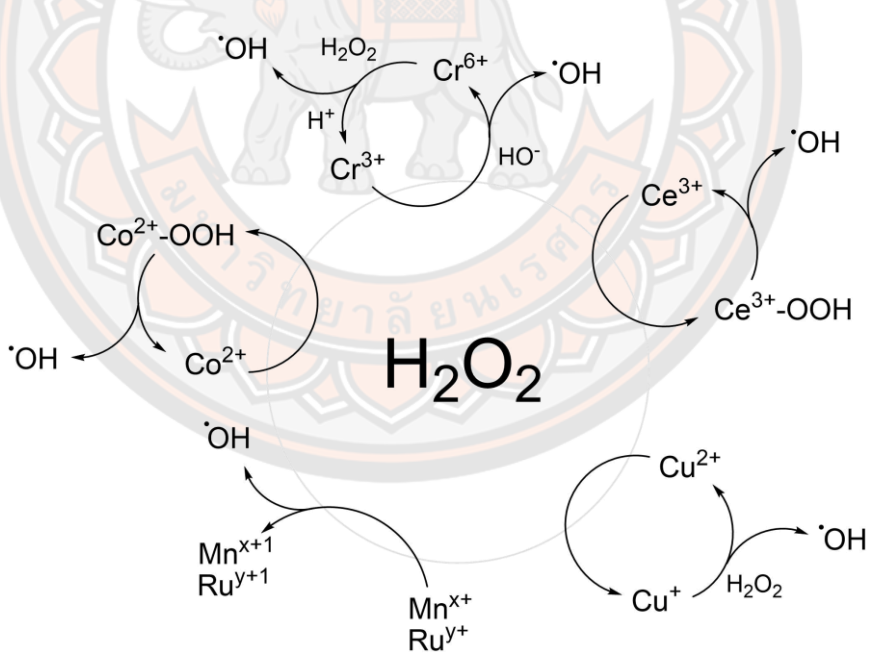

Scheme 4 The redox reactions between H_2O_2 and various nonferrous metal ions

Among these, the Cu-based Fenton catalyst seems to be practical in wastewater treatment due to the stable oxidation state of Cu^{2+}. Furthermore, there are only two uptakes of electrons required in the redox process for the generation of ROS.

3.1 Copper

Copper is a chemical element with the symbol Cu and is in group 11 of the periodic table. This element is a transition metal because there is an incompletely filled d orbital in their ion forms (Cu^{+} and Cu^{2+}). Copper is also known as an essential trace element in living systems. Its ion forms are presented in several important enzymes involving in a variety of biological processes, such as photosynthesis, electron transport, and cell wall metabolism [43, 44].

The ions are named cuprous or cupric based on the electronic configuration where cuprous is Cu^{+} (d^{10}), whereas cupric is Cu^{2+} (d^{9}). However, those ions can be changed in their oxidation states by an electron-transfer reaction. The reaction is allowed when there is an additional chemical or energy from the surrounding system [45]. The transformation between the oxidation state of Cu^{+} and Cu^{2+} plays a critical role in the speciation, transport, and bioavailability [46].

One of the important roles of the redox of Cu is the H_2O_2 decomposition to generate $HO^{\bullet}$ and/or another ROS for a balance of free radicals and antioxidants in the body. The copper is bound strongly to serum albumin or incorporated into ceruloplasmin with approximately 80 mg Cu present in an average adult [47]. However, the copper in excess can be potentially toxic to organisms. Especially in its free hydrated form (i.e., Cu^{2+}), it can be harmful to membrane permeability, chromatin structure, protein synthesis, and various enzyme activities. Most importantly, the oxidative stress in the body is caused by the reaction of Cu with hydrogen peroxide in the cells of organisms from a by-product of oxygen metabolism. It can lead to cell and tissue damage (**Scheme 5**) [48].

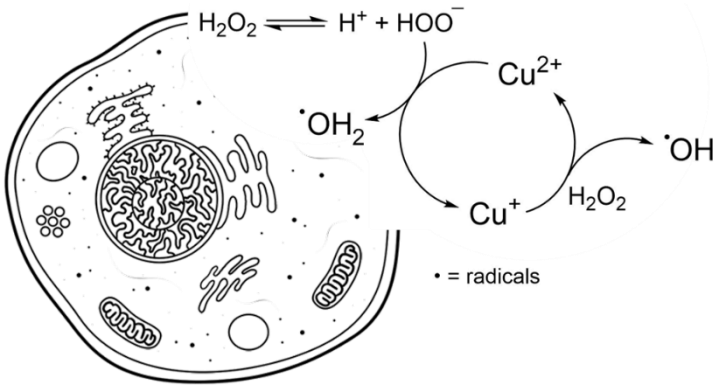

Scheme 5 Cell and tissue damage in the oxidative stress

3.2 Redox chemistry of Cu in Fenton-like based reaction

Redox properties of copper are like iron. The oxidation states can be easily switched by reacting with H_2O_2 (Eq. (21)-(22)).

$$Cu^{2+} + H_2O_2 \rightarrow Cu^{+} + HO^{\bullet} + HO^{-} \quad (k = 4.6 \times 10^{2}\ M^{-1}s^{-1}) \quad (21)$$

$$Cu^{+} + H_2O_2 \rightarrow Cu^{2+} + HO^{\bullet} + HO^{-} \quad (k = 1.0 \times 10^{2}\ M^{-1}s^{-1}) \quad (22)$$

The hydrolyzed complex with the most stable oxidation state, $Cu(OH)_2$ for Cu^{2+} and $FeOH(H_2O)^{2+}$ for Fe^{3+} performed in homogeneous catalysis. However, there is a difference in aqueous solubility. While, the iron aquo complex $[Fe(H_2O)_6]^{3+}$ is insoluble at pH >5, the copper complex $[Cu(H_2O)_6]^{2+}$ is still soluble in neutral pH conditions [49]. Therefore, the Cu^{2+}/H_2O_2 system works over a broader pH range, compared to the Fe^{3+}/H_2O_2 which only works in the acidic condition.

Nevertheless, the performance of the copper is inhibited by O_2 since Cu^{+} is oxidized by oxygen to Cu^{2+} under near-neutral and acidic conditions (Eq. (23)) [50]. As a result, it reduces the effective Cu^{+} available to react with H_2O_2. Thus, the Fenton systems using Cu^{2+} catalyst require a larger excess of H_2O_2, compared to Fe^{3+}-based systems [51].

$$4Cu^{+} + 4H^{+} + O_2 \rightarrow 4Cu^{2+} + H_2O \quad (23)$$

There is considerable interest in the development of copper in the Fenton-like catalysts. Generally, there are two pathways of hydroxyl radicals generation described by the free radical pathway and the complex pathway, as shown in Eq. (24)-(27) and (28)-(30), respectively [52-54].

Free radical pathway;

$$H_2O_2 \rightleftharpoons H^+ + HOO^- \quad (24)$$

$$Cu^{2+} + HOO^- \rightarrow Cu^+ + HO_2^{\bullet} \quad (25)$$

$$HO_2^{\bullet} \rightarrow H^+ + O_2^{\bullet-} \quad (26)$$

$$Cu^+ + H_2O_2 \rightarrow Cu^{2+} + HO^{\bullet} + HO^- \quad (27)$$

Complex pathway;

$$Cu^{2+}L + HOO^- \rightarrow Cu^{2+}L(HOO) \quad (28)$$

$$Cu^{2+}L(OOH) \rightarrow Cu^{+}L(HOO^{\bullet}) \quad (29)$$

$$Cu^{+}L(HOO^{\bullet}) + H_2O_2 \rightarrow Cu^{2+}L + O_2 + H_2O + HO^- \quad (30)$$

The Cu-based Fenton processes which perform the free radical pathway are involved cuprous copper (Cu^+), cupric copper (Cu^{2+}), zero-valent copper (Cu^0), and copper composites. On the other hand, the processes that perform the complex pathway are the Cu-complexes with organic and inorganic ligands (L). Interestingly, the coordination of copper ions with those ligands caused dramatically enhanced catalysis in the generation of $HO^{\bullet}$ [34, 35, 55, 56].

Furthermore, two extra reactions of the Cu-based Fenton catalyst can occur due to the existence of photo-irradiation as given in Eq. (31)-(32). The first reaction involves $Cu^{2+}L$ undergoing a photochemical reduction process. As seen in Eq. (31), the oxidation number of Cu^{2+} is reduced to Cu^+ because of the excited electron which is stimulated by the photo-irradiation ($h\nu$). It is followed by the second reaction that involves $HO^{\bullet}$ generating via an electron transfer of H_2O_2 to the Cu^+ [57].

$$Cu^{2+}L + h\nu \rightarrow Cu^+ + L^{+\bullet} \quad (31)$$

$$Cu^+ + H_2O_2 \rightarrow Cu^{2+} + HO^{\bullet} + HO^- \quad (32)$$

4. Schiff Base

Schiff base (also known as imine or azomethine functional group) is a compound with the general structure $R_2C=NR'$ ($R' \neq H$) [58]. It can be synthesized from primary amine and aldehyde compounds by a nucleophilic addition. This is followed by a condensation reaction to generate a Schiff base (**Scheme 6**).

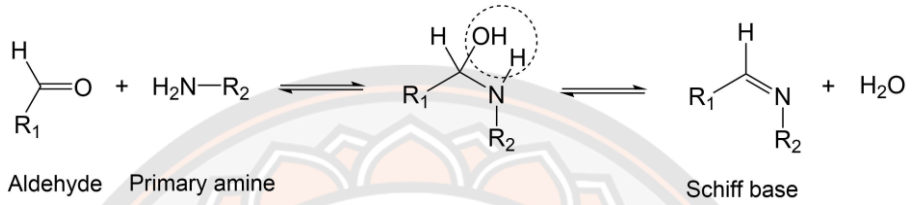

Scheme 6 The formation of Schiff base

Schiff bases were discovered and named after Hugo Schiff in 1864 [59]. Since then a variety of methods for the synthesis of imine have been described [60-64]. Schiff bases played an important role as ligands in coordination chemistry due to their convenient synthesis method and effective stabilization to metal ions.

The environment of the coordination center (R_1 and R_2) can be modified by attaching different substituents to the structure of Schiff bases. This can provide different structures and reactivities as introduced in the two basic ideas of HSAB (Hard and Soft Acids and Bases) and the chelate effect. In addition, the steric and electronic effects around the metal core can be tuned by an appropriate selection of bulky and/or electron-withdrawing or donating substituents [65]. More importantly, the designed structure is depended on the purpose required.

Many Schiff base complexes with different transition metal ions are flexible compounds. It is extensively used for industrial purposes. The broad range of biological activities and catalysis reactions of Schiff base complexes have been investigated in various areas [62, 66-68].

5. Methylene Blue

MB is a heterocyclic aromatic compound with the molecular formula ($C_{16}H_{18}ClN_3S$, $3H_2O$). The structure is displayed in **Figure 1**. The chemical name is [7-(dimethylamino)phenothiazin-3-ylidene]-dimethylazanium;chloride, as corresponding in IUPAC. It is soluble in water and has a deep blue color [69, 70].

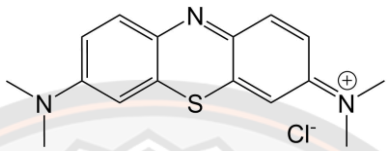

Figure 1 The chemical structure of Methylene Blue

MB is not strongly hazardous when compared to the other dyes, but various harmful effects are found on inhalation. The rise to short periods of rapid or difficult breathing produces a burning sensation, and it may cause nausea, vomiting, diarrhea, and gastritis. An accidental large dose creates abdominal and chest pain, severe headache, profuse sweating, mental confusion, painful micturition, and methemoglobinemia [71].

Historically, MB was a synthetic drug used in medicine. Robert Koch used MB as a stain for microscopic visualization of tuberculosis bacilli in 1870. After observing that bacteria were seen with MB-containing stains, Paul Ehrlich argued this might suggest a harmful effect on the microorganism. As a result, Ehrlich and Guttman applied MB to the treatment of malaria starting in 1891. MB was used as an antimalarial agent through the end of World War II by U.S. service members but not the result was not good enough [72].

Other historical applications for MB have included use as an indicator of compliance with psychiatric medications. This practice led to the observation that MB has antidepressants and other psychotropic effects. MB served as the lead compound for the development of chlorpromazine and tricyclic antidepressants [73]. Now a day, MB has become recognized to be beneficial in the treatment of toxin-induced and hereditary methemoglobinemia [74].

As a dye, MB was first developed as an aniline dye derivative for the textile industry by Heinrich Caro in 1876. MB is classified as a basic dye and named methylthioninium chloride or Basic blue 9. It is widely used for dying cotton, wool, and silk [75]. More recently, aqueous solutions of methylene blue were used as a selected dye model for a survey of degradation of various dyes because it is easy to handle and less harmful to the researchers and environment [76-80].

6. Purposes of the Study

1. To develop a new catalyst by immobilizing the Cu(II) complex with quinoline onto silica support.
2. To study catalytic efficiency in MB degradation under the selected experiment conditions including catalyst dosage, H_2O_2 concentration, MB concentration, pH, time, and UV light irradiation effect.

7. Scope of the Study

The catalyst was prepared by immobilizing the Cu(II) complex with quinoline onto a silica surface. The synthetic procedures followed the literature [81] but 8-aminoquinoline was used instead of 2-aminopyridine (2-APY). The obtained catalyst was monitored by spectroscopic techniques such as Fourier-transform infrared spectroscopy (FTIR), X-ray powder diffraction (XRD), UV-visible diffuse reflectance spectroscopy (DRS), and X-ray photoelectron spectroscopy (XPS). Besides, the catalyst was investigated in surface studies including the Brunauer-Emmett-Teller method (BET) and scanning electron microscopy (SEM). Finally, the catalytic efficiency of the prepared catalyst was determined in MB degradation under the selected experiment conditions such as catalyst dosage, H_2O_2 concentration, MB concentration, pH, time, and UV light irradiation effect.

CHAPTER II

LITERATURE REVIEWS

1. Copper in Fenton-based Catalyst for Degradation of Synthetic Dyes

The copper was used as Cu (II) complex in hydrogen peroxide decomposition for the generation of ROS as well as homogeneous and heterogeneous reactions. It has been started since the discovery of the Cu(II)/pyridine/H2O2 system in 1998 and then has been extensively studied in various ways.

Cu(II)/pyridine/H_2O_2 system was discovered by Watanabe et al. (1998) [82] in the study of lignin degradation (**Figure 2**). The phenolic and non-phenolic synthetic lignin were intensively depolymerized by Cu(II) and peroxide sources. The use of copper with pyridine ligand enhanced the decomposition of lignin by generating an active oxidant. Moreover, the radical species were demonstrated in this finding by spin trapping experiments that not hydroxyl radical, but superoxide anion is involved in the Cu(II)/pyridine/H_2O_2 system.

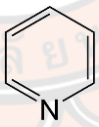

Figure 2 Chemical structure of pyridine

The Cu(II)/pyridine/H_2O_2 was firstly used in the decolorization of synthetic dyes described by Nerud F. et al. (2001) [83]. Those dyes with 1 mM were incubated with 1 mM of $CuSO_4$ solution, 2% pyridine and, peroxide sources such as H_2O_2 at 100 mM. The decolorization measured after 1 h was obtained with Phenol Red (89%), Tropaeolin 00 (58%), Evans Blue (95%), Eosin Yellowish (84%), and Poly B-411 (92%) (**Figure 3**). In addition, the pH and temperature were studied. It was found that the rate of decolorization was not affected pH in the range of 3-9 and increased with increasing temperature. Furthermore, the result was investigated using radical scavengers (thiourea and superoxide dismutase). The hydroxyl radicals are involved

in the reaction rather than superoxide anions. This result is in contrast with the finding of Watanabe T. et al.

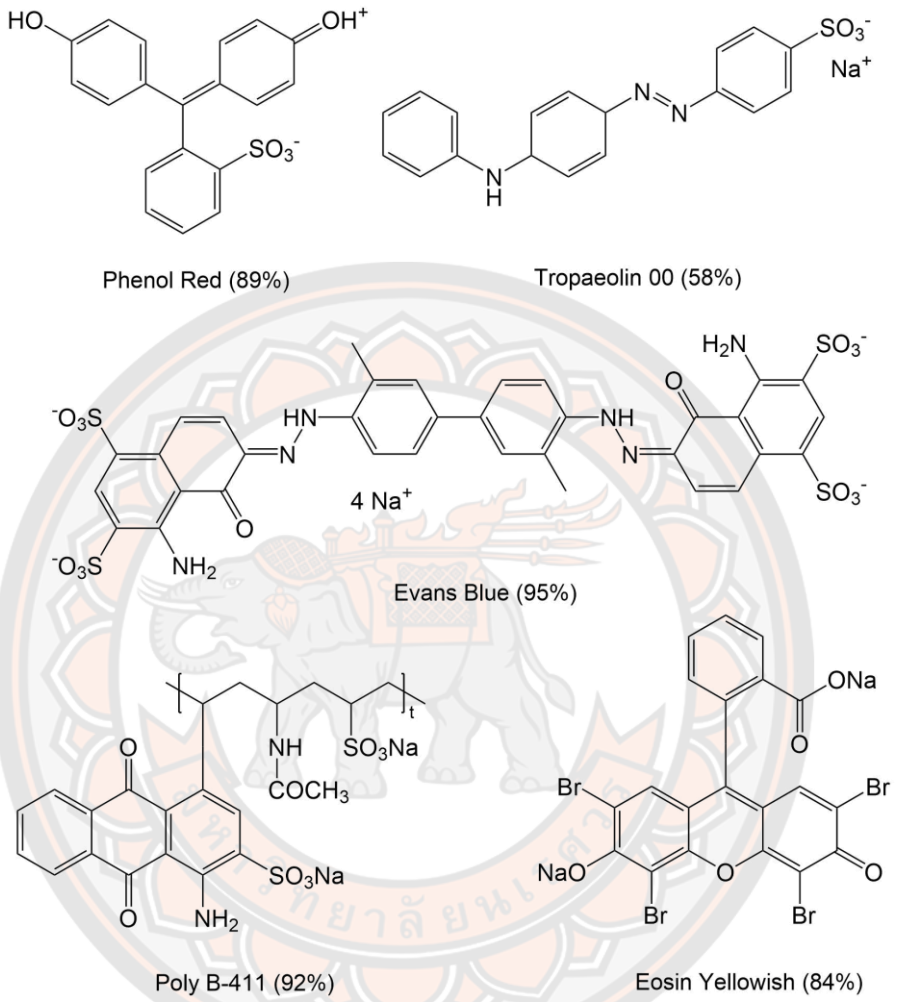

Figure 3 Chemical structures of Phenol Red, Tropaeolin 00, Evans Blue, Eosin Yellowish, and Poly B-411 with decolorization degree

Various dyes were investigated in the decolorization by Verma et al. (2004) [55]. Cu(II)-ligand complex with D-arabinono-1,4-lactone (APL) was reported to be effective in the decolorization and reduction of azo toxicity and other synthetics dyes. The incubations were performed for 24 h in the presence of 10 mM $CuSO_4$, 20 mM APL, and 80 mM H_2O_2. The decolorizations of such dyes were obtained with 100 ppm Acridine Orange (91%), Azure B (87%), Chicago Sky Blue 6B (87%), Crystal Violet (91%), Evans Blue (90%), Poly B-411 (91%), Reactive Blue 2 (88%), Reactive Blue 5 (89%), and Remazol Brilliant Blue R (87%) (**Figure 4**). In addition, the use of

APL complexes with other metals instead of Cu(II) was determined, but it led to a decrease in decolorization efficiency. More interestingly, the mechanism of decolorization was pointed out for the very first time that hydroxyl radicals probably exist as a radical-metal-ligand complex [84].

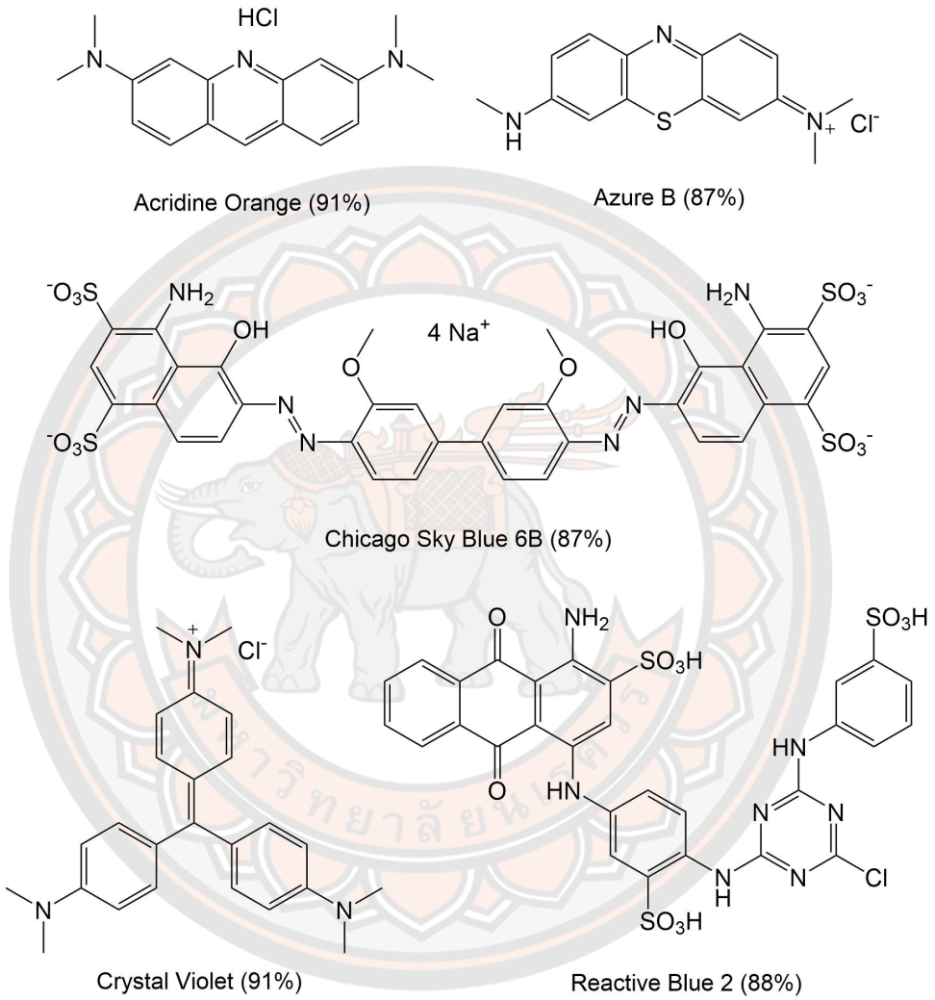

Figure 4 Chemical structures of Acridine Orange, Azure B, Chicago Sky Blue 6B, Crystal Violet, Reactive Blue 2, Reactive Blue 5, and Remazol Brilliant Blue R with decolorization degree

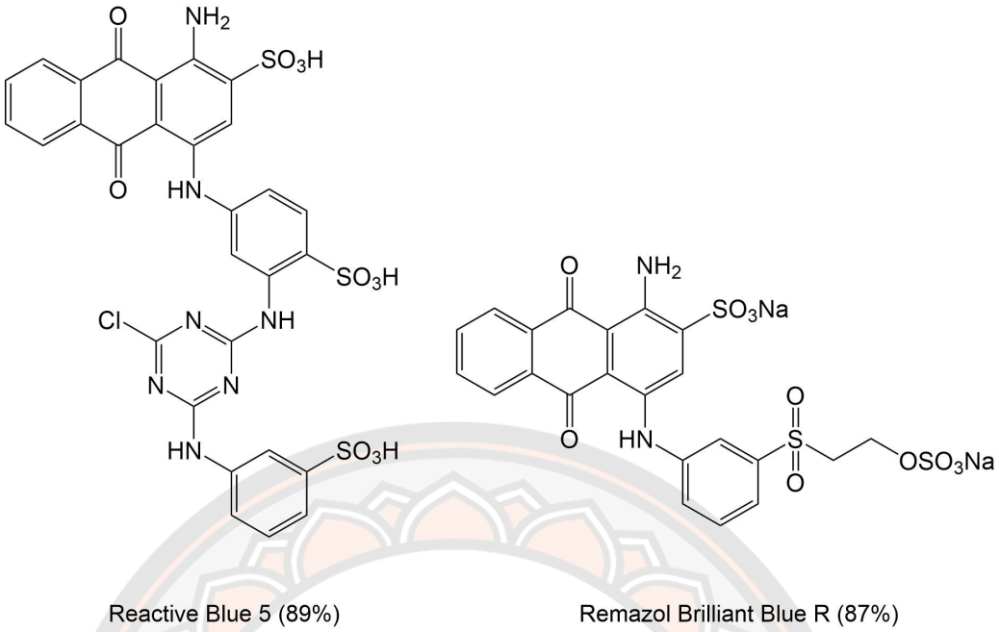

Figure 4 Cont.

The discussion of previous literature was only focused on the use of Cu/pyridine/ H_2O_2. A detailed investigation of H_2O_2/pyridine, H_2O_2/Cu(II), and H_2O_2/pyridine/Cu(II) processes were carried out, for decolorization of some selected dyes, by Bali et al. (2007) [85]. The effect of different components in the system such as initial Cu(II), pyridine, H_2O_2, dyestuff concentration, pH, mixing speed, and the reaction time was determined. The optimum catalytic system was found in the presence of 125 mM H_2O_2, 0.5% pyridine, and 0.1 mM Cu(II). The decolorization was very fast and achieved over 90% after 10 min (instead of a day) for some dyes with 50 ppm.

The study of the Cu/pyridine/H_2O_2 system was further compared to the original Fenton's reagent [51]. The experiments were conducted using synthetic textile wastewater including polyvinyl alcohol (PVA) and Remazol Turquoise Blue G-133, with 100 ppm and 50 ppm, respectively (**Figure 5**). Interestingly, the maximum efficiency achieved by the Cu system was about 92% and, the higher initial reaction rate. However, the hydrogen peroxide consumption was very high (4250 ppm), especially when compared to that used in Fenton's reagent (25 ppm).

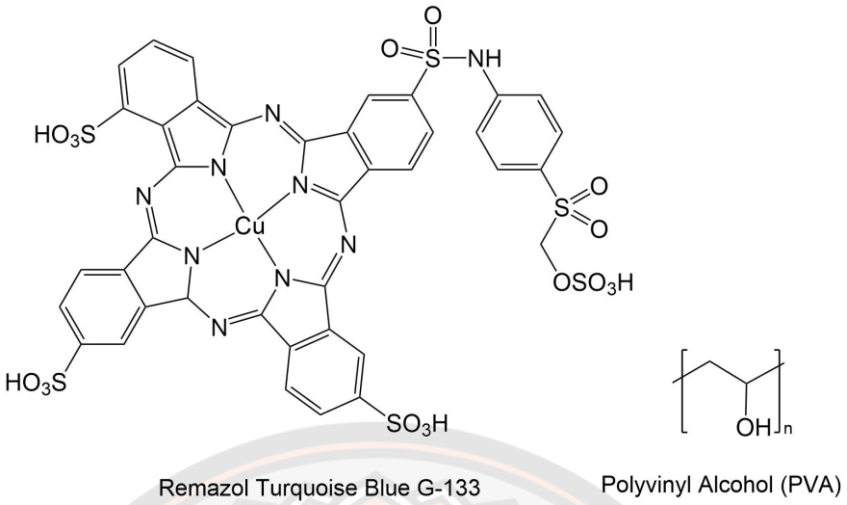

Figure 5 Synthetic textile wastewater (PVA+ Remazol Turquoise Blue G-133)

Some studies aim to replace pyridine with other organic ligands, such as ammonia, ethylenediamine, methylamine. Their reactivity mostly depends on the redox potential of the metal ions [86-88]. In addition, Cu(II)/succinic acid/H_2O_2 was investigated by Shah et al. (2003) [84]. A 24 h incubation of 10 mM Cu(II), 200 mM succinic acid, and 100 mM H_2O_2 resulted in decolorization of 200 ppm Poly B-411 (90%) and Reactive Blue (75%). The ESR spectra of Cu(II)-succinic acid-radical complex showed that the radical probably does not diffuse into the solution but bind with the ligand before the degradation of dyes.

The study of metal peroxo complexes (M-OOH) was further considered and discussed by Li et al. (2009) [89]. 4-Chlorophenol (CP) oxidation was proposed as shown in **Scheme 7**. Cu(II) ion in the complex was found to coordinate with four N or O atoms and two water molecules as axial ligands. The associating copper (II) complex was unstable. Once one water molecule dissociated from Cu(II) complex, hydrogen peroxide could directly associate with Cu(II) complex. Consequently, electron transfer from hydrogen peroxide to Cu(II) might happen. Thus, the possible reactive species LCu(I)-•OOH was formed.

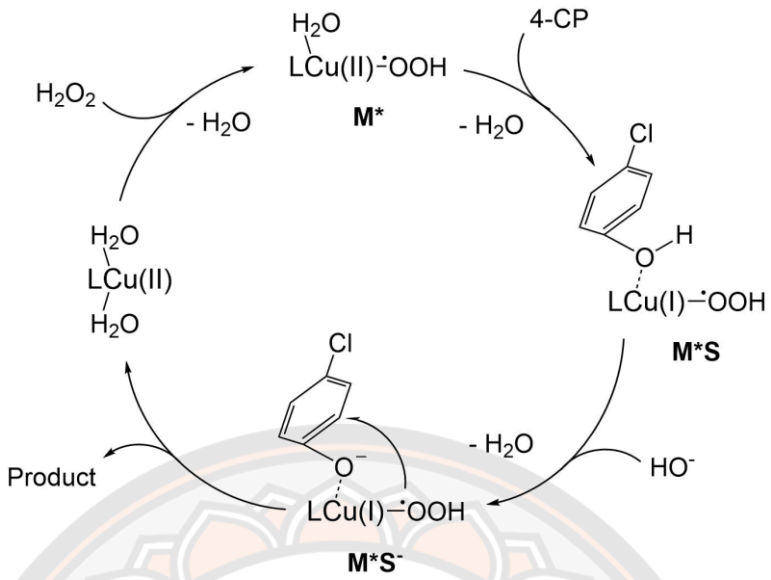

Scheme 7 Possible catalytic mechanism for the oxidation of 4-CP

Previous literature was described in several copper-based Fenton-like metal/ligand systems for homogeneous catalytic decomposition of hydrogen peroxide and generation of hydroxyl radicals. The main shortcoming of homogeneous catalytic processes ensues from the requirement for catalyst recovery or separation. It can be technically and economically unfeasible. Moreover, active homogeneous catalysts, including transition metal ions and their complex are toxic and thus present a potential environmental problem. Therefore, it is desirable to develop heterogeneous catalytic procedures where the catalysts are easily separable.

The heterogeneous catalyst was presented in a solid form of the complex itself or an immobilized complex on a solid support. The heterogeneous polymeric catalyst of Cu(II) for degradation of polycyclic aromatic hydrocarbons (PAH) in the presence of hydrogen peroxide was reported by Baldrian et al. (2005) [90]. Poly(glycidyl methacrylate) with 8-hydroxylquinoline and tris(2-aminoethyl)amine ligands immobilized on microporous methacrylate matrix were prepared with Cu(II), as shown in **Scheme 8**. The PAH was degraded by the incubation of 25 mg catalysts and 100 μmol H_2O_2 for a 7-day catalytic cycle at 25 ˚C.

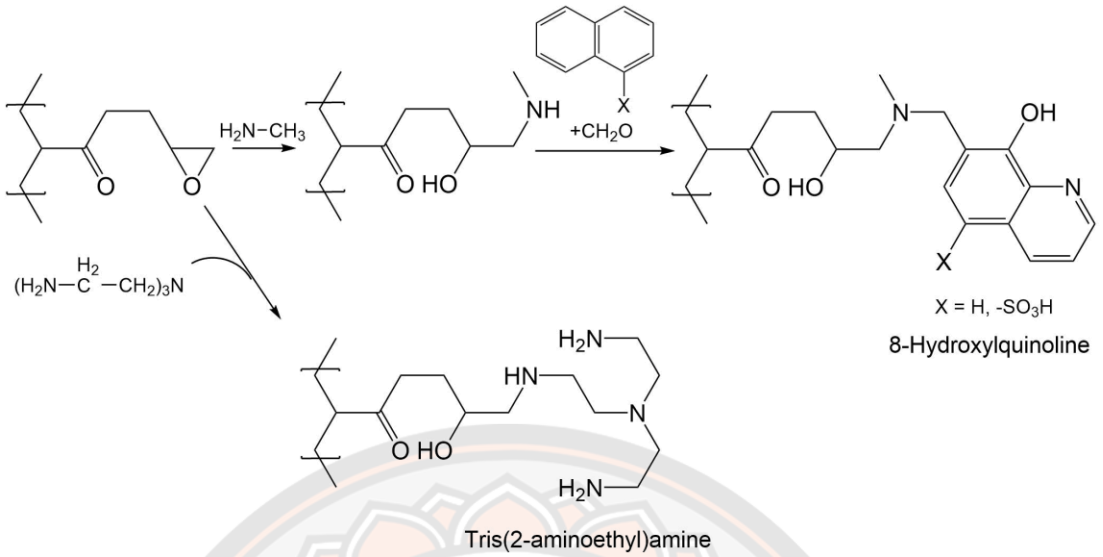

Scheme 8 Addition of ligand groups to the polymeric chain of poly(glycidyl methacrylate-*co*-ethylene dimethacrylate)

The catalyst based on ion-exchange binding including, metal- or metal complex-loaded ion exchangers and polymeric support may be limited. It was found that the carrier itself can be also oxidatively attacked by the produced ROS. This results in an irreversible loss of metal binding capacity. The convenient way to overcome this problem is the use of inorganic supports. It is necessary to find appropriate immobilization chemistry for binding metal chelates to the surface of a support. The inorganic support including silica (SiO_2) was functionalized by 4-aminopropyl trimethoxy silane (APTS) for binding catalytically active metal ions. The transition metal salicylaldimine complexes immobilized on silica support for hydroxylation of phenol were reported by Ray et al. (2007) [91]. The catalysts were prepared using APTS and salicylaldehyde to form a Schiff base anchored on the SiO_2, as shown in **Scheme 9**. It was observed that the catalysts performed well in the hydroxylation of phenol but only the effects of surface on that catalysis were discussed.

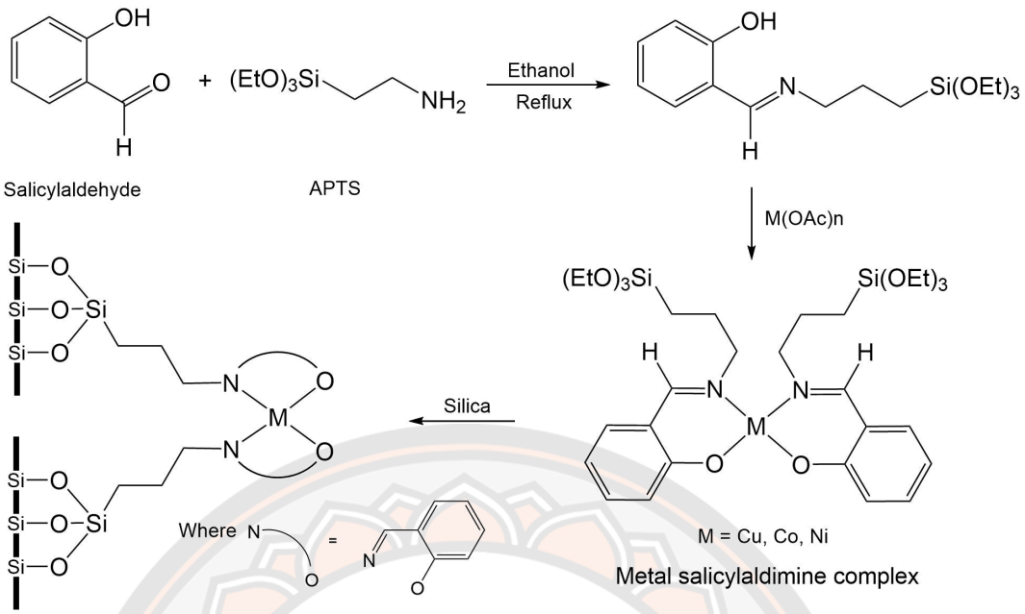

Scheme 9 Synthetic route of the supported salicylaldimine complex

In 2008, chelating sorbent of zirconium (ZrO_2) with diethylenetriamine-penta(methylene-phosphoric acid) (DTPMPA) was prepared for coordination of Cu(II) ion by Baldrian et al [92]. The catalyst was prepared by the sol-gel method of ZrO_2-DTPMPA, and then coordinated with $CuSO_4$ solution. The structure of DTPMA ligand chelated on ZrO_2 was only proposed as reported (**Scheme 10**). The catalyst was investigated in the oxidation of PAH through a Fenton-like reaction. Up to 90% of 15 ppm, PAHs (anthracene, benzo[a]pyrene, and benzo[b] fluoranthene) were decomposed by 10 mg mL^{-1} of the catalyst with 100 mmol of H_2O_2 during a five-day catalytic cycle at 30 ˚C (**Figure 6**). There is a suggestion that the use of inorganic support for Cu(II) ion catalytically active in Fenton-like reactions can perform potentially overcome the problem with oxidative damage of the support. It was confirmed by the simple recovery from treated solution and stability of the catalyst prepared in this work.

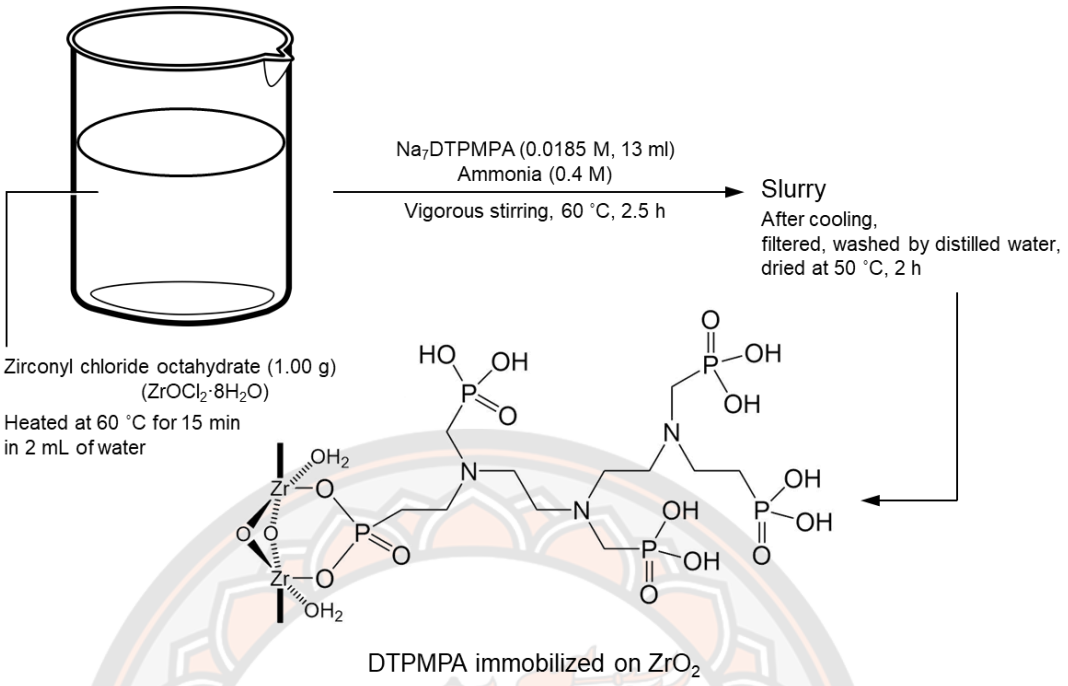

Scheme 10 Preparation of diethylenetriamine-penta(methylene-phosphoric acid) chelated on the ZrO_2 surface

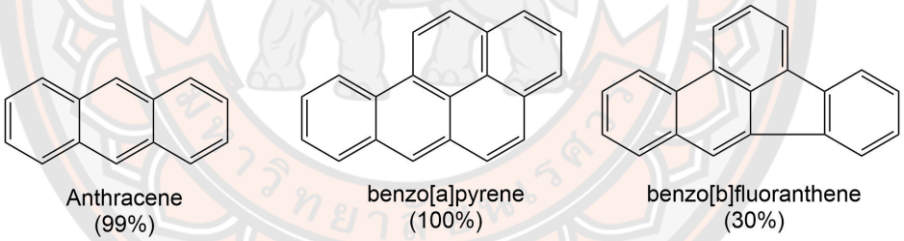

Figure 6 Polycyclic aromatic hydrocarbons (anthracene, benzo[*a*]pyrene and benzo[b] fluoranthene) with degradation degree

In 2014, Fei et al. reported simple Cu(II) Schiff base complexes as efficient heterogeneous Photo-Fenton-like catalysts for degradation of Methyl Orange (MO) [93]. The chemical structure of MO is displayed in **Figure 7**.

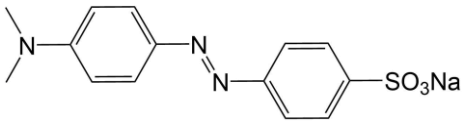

Figure 7 Chemical structure of Methyl Orange

The H_2L1 (H_2L1 = *N*-salicylidene-2-aminoethanol) with Cu(II) ion was prepared in two forms of $[Cu(L1)Cl]_2$ and $[Cu(HL1)_2]$ as a dinuclear and a mononuclear, respectively (**Scheme 11**). The complexes were characterized by IR, elemental analysis, and X-ray single-crystal diffraction methods. In the MO degradation, the complexes were performed as a heterogeneous catalyst under the experiment condition: the complexes 0.0020 g; H_2O_2, 12 mM; pH 6.55-6.70; UV light 300 W. 20 μM of MO was completely degraded within 2.0 min (**Figure 8**).

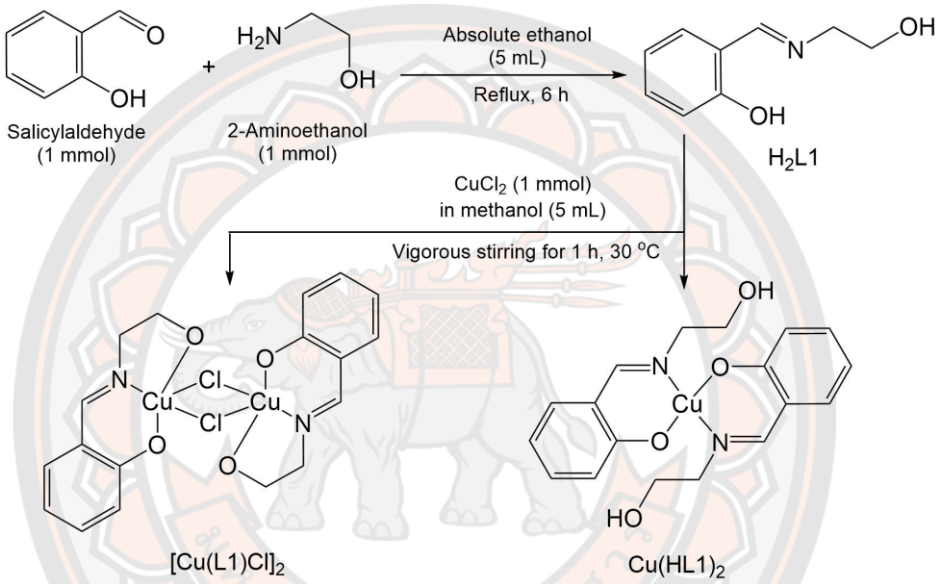

Scheme 11 Synthetic route of *N*-salicylidene-2-aminoethanol complexes with Cu(II) ion

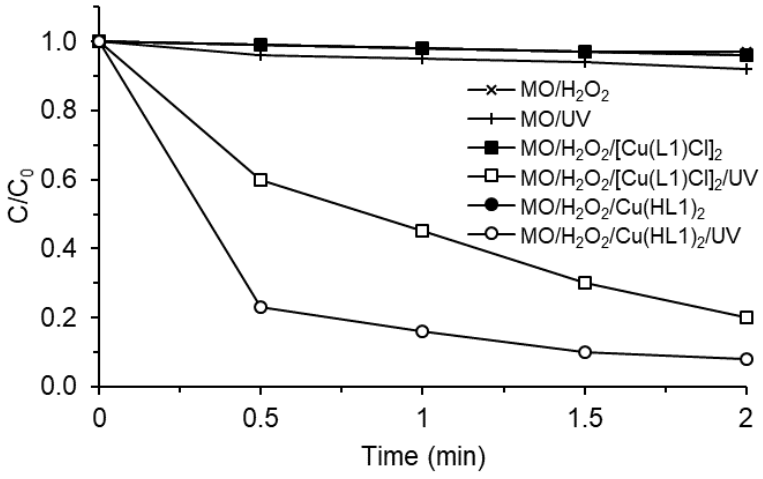

Figure 8 Decolorization efficiency of $[Cu(L1)Cl]_2$ and $Cu(HL1)_2$ in control experiments: MO, 20 μM; $[Cu(L1)Cl]_2$ and $Cu(HL1)_2$ 0.0020 g; H_2O_2, 12 mM; pH 6.55-6.70; UV light 300 W

The new homogeneous Cu(II) complexes which contain H_2L2 (H_2L2 = *N*-[(2-oxy-acetatebenzyl)]-2-aminothanol were reported by Fei et al. (2014) [94]. The complexes were prepared in two forms of [Cu(L2)Cl] and [Cu(L2)Br] as distorted squared pyramidal (**Scheme 12**).

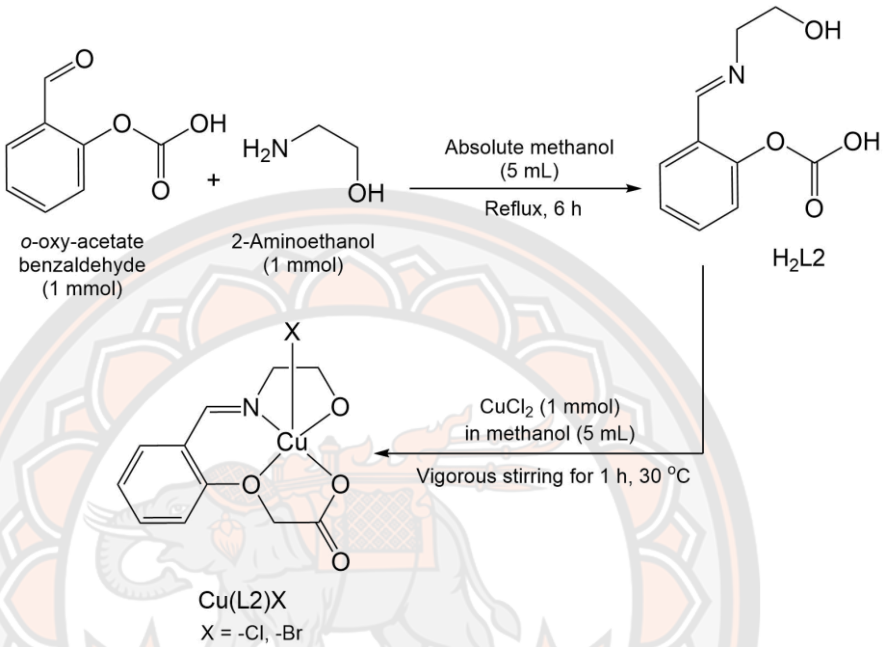

Scheme 12 Synthetic route of *N*-[(2-oxy-acetatebenzyl)]-2-aminothanol) complexes with Cu(II) ion

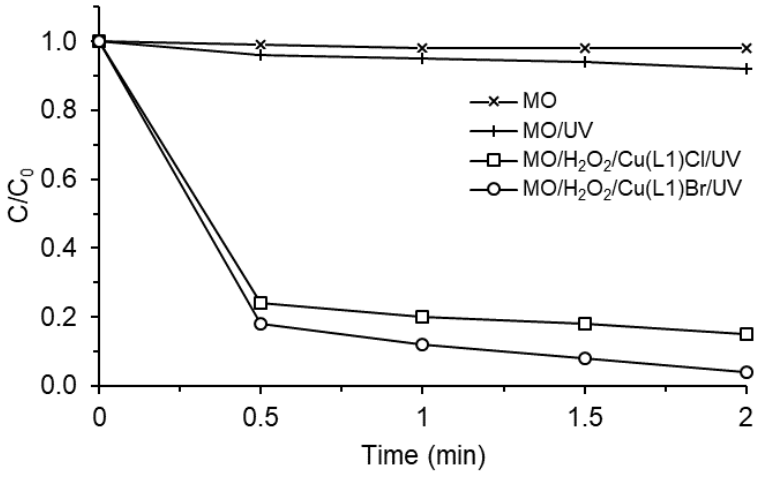

Figure 9 Decolorization efficiency of Cu(L2)Cl and Cu(L2)Br in control experiments: MO, 20 µM; Cu(L2)Cl and Cu(L2)Br 3.11×10^{-6} M; H_2O_2, 24 mM; pH 6.55-6.70; UV light 300 W

The complexes were characterized by IR, elemental analysis, and X-ray single-crystal diffraction methods. In the MO degradation, the complexes were performed as a homogeneous photo-Fenton-like catalyst under the experiment condition: the complexes 3.11×10^{-6} M; H_2O_2, 24 mM; pH 6.55-6.70; UV light 300 W. 20 μM of MO was completely degraded within 2.0 min (**Figure 9**).

In 2016, Hailu et al. reported a Cu(II) Schiff base complex encapsulated in a zeolite (Y) for the degradation of 4-chloro-3-methylphenol (PCMC) [95]. The ligand (*N*,*N*'-disalicylidene-1,2-phenylediamine, H_2L3) was synthesized by the condensation reaction of salicylaldehyde and *o*-phenylenediamine. The HL3 was encapsulated in zeolite super cage using Cu-exchanged zeolite (CuY, 1 g) under reflux at 150-200 ˚C for 12 h (**Figure 10**).

Figure 10 Zeolite-encapsulated *N*,*N*'-disalicylidene-1,2-phenylediamine complex with Cu(II) ion

The chemical structure of PCMC as a selected pollutant is displayed in **Figure 11**. The almost complete removal of PCMC was achieved with the catalyst after 120 min under the optimum reaction condition: the catalyst 0.1 g; H_2O_2, 75 mmol L^{-1}; PMC 0.35 mmol L^{-1}; 50 ˚C (**Figure 12**).

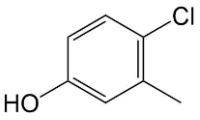

Figure 11 Chemical structure of 4-chloro-3-methylphenol

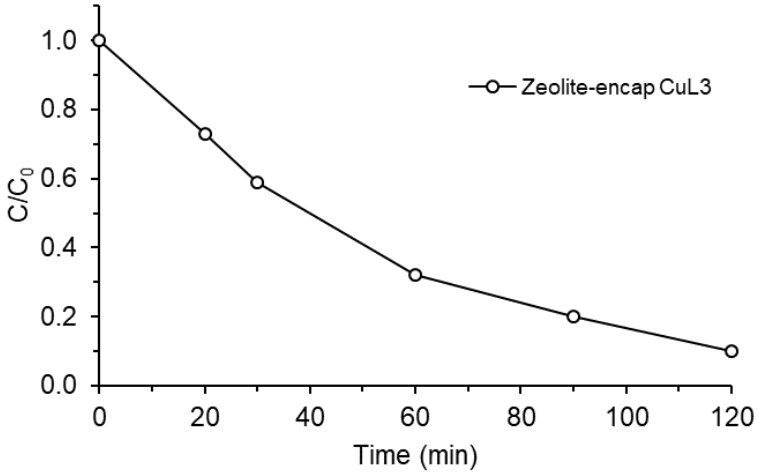

Figure 12 Catalytic efficiency of zeolite-encapsulated CuL_3 in control experiments: the catalyst 0.1 g; H_2O_2, 75 mmol L^{-1}; PCMC 0.35 mmol L^{-1}; 50 ˚C

The catalytic efficiency was represented by a pseudo-first-order kinetic plot (**Figure 13**). The rate constant (*k*) for PCMC oxidation with the zeolite-encapsulated CuL3 catalyst was 0.0191 min^{-1} as displayed in the slope (m) of the linear function.

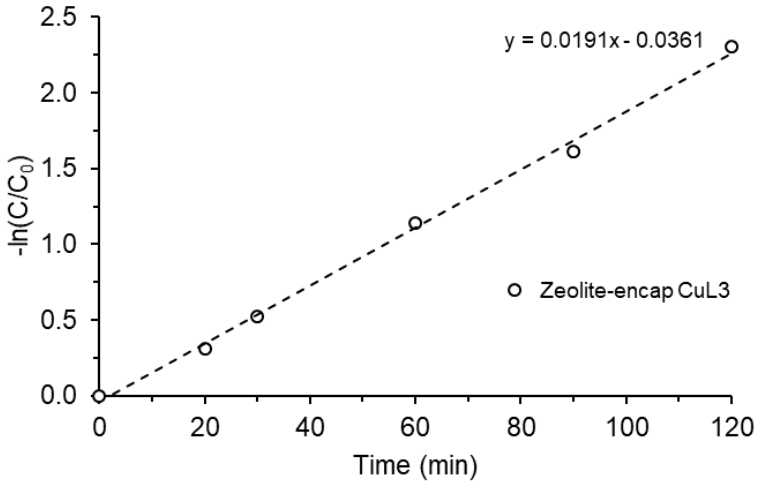

Figure 13 Pseudo-first-order kinetic plot for catalytic efficiency of zeolite-encapsulated CuL_3 in control experiments: the catalyst 0.1 g; H_2O_2, 75 mmol L^{-1}; PCMC 0.35 mmol L^{-1}; 50 ˚C

In 2017, Yuan et al. reported a Cu(II) Schiff base complex with 2-amino pyridine (2-APY) immobilized on silica microspheres as a Fenton-like catalyst for Rhodamine B (RhB) [81]. The catalyst was prepared by immobilization of Cu(II)-pyridine complex on silica support as displayed in **Scheme 13**.

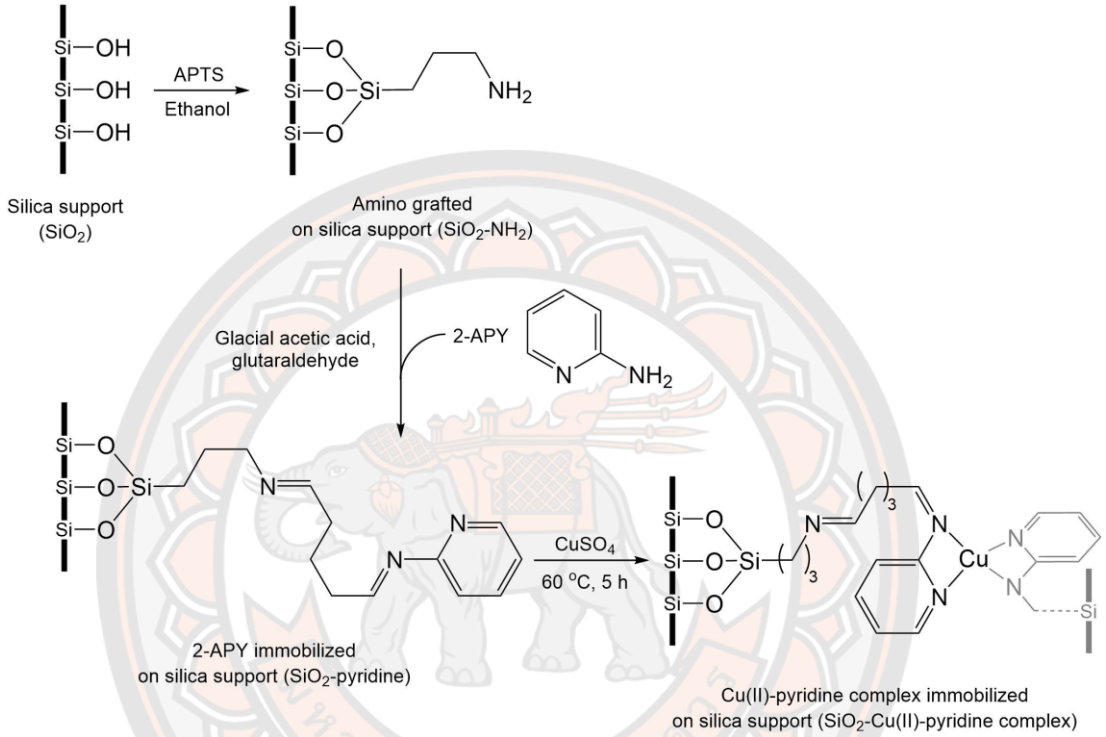

Scheme 13 Synthetic route of 2-amino pyridine complex with Cu(II) ion immobilized on silica support

RhB was selected as a dye model for the degradation study. The chemical structure of RhB is shown in **Figure 14**. 5-7.5 mg L^{-1} of RhB was degraded by the catalyst in 6 h under the optimum reaction condition: SiO_2-Cu(II) pyridine complex, 0.0020 g; H_2O_2, 12 mM; pH 7. The catalyst was discussed as a hydroxyl radical generator through a Fenton-like reaction. It was confirmed by the different conditions as shown in **Figure 15**. The rate constant of each condition was represented as a pseudo-first-order kinetic plot in **Figure 16**. The number for Fenton-like reaction (RhB + H_2O_2 + cat.), i.e., 0.459 h^{-1}, is higher than the control conditions (RhB + cat. and RhB + H_2O_2).

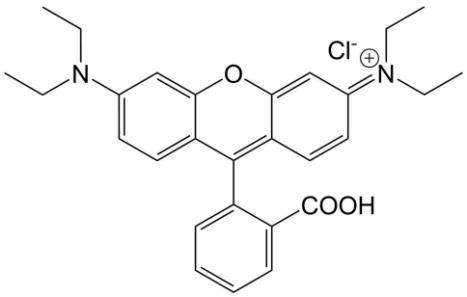

Figure 14 Chemical structure of Rhodamine B

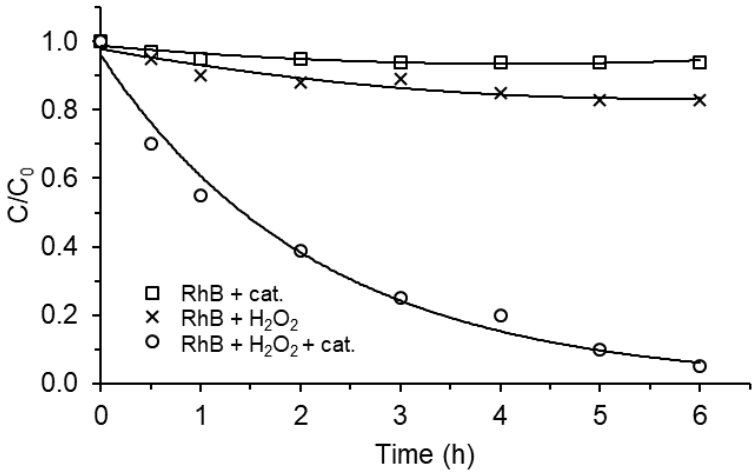

Figure 15 Catalytic efficiency of SiO_2-Cu(II)-pyridine complex under the optimal condition: the catalyst 2 g L^{-1}; H_2O_2, 200 mg L^{-1}; RhB 5 mg L^{-1}; pH 7.1

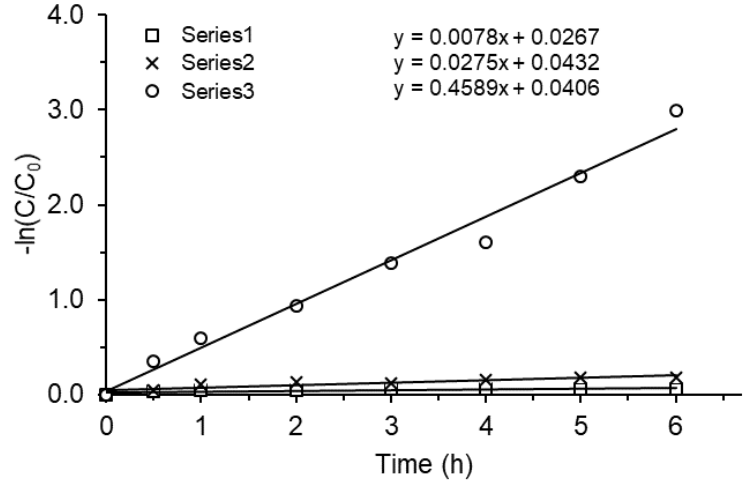

Figure 16 Pseudo-first-order kinetic plot for catalytic efficiency of SiO_2-Cu(II)-pyridine complex under the optimal condition: the catalyst 2 g L^{-1}; H_2O_2, 200 mg L^{-1}; RhB 5 mg L^{-1}; pH 7.1

CHAPTER III

MATERIALS AND METHODS

1. Materials

All chemicals were used without further purification. Ammonium hydroxide (NH_4OH, 28 wt.%), tetraethyl orthosilicate (TEOS, 98%), (3-Aminopropyl) triethoxysilane (APTES, 99%), 8-aminoquinoline ($C_9H_8N_2$, 98%), commercial ethanol (C_2H_5OH), isopropanol (IPA, C_3H_8O), glutaraldehyde 25 wt.% ($C_5H_8O_2$), glacial acetic acid (CH_3COOH), and coumarin ($C_9H_6O_2$, 99%) were purchased from Sigma-Aldrich. Hydrogen peroxide 30wt.% (H_2O_2) and p-benzoquinone (BQ, $C_6H_4O_2$) were purchased from MERCK. Copper (II) sulfate heptahydrate ($CuSO_4 \cdot 7H_2O$, 98%) was purchased from Ajax Finechem. Deionized water (DI) was used throughout the experiment.

2. Experiments

2.1 Preparation of silica support

The silica support (denoted: SiO_2) was synthesized by hydrolysis of TEOS in distilled ethanol solution [96]. Firstly, the mixture of ethanol (170 mL) and DI water (511 mL) was sonicated for 10 min. Then, TEOS (7.0 mL) was added dropwise while sonicating, and after 20 min, 28 wt.% NH_4OH (12 mL) was added as a catalyst to promote the condensation reaction. The reaction was carried out for a further 60 min by stirring at 750 rpm to get a white turbid suspension. The white solid of silica support (1.8 g) was obtained after drying at 100 ˚C for 5 h (**Scheme 14**).

2.2 Preparation of amine-functionalized silica support

The prepared silica support was dried at 100 ˚C for 30 min before use. The dried solid (1.2 g) was dispersed into ethanol solution (10 mL) and kept stirring at 500 rpm. Then, APTS (3.6 mmol, 0.84 mL) was slowly added into the suspension.

After 30 min, DI water (7.2 mmol, 130 μL) was added to perform hydrolysis of the alkoxide groups of APTS. The amount of water added was twice the amount required to completely hydrolyze APTS loading [97]. The reaction was continued for a further 30 min and the solids (1.1 g) were obtained after drying at 100 ˚C for 2 h (**Scheme 15**). The prepared amine-functionalized silica was denoted: SiO_2-NH_2.

2.3 Preparation of Cu(II)-quinoline complex immobilized on silica support

1.0 g of amine-functionalized silica support was dispersed in DI water and sonicated for 10 min. Then, 8-aminoquinoline (432 mg, 3 mmol) dissolved in 5 mL of CH_3CN was added slowly into the suspension. After 30 min, the mixture of glutaraldehyde (2.4 mL, 6 mmol) and glacial acetic acid (0.69 mL, 12 mmol) was added dropwise. The reaction was carried out at room temperature for 12 h. Afterward, 20 mL of 0.1 M copper(II) sulfate solution was added into the reaction and kept stirring at 60 ˚C for 5 h [81]. The product (0.8 g) was collected by centrifuge at 9000 rpm, washed with DI water, and dried at 80 ˚C for 4 h (**Scheme 16**). The product was denoted: SiO_2-Cu(II)-quinoline complex or catalyst.

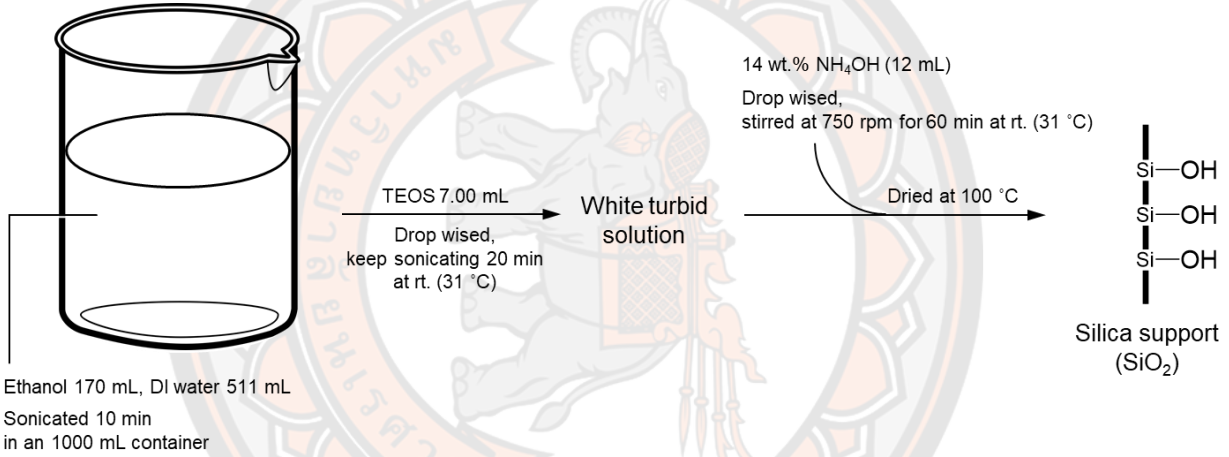

Scheme 14 Synthesis of silica support

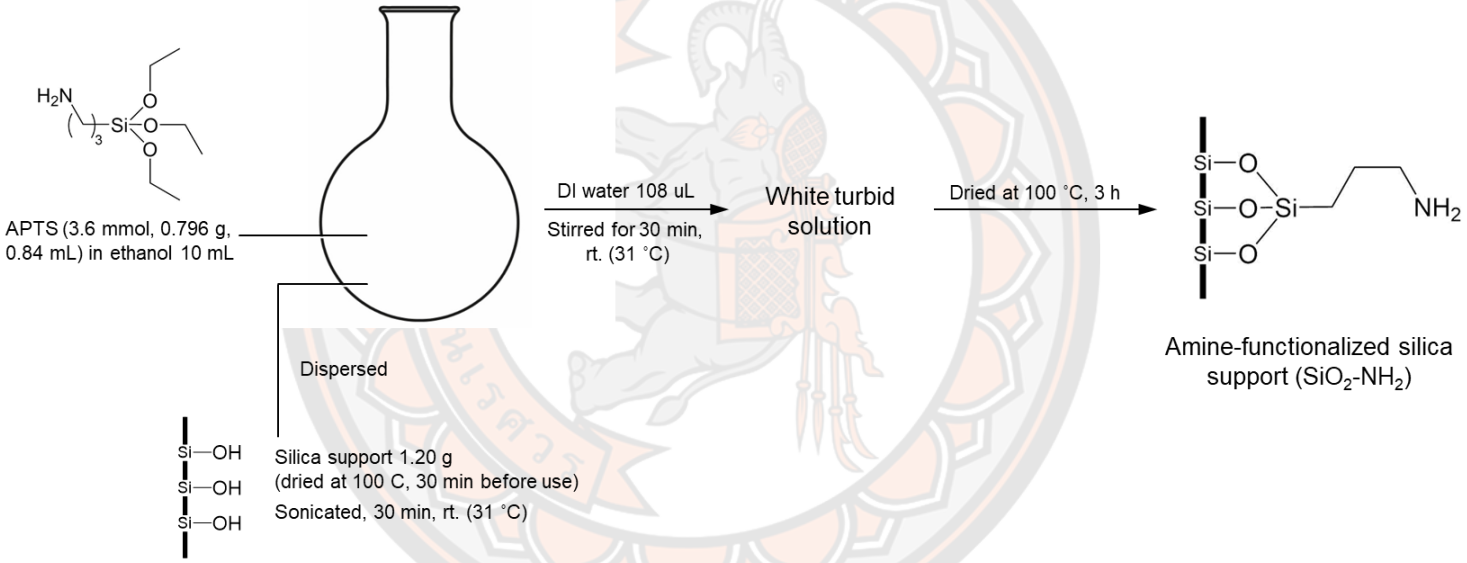

Scheme 15 Synthesis of amine-functionalized silica support

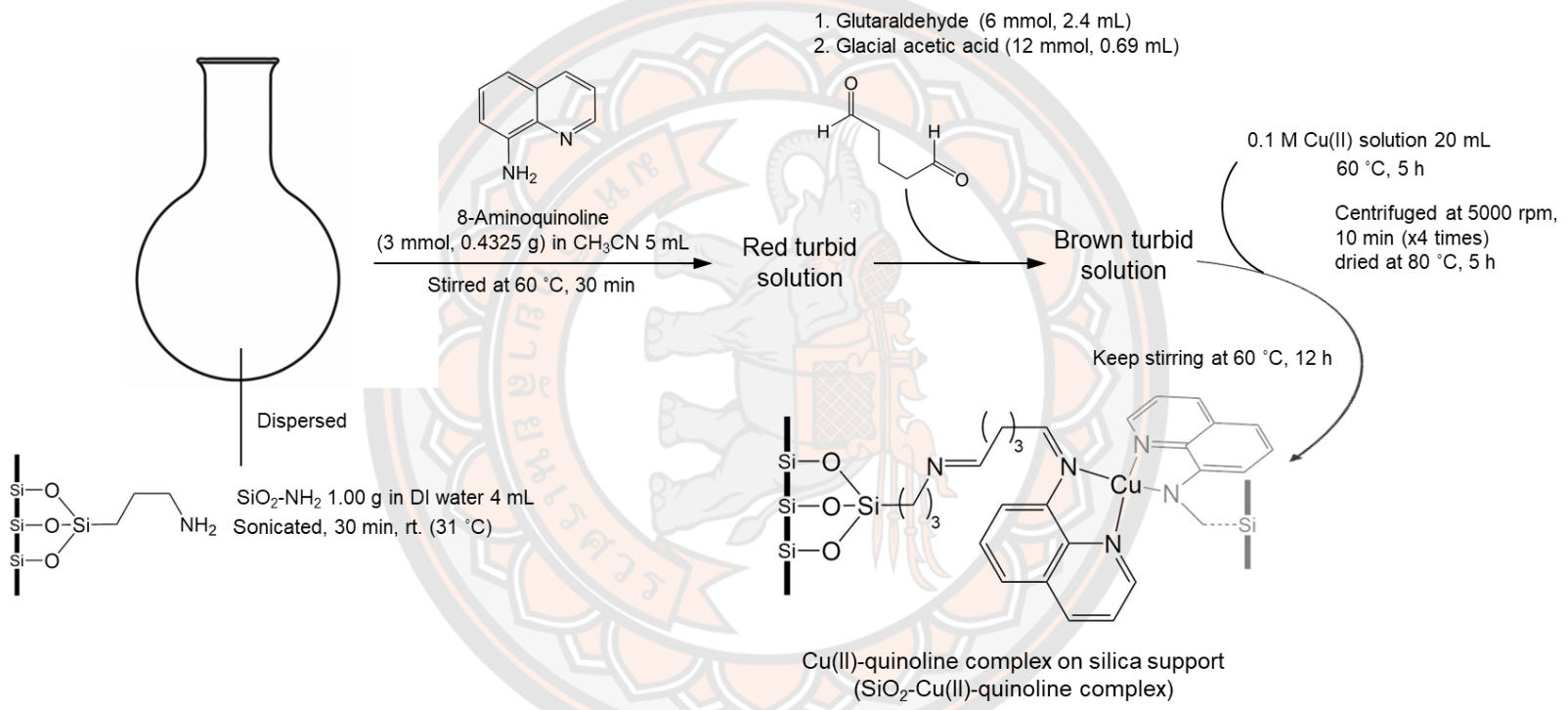

Scheme 16 Synthesis of Cu(II)-quinoline complex immobilized on silica support

2.4 Characterizations

The change on the surface of silica was monitored by Fourier Transform Infrared Spectrometer (FT-IR, Spectrum GX). The crystallinity of prepared solids was obtained by X-ray diffraction spectroscopy (XRD, Panalytical /Expert 2Theta: 5-140 degree) The morphologies, element distributions, and sizes of samples were observed by field emission scanning electron microscopy (FESEM, LEO1455VP) equipped with the energy dispersive X-ray (EDX). The specific surface areas of samples were evaluated using the Brunauer-Emmett-Teller method (BET, TriStar II 3020). The elemental composition and surface chemical state were determined with an X-ray photoelectron spectroscopy (XPS, Mg K_{α} as radiation source, the AXIS Ultra DLD, AXIS Ultra DLD). The UV-vis diffuse reflectance spectrum (DRS) was obtained with a UV-vis spectrophotometer (UV-Vis Spectrophotometer Agilent 8453, $BaSO_4$ as a reference). The UV-vis absorption spectrum for solutions was investigated using a UV-Vis spectrophotometer (UV-6100 UV/VIS spectrophotometer).

2.5 Adsorption experiment

The adsorption of MB by the prepared silica and the catalyst was studied by a batch operation, only focusing on the effects of contact time. Batch sorption experiments were performed in a closed chamber at the ambient temperature inside, which was maintained at 28˚C. 1.0 mg of catalyst (0.25 mg/L) was dispersed in a 5.0 mL aqueous solution containing 5 ppm of MB for 2 min with ultrasonication. Then, the suspension was magnetically stirred and analyzed at every certain time (30, 60, 120, and 150 min). The suspensions were centrifuged at 5000 rpm for 7 min to collect the final solution. The concentrations of each solution correspond to the absorption value of MB solution determined by recording at the maximum absorption (664 nm) using a UV-vis spectrometer.

2.6 Photocatalytic experiment

The photocatalytic activities of the prepared catalyst in the degradation of MB were performed in a closed chamber with vertical light irradiation. The ambient temperature inside of the chamber was maintained at 28˚C with air cooling. 30W UV lamp was used as the light source and the distance between the level of the solution and light source was 13 cm. The reaction was carried out by a batch experiment to avoid the loss of catalyst dosage in each reaction. In a typical process: 1.0 mg of catalyst (0.25 mg/L) was dispersed in 5.0 mL aqueous solution containing a 5 ppm of MB for 2 min with ultrasonication. Then, the suspension was magnetically stirred in the dark for 30 min to reach an adsorption equilibrium. Prior to the irradiation, one of the reactions was taken out and centrifuged to obtain the clear supernatant. The MB concentration was remarked as C_{30}. Then, 3000 ppm of 30 wt.% H_2O_2 was introduced in a system and the UV lamp was turned on. The reaction suspension at every certain time (30, 60, and 120 min) was centrifuged and analyzed. The concentrations which correspond to the absorption value of MB solution were determined by recording at the maximum absorption (664 nm) using a UV-vis spectrometer. The decolorization efficiency of MB was obtained by the following formula:

$$\eta = (1 - C_t/C_0) \times 100\% = (1 - A_t/A_0) \times 100\%$$

where C_t is the concentration of MB solution at the reaction time t, C_0 is the concentration of initial MB solution at 0 min; A and A_0 are the corresponding absorption values.

2.7 Effect of hydrogen peroxide concentration

The method and conditions of this study were similar to the above photocatalytic experiment except for the uses of various hydrogen peroxide adding into the MB solutions. The concentrations were ranged from 0 ppm, 750 ppm, 1500 ppm, and 3000 ppm. The reaction suspension at every certain time was centrifuged and analyzed. The concentrations which correspond to the absorption value of MB solution were determined by recording at the maximum absorption (664 nm).

2.8 Active species trapping experiments

In order to prove the generated active species in the photocatalytic reaction, coumarin, isopropanol (IPA), and p-benzoquinone (BQ) were used as the scavengers of hydroxyl radicals ($^{\bullet}OH$), and superoxide radicals ($^{\bullet}O_2^-$), respectively. The solution of the scavengers was added into the MB solution to study the influence of different active species. The photocatalytic reaction was performed similarly to the mentioned photocatalytic experiment except for the addition of scavengers into the MB solution. A control experiment was run without adding those scavengers.

Coumarin

Coumarin (14.6 mg, 0.1 mmol) was dissolved in 100 mL of distilled water [98]. The method and conditions of this study were similar to the above photocatalytic experiment except for the use of prepared coumarin solution instead of MB. After adsorption-desorption equilibrium at 30 min in the dark, 3000 ppm of 30 wt.% H_2O_2 was introduced in a system and the UV lamp was turned on. The fluorescence emission spectrum was excited at 320 nm. The reaction was monitored by the increased fluorescence intensity of 7-hydroxycoumarin at 450 nm [99]. The reaction suspension every certain time (30, 60, and 120 min) was centrifuged and analyzed as mentioned in the photocatalytic experiment.

Isopropyl alcohol (IPA)

IPA (0.1 mol L^{-1} or 0.3 mol L^{-1}) was added into the batches of MB solution (5 ppm). Then, UV light was turned on in a closed chamber. The reaction was monitored by the decreased absorbance of MB at 664 nm. The reaction suspension every certain time was centrifuged and analyzed as mentioned in the photocatalytic experiment.

p-Benzoquinone (BQ)

BQ was recrystallized from ethanol before being used [100]. Then, 216.1 mg (2 mmol) was dissolved in distilled ethanol. The prepared solution (0.2 mol L^{-1}, 25 µL) was added into the batches of MB solution (5 ppm). Then, UV light was turned on in a closed chamber. The reaction was monitored by the decreased absorbance of MB at 664 nm. The reaction suspension every certain time was centrifuged and analyzed as mentioned in the photocatalytic experiment.

2.9 Photocatalytic stability

The photocatalytic stability of the prepared catalyst was determined by two consecutive cycles under the typical condition of 5 ppm of MB (pH 7, 100 mL), 0.20 g L^{-1} of catalyst, and 3000 ppm of 30 wt.% H_2O_2. The catalyst was used repeatedly after centrifugation (5000 ppm, 7 min) and dry at 80 ˚C for 2 h.

CHAPTER IV

RESULTS AND DISCUSSION

1. Synthesis

1.1 Silica support (SiO_2)

Scheme 17 shows the formation of silica. The solid was synthesized by hydrolysis of TEOS and condensation polymerization of alkoxysilanes. Ammonia was used as a basic catalyst in these processes, and also used to protect the aggregation of newly formed silica particles [101]. Firstly, TEOS was hydrolyzed to generate a silanol group (-Si-OH) and an ethanol molecule. After the reaction between silanol groups, a covalent bond of silicon oxide was formed, followed by an elimination of a water molecule. The condensation reaction was performed continuously, and the particles of silica appeared because of their poor solubility in the water-ethanol solution.

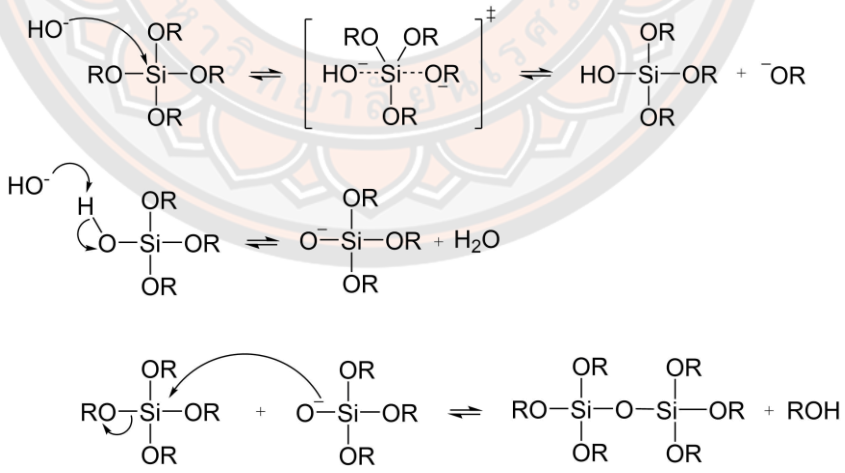

Scheme 17 Base-catalyzed condensation of TEOS

The structure consists of dense SiO_2. The building blocks of these particles are randomly distributed tetrahedrons and their surface is coated with silanol groups.

The yield of SiO_2 was calculated based on the theoretical yield as described by Koźlecki et al. It is assumed that all C_2H_5O- groups were replaced by -OH groups [102]. The yield was moderate, with 62%.

1.2 Amine-functionalized silica support (SiO_2-NH_2)

The surface of silica was coated by amino groups (-NH_2) of APTS. Firstly, APTS was hydrolyzed following by a condensation reaction with hydroxyl groups of the surface of silica as seen in **Scheme 18**. Water was incorporated to perform hydrolysis of the alkoxide groups of APTS. The amount of water added was twice the amount required for complete the hydrolysis of APTS loading [97].

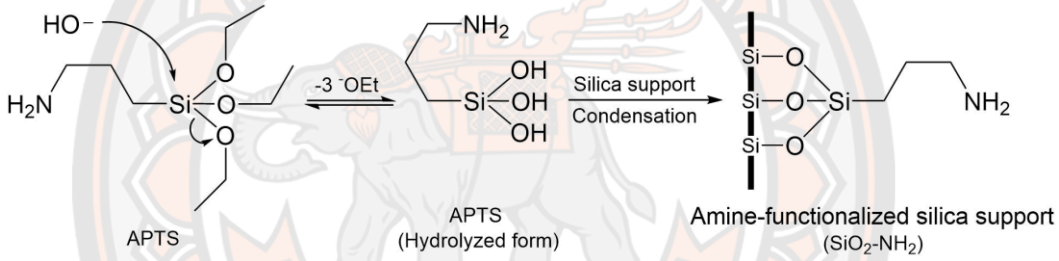

Scheme 18 Formation of functionalized amine on silica support

1.3 Cu(II)-quinoline complex immobilized on silica support

In order to prepare particle dispersions, the solid of SiO_2-NH_2 was sonicated in DI water. 8-aminoquinoline was added to the suspension, which was stirred for 30 min to perform the adsorption on the surface of SiO_2-NH_2. The Schiff base was obtained after addition of the crosslinking agent, glutaraldehyde, catalyzed by an acid catalyst (as shown in **Scheme 19**). Firstly, the lone paired electron of the N atom of SiO_2-NH_2 and 8-aminoquinoline attacks the carbonyl carbon. Then, the water molecule is eliminated to form a Schiff base [103].

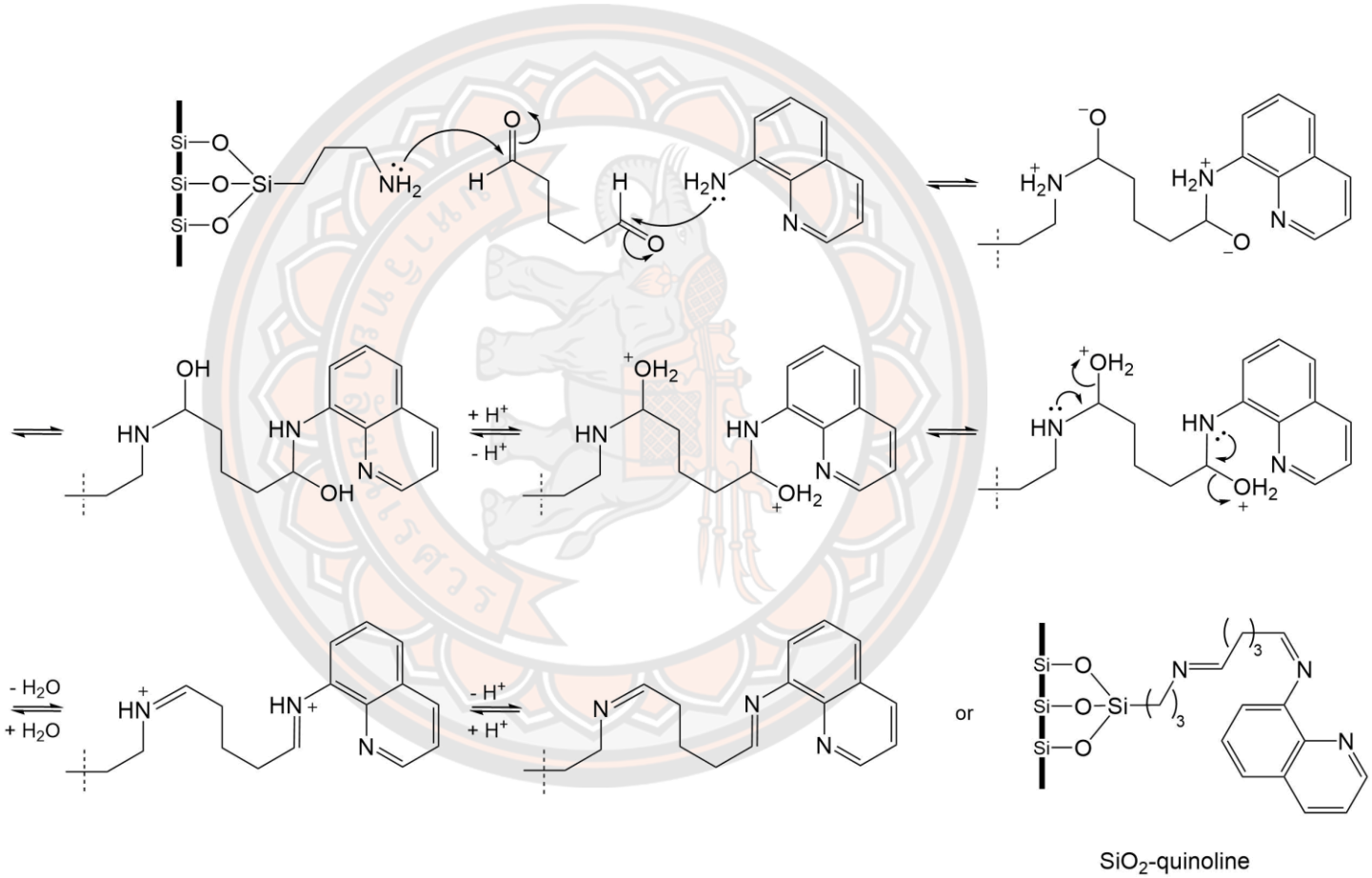

Scheme 19 Formation of Schiff bases on the silica support

After the addition of the $CuSO_4$ solution to 8-aminoquinoline modified silica support, the blue color of the solution was turned to pale blue. It probably indicated that N atoms in the quinoline ring and in Schiff base coordinated to copper (II) ions as shown in **Scheme 20** [81].

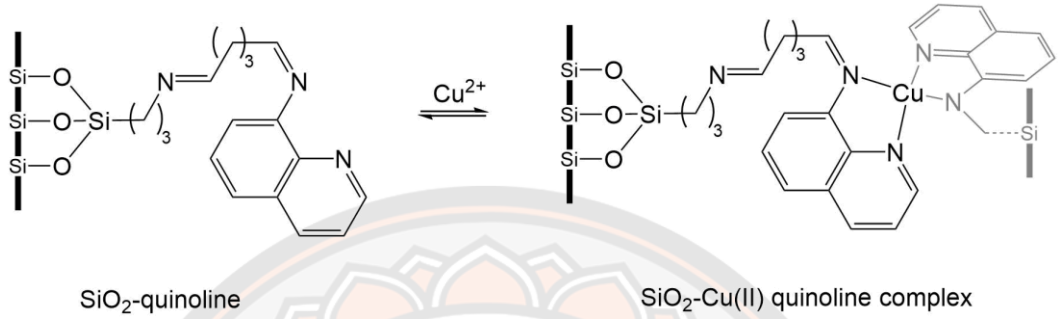

Scheme 20 Formation of copper(II) quinoline complex immobilized on silica support

2. Catalyst characterizations

2.1 Fourier transform infrared spectroscopy (FTIR)

The interface of the silica surface plays an important role in the adsorption process. Its characteristics determine the nature of bonding between adsorbate and adsorbent. FTIR, one of the surface study techniques, was used to investigate the behavior of porous silica. Basically, there are 3 modes of silanols on silica surface; (i) isolated free (single silanols), (ii) geminal free, and (iii) vicinal (OH groups bound together through hydrogen bond) [104].

All of them were found in the region of 3200-3800 cm^{-1} corresponding to ν_{OH} stretching mode. A broad band at 3715 cm^{-1} suggested the presence of isolated silanol because of the absence of a hydrogen bond [105]. The appearance of 3530 cm^{-1} is identified as germinal silanol due to its hydrogen bonding. Even though those silanols appeared at different numbers, it is still difficult to differentiate between those two modes because their properties are almost similar [106]. Also, the absorption range between 3400 to 3600 cm^{-1} depends on the formation of a hydrogen-bonded water network. Therefore, in the presence of water adsorption on the silica surface, it is difficult to directly observe the silanol groups [107].

The IR spectral characteristic of silica was previously reported by Jal et al. [108] as shown in **Table 2**.

Table 2 IR spectral characteristic of silica

Frequency (cm^{-1})	Position assignment	Value reported	Reference
462	Si–O bond rocking	465-475	[109]
800	OH bending (silanol)	800-870	[110-114]
970-980	Si–OH bond stretching	935-980	[109-112]
1102	Asymmetric Si–O–Si stretching in SiO_4 tetrahedron	1050-1150	[115-119]
1630	O–H bending (molecular water)	1625	[120]
3000-4000	O–H stretching and adsorbed water	3000-3800	[120]
3755	OH stretching	3740-3750	[111]

Figures 17-19 display the FTIR results of all synthesized products. Only characteristic bands of silica were found. The wavenumbers correspond to the reported value. Additionally, there is no additional peak observed when SiO_2 was modified by the amine functionalization and the immobilization of Cu(II)-quinoline complex on the surface. The amount of APTES was only 3.6 mmol which is lower than the literature (21 mmol) [81] as well as the assumed amount of Cu(II)-quinoline complex. As a result, it might be difficult to detect those additions on the surface of silica by FTIR.

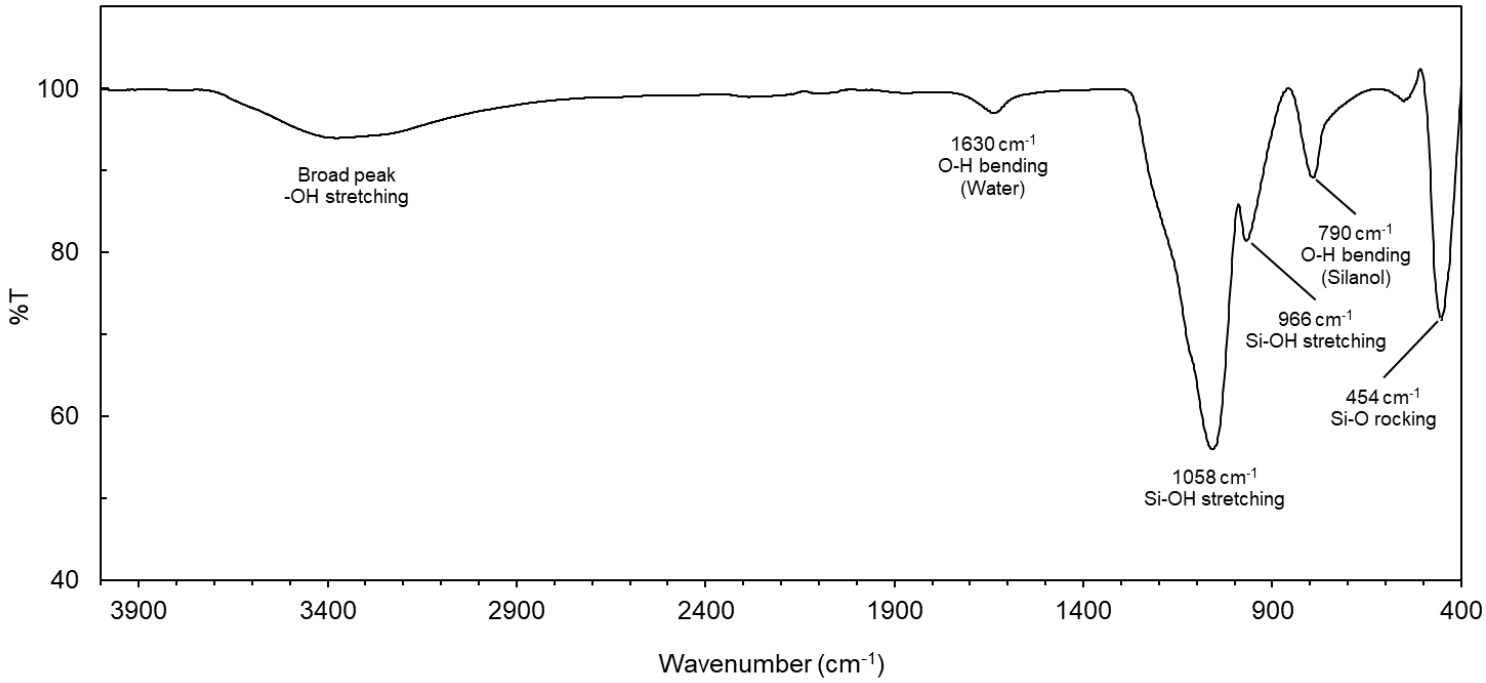

Figure 17 FTIR spectrum of SiO_2

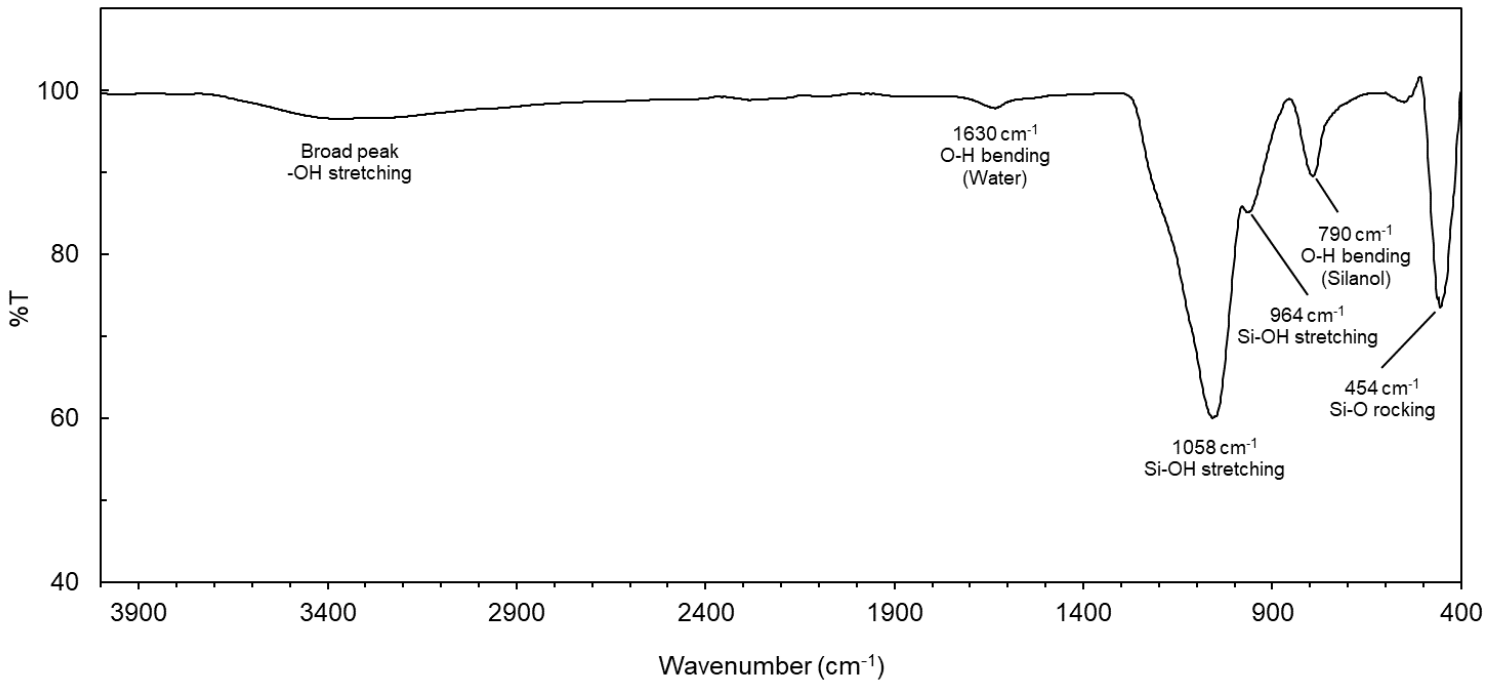

Figure 18 FTIR spectrum of SiO_2-NH_2

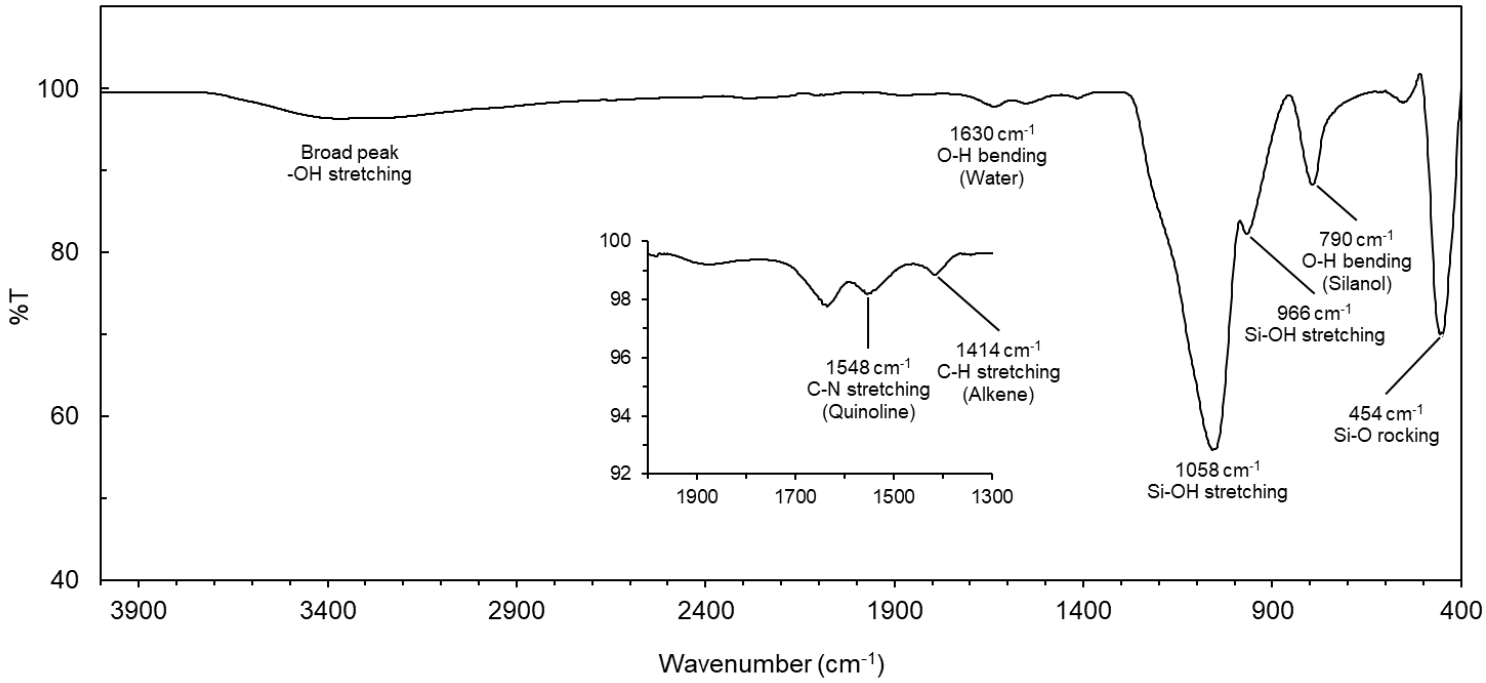

Figure 19 FTIR spectrum of SiO_2-Cu(II)-quinoline complex

2.2 X-ray diffraction (XRD)

The XRD patterns of the synthesized SiO_2, SiO_2-NH_2, and SiO_2-Cu(II) complex are shown in **Figure 20**. The XRD spectrum of SiO_2 was found a broad peak (low crystallinity) at 2θ = 22.8˚ which is a characteristic of SiO_2. The 2θ value and peak pattern were compared to SiO_2-NH_2 and SiO_2-Cu(II) complex. Apparently, no significantly different peak was observed due to this technique cannot monitor the low concentration of additional APTES and Cu(II) complex as mentioned in FTIR. Even though a high concentration of those two additions was used, it may not follow any changes on/inside the SiO_2. It was only concluded that the main composition of the prepared materials is SiO_2.

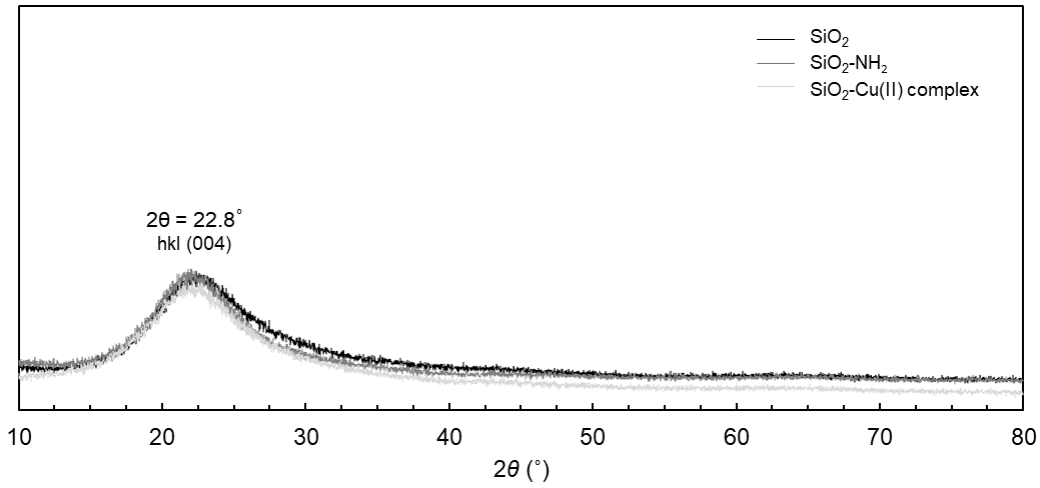

Figure 20 XRD spectra of SiO_2, SiO_2-NH_2, and SiO_2-Cu(II) quinoline complex

2.3 Brunauer–Emmett–Teller study (BET)

The surface properties were studied by N_2 adsorption-desorption isotherm at 77 K (-196 ˚C). **Figure 21** displays the adsorption-desorption isotherm of all synthesized materials. All prepared materials exhibited irreversible type II adsorption-desorption isotherm with an H2-type hysteresis loop indicating a neck-like and wide pore in the partial pressure range from 0.40-0.74 [121]. The amount of adsorbed nitrogen decreases from 275 to 111 cm^3/g_{cat} (for SiO_2-NH_2) and 44.7 cm^3/g_{cat} (for SiO_2-Cu(II) quinoline complex). The reduced values suggest the pore plugging after the functionalization with amino groups and the Cu(II) complex immobilization [97].

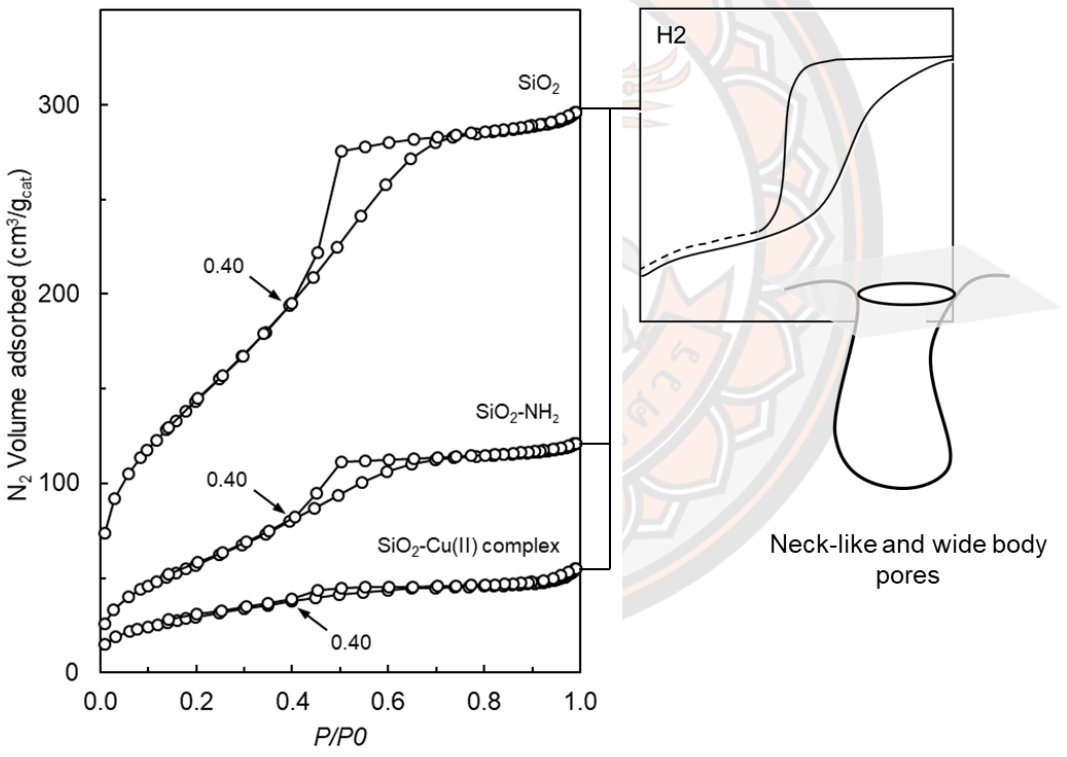

Figure 21 N_2 adsorption-desorption isotherms of SiO_2, SiO_2-NH_2 and SiO_2-Cu(II) complex

Table 3 Textural properties of SiO_2, SiO_2-NH_2 and SiO_2-Cu(II) complex

Sample	S_{BET} (m^2/g)	V_{pmeso} (cm^3/g)	dp (nm)
SiO_2	527.3	0.41	3.36
SiO_2-NH_2	216.4	0.16	3.23
SiO_2-Cu(II) complex	103.6	0.050	2.97

Table 3 listed some textural properties of all synthesized materials. The numbers of specific surface area (S_{BET}) were calculated from nitrogen sorption studies by applying the BET equation. The BET surface area of SiO_2 was 527.3 m^2/g which is greater than commercial silica [122]. The values of the specific surface area of SiO_2-NH_2 and SiO_2-Cu(II) quinoline complex were 216.4 and 103.6 m^2/g, respectively. The pore volume (V_{pmeso}) and the pore size distributions (dp) of all materials were calculated from the adsorption branch of the N_2 isotherm by using the Barrett–Joyner–Halenda (BJH) model. The V_{pmeso} and pore size of each one was decreased and corresponded to the H2 hysteresis loop showing a characteristic of mesoporous material. These findings suggest that no changes in pore size after the functionalization with amino groups and the Cu(II) complex immobilization.

2.4 Field emission scanning electron microscopy (FESEM)

As mentioned, the sequential preparation of silica in this present work followed the method described by KS. Rao et al. The silica nanoparticles were prepared using ultrasonication by sol-gel process. The effect of different reagents such as ammonia, ethanol, water, and TEOS was studied in detail. Various-sized particles were obtained in the range of 20-460 nm. It was obtained in monodisperse and uniform-size particles. The optimal condition (Sample-2) was used and modified for the preparation of silica as support.

Figures 22-24 show SEM images of the SiO_2, SiO_2-NH_2, and SiO_2-Cu(II)-quinoline complex. The SiO_2 (**Figure 22**) was in a spherical shape and had different degrees of aggregation less than 100 nm, which was in accordance with

several works [123-126]. It can be considered that the aggregated particles were obtained because the reaction was performed in a medium with a high concentration of water (14 mol L^{-1}). In addition, the concentration of ammonia was relatively low (1.4 mol L^{-1}) to protect the aggregation of the silica [101]. As seen in **Figures 23-24**, there was no significant change of morphology of the synthesized silica after the amine-functionalization and the immobilization processes. Only larger aggregations of silica were observed.

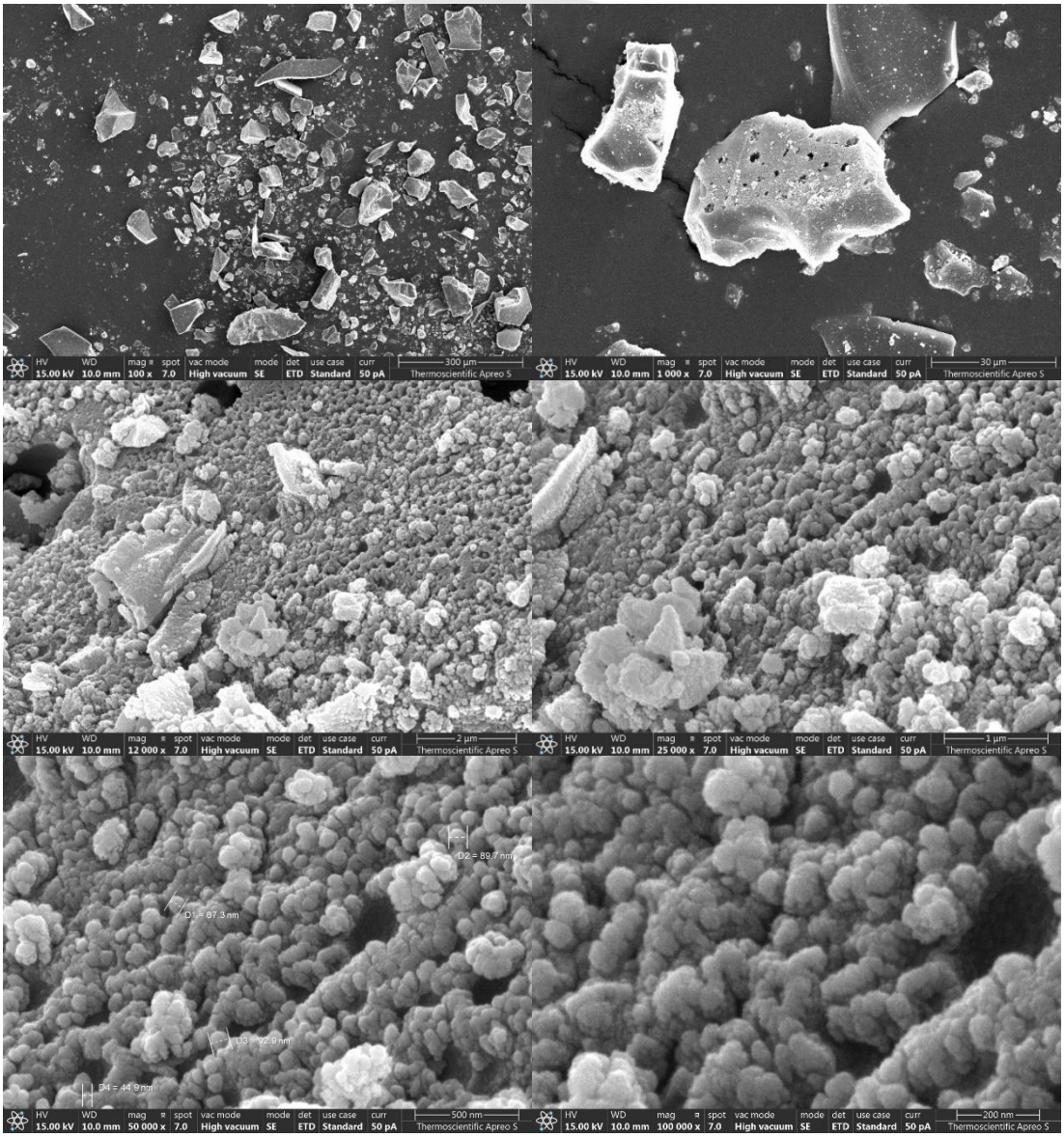

Figure 22 The SEM images of SiO_2

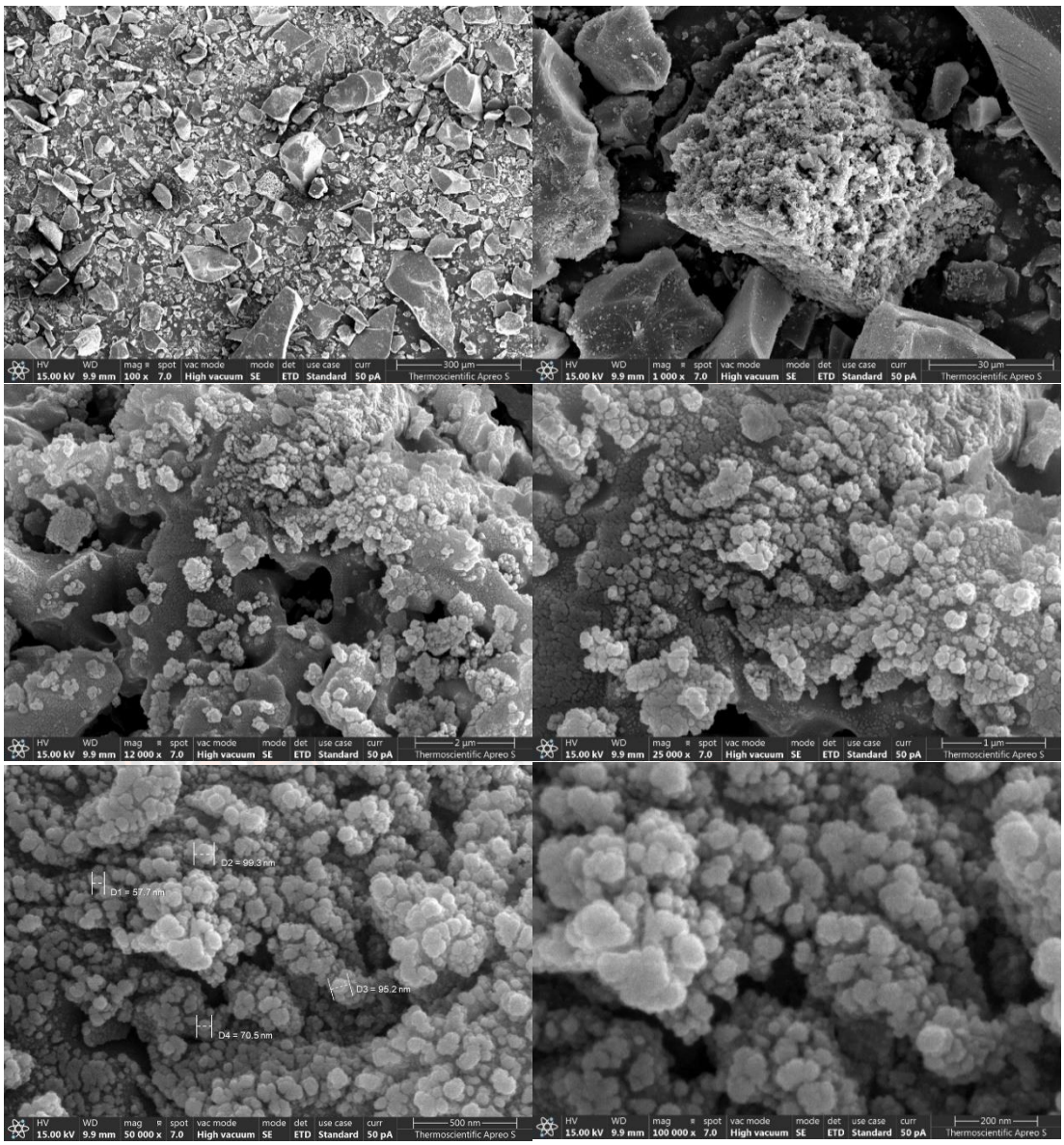

Figure 23 The SEM images of SiO_2-NH_2

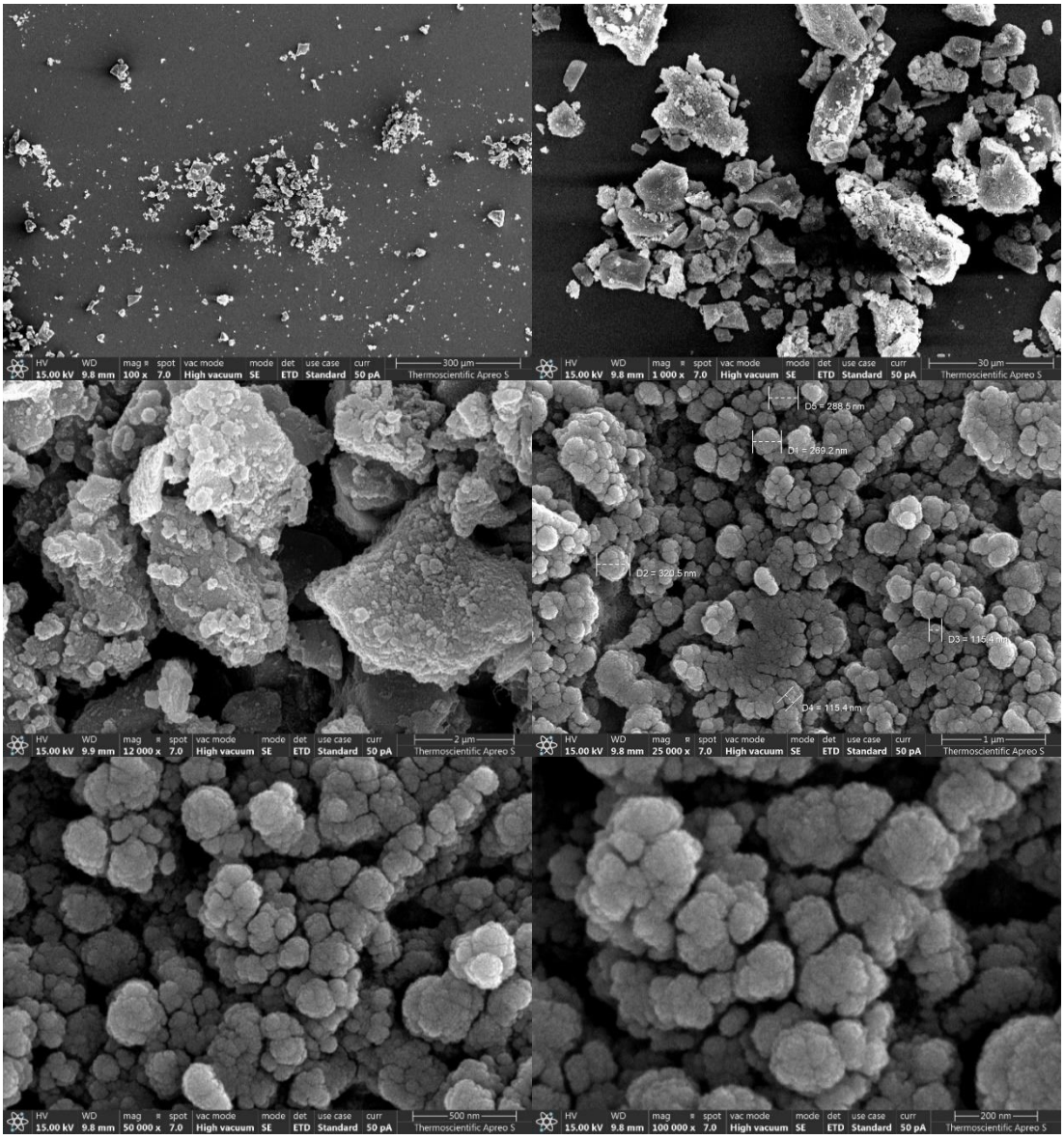

Figure 24 The SEM images of SiO_2-Cu(II) complex

2.5 Energy dispersive spectroscopy (EDS)

The elemental composition of Cu(II)-quinoline complex immobilized on silica support was investigated using energy dispersive X-Ray (EDX). EDX or EDS is an X-ray technique used to identify the consistent elements in materials. The equipment is an attachment of electron microscopy instruments. To stimulate the emission of characteristic X-rays from a sample, ground state electrons bound to the nucleus are excited and ejected from electron shells followed by creating an electron-hole. An electron from an outer then fills the hole and emits the difference in energy between those two levels in the form of an X-ray. As the energies of the X-rays are characteristic, EDS allows the elemental composition of a sample to be measured [127].

The EDX elemental mapping demonstrated that elements Si (red), C (purple), O (green), N (blue), and Cu (yellow) are uniformly distributed within the material surface (**Figure 25**). These results evidenced Cu is well anchored on the surface of the silica support.

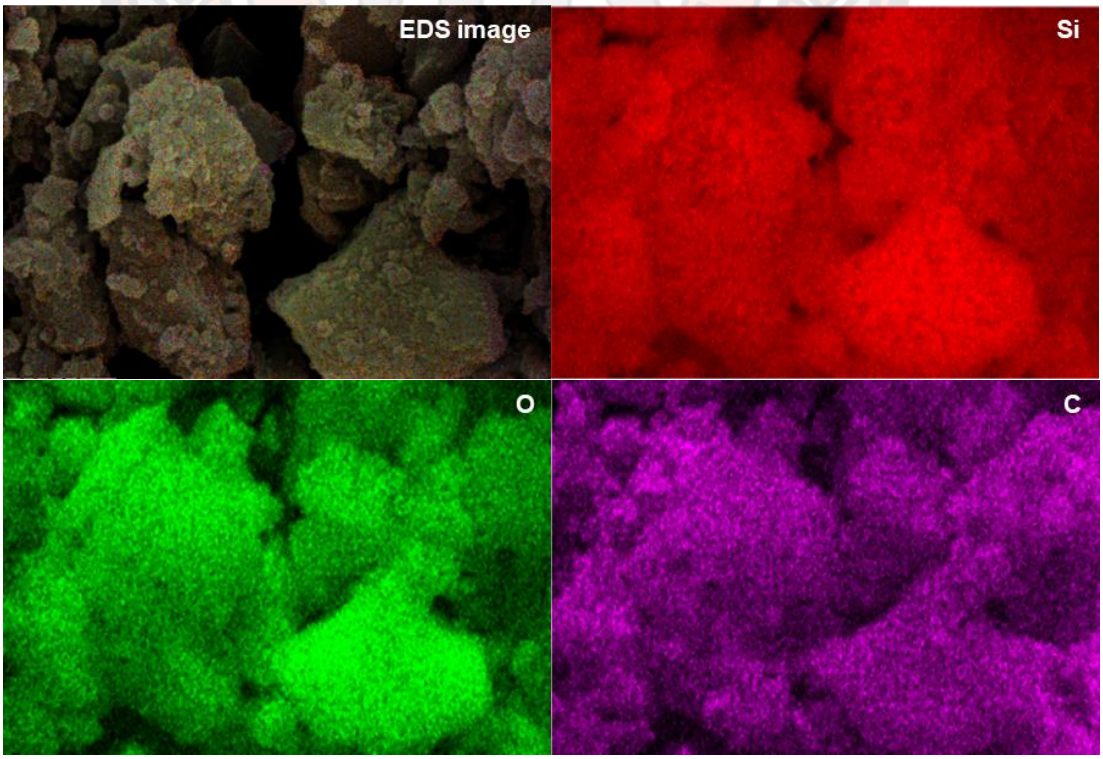

Figure 25 The EDX mapping of SiO_2-Cu(II)-quinoline complex

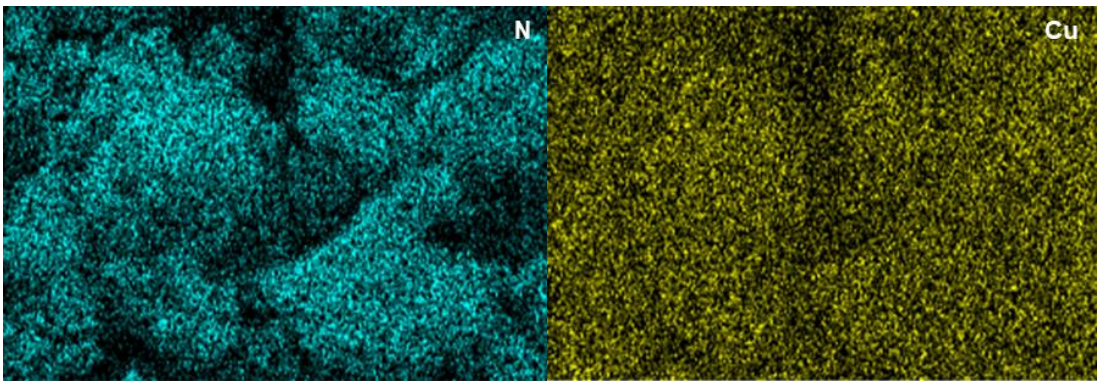

Figure 25 Cont.

In the EDS spectrum (**Figure 26**), peaks at 0.277, 0.392, 0.523, and 1.704 keV related to C, N, O, and Si, respectively. In addition, two peaks of Cu were found at 0.930 and 8.040 keV. The total copper content on the selected area was found to be 0.6 wt.%.

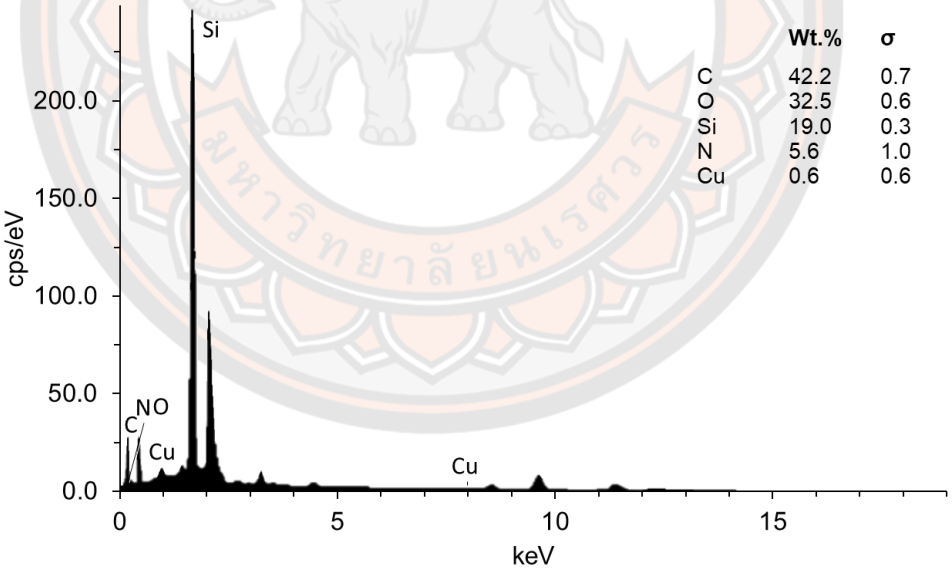

Figure 26 The EDX spectrum of SiO_2-Cu(II)-quinoline complex

2.6 X-ray photoelectron spectroscopy (XPS)

Figure 27 shows the results of XPS spectra SiO_2-quinoline before and after loading Cu(II). The peaks at bond energy (BE) of 103 eV, 285 eV, 399 eV, and 532 eV correspond to the Si 2p, C 1s, N 1s, and O 1s spectra, respectively. It is observed that after loading Cu(II), a new peak with a binding energy of 935 eV appeared, which could be assigned to the Cu 2p orbital. The high-resolution XPS spectra of N 1s and Cu 2p regions were used to further clarify the surface chemical state of the copper element.

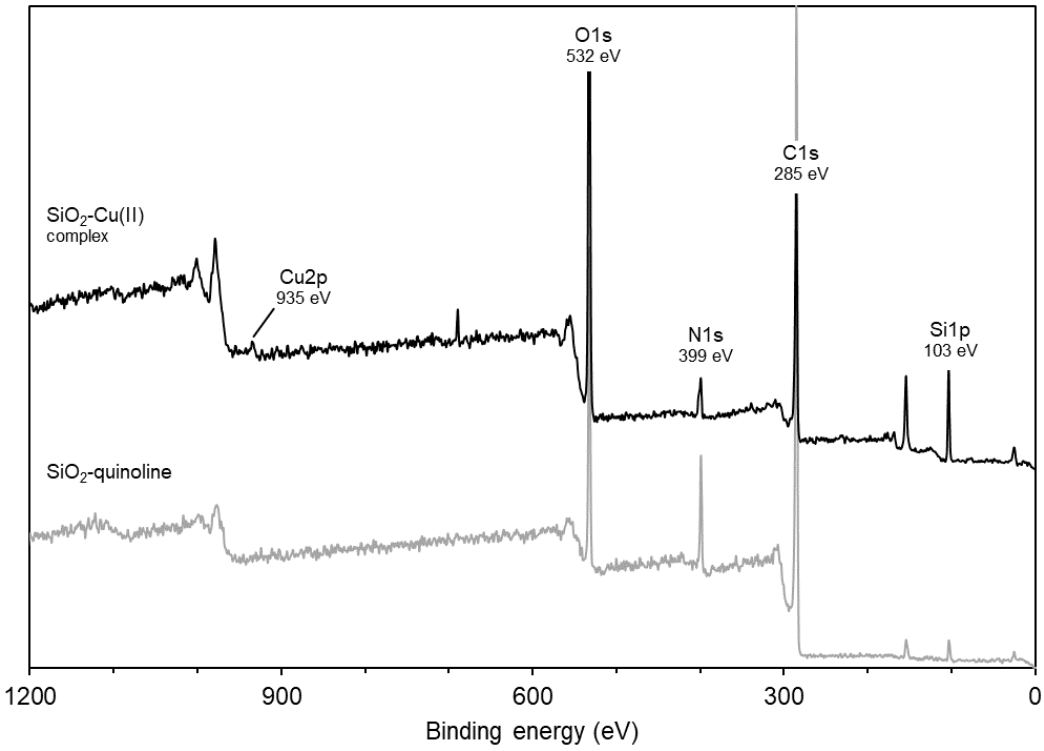

Figure 27 XPS survey spectra of SiO_2-quinoline before (below) and after loading Cu(II) (top)

Figure 28 shows that the strong Cu 2p1/2 and Cu 2p3/2 peaks occurred at 952.1 and 932.3 eV. The BE of 932.3 eV for Cu 2p3/2 is in agreement with its oxidation states +2.

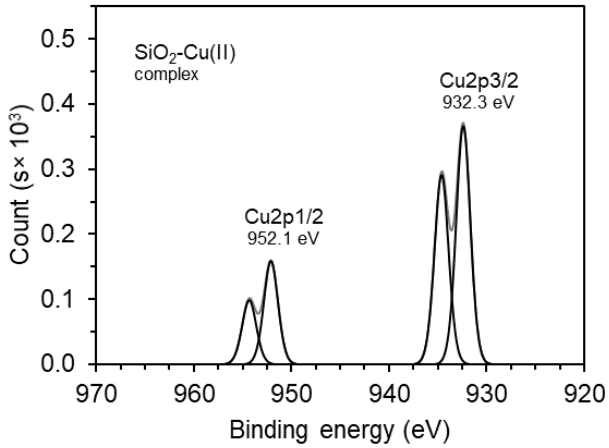

Figure 28 The high-resolution XPS for Cu 2p of SiO_2-quinoline after loading of Cu(II)

N 1s core-level spectra are displayed in **Figures 29-30**. BEs of 399.1 eV and 400.1 eV were found in SiO_2-quinoline. The peak of 399.1 eV can be assigned to nitrogen in the aromatic ring while the peak with BE of 400.1 eV can be assigned to nitrogen in primary amines or imines [128-130]. After loading Cu(II) ions, BEs of N 1s in SiO_2-quinoline shifted to 399.2 eV and 400.4 eV, respectively (**Figure 30**). The increases and changes in BEs of N 1s indicate that the lone pair electrons in the nitrogen atoms were donated or in a different position to Cu(II) ions.

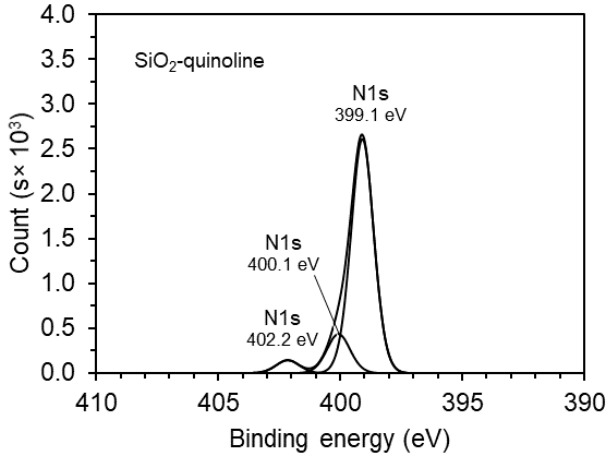

Figure 29 The high-resolution XPS for N 1s of SiO_2-quinoline before loading of Cu(II)

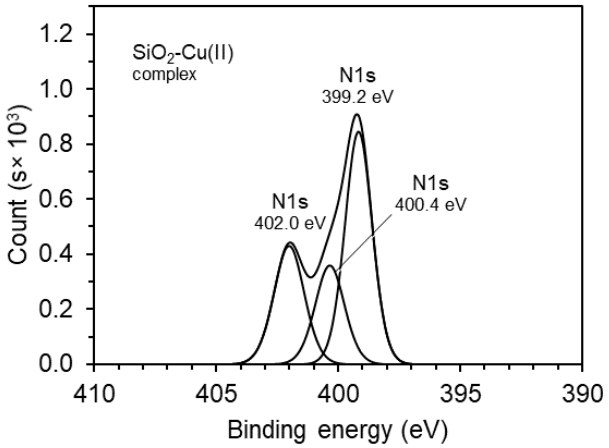

Figure 30 The high-resolution XPS for N 1s of SiO_2-quinoline after loading of Cu(II)

2.7 Diffuse reflection spectroscopy (DRS)

Diffuse reflectance relies upon the focused projection of light into the sample. The light is reflected, scattered, and transmitted through the sample material. Some of which is absorbed by the sample. Only a part of the beam that is scattered in a sample and returned to the surface is considered as diffuse reflection. The reflectance data can be converted to light absorption of the sample [131].

Determination of band gap in materials is very important for a semiconductor or a photocatalyst. Band gap or energy gap (Eg) indicates the difference in energy between the top of the valence band filled with electrons and the bottom of the conduction band devoid of electrons [132]. The band gap was measured using the reflection spectra observed in the wavelength range 200-800 nm. **Figure 31** displays the spectra of SiO_2 and SiO_2-Cu(II) complex with a different pattern.

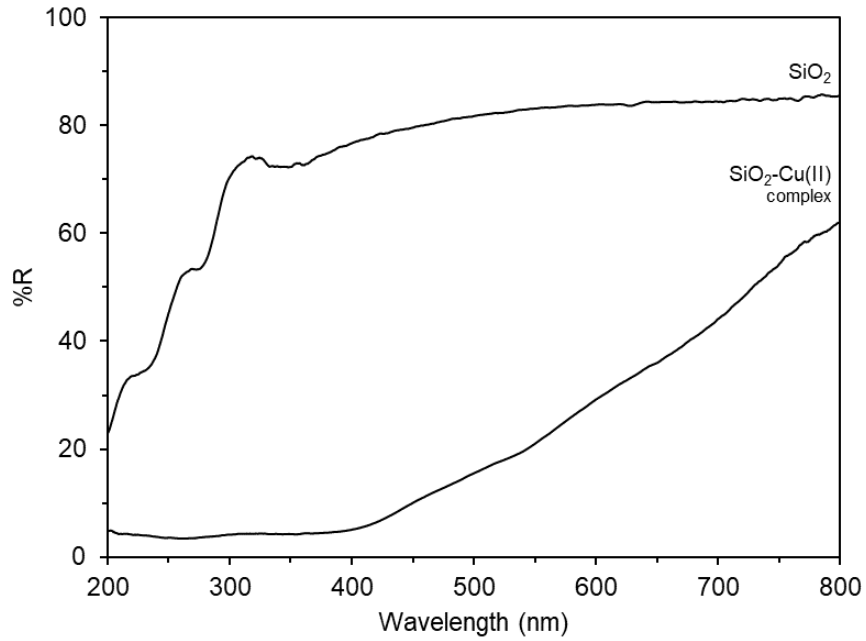

Figure 31 DRS spectra of SiO_2 (top) and SiO_2-Cu(II)-quinoline complex (below)

To calculate an indirect band gap, Kubelka-Munk model was used for the investigation of the band gap [128, 133]. The Kubelka-Munk equation is expressed as a following formula;

$$F(R) = (1 - R)^2/2R$$

where R is the absolute reflectance of the sampled layer.

Figure 32-33 presents the estimated band gap from the plot of $(1–R)^2/2R$ versus *hv* for SiO_2 and SiO_2-Cu(II)-quinoline complex. The calculated band gap energy of SiO_2 was found to be 5.8 eV. The number decreased after the immobilization of Cu(II)-quinoline complex. The band gap energies were found at two positions of 2.8 and 3.5 eV. The results indicate that the addition of Cu(II)-quinoline complex onto the surface of SiO_2 can reduce the band gap to the region of UV light.

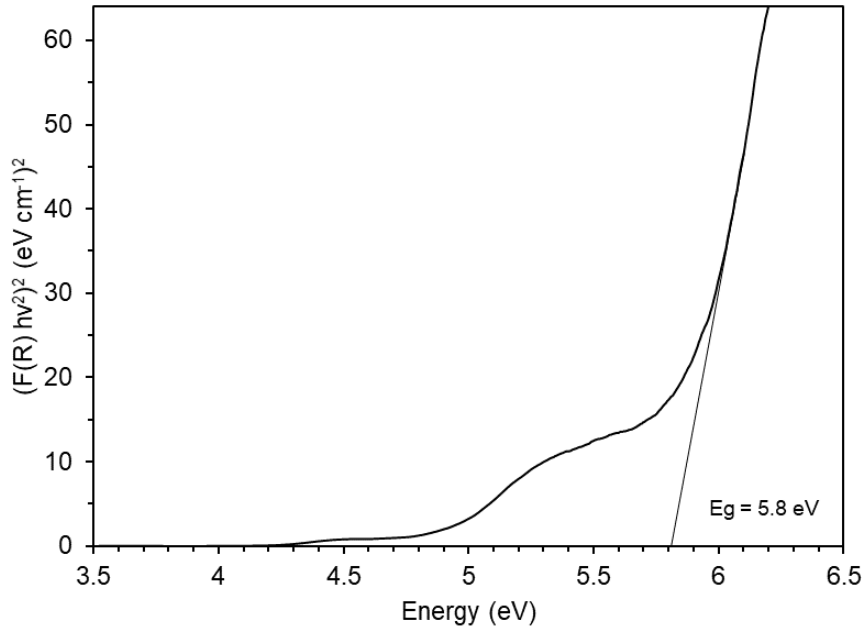

Figure 32 Kubelka Munk function of SiO_2

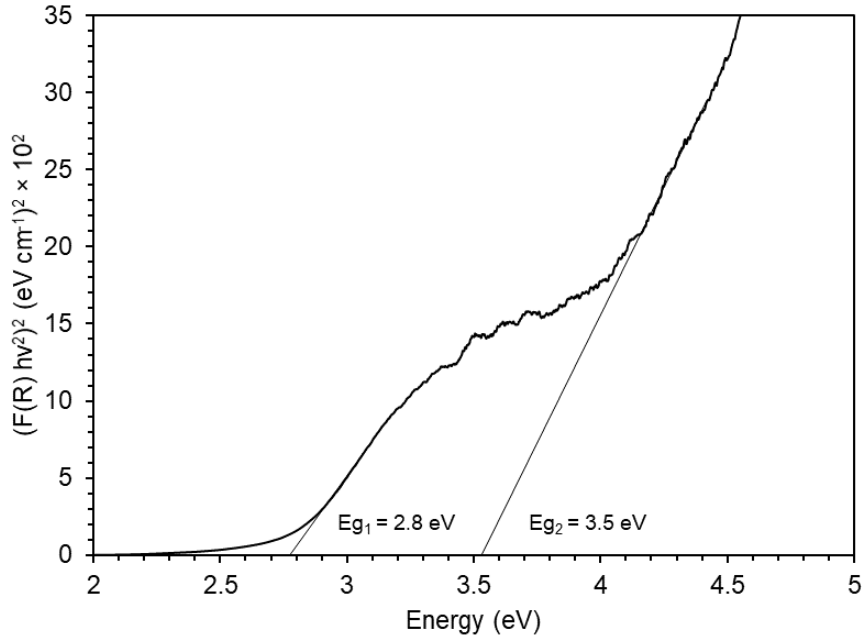

Figure 33 Kubelka Munk function of SiO_2-Cu(II)-quinoline complex

3. Degradation of methylene blue

3.1 Contact time of the silica support and the catalyst

The heterogeneous photocatalytic reaction is operated on the catalyst surface, and pre-adsorption of the target is necessary for their degradation. Therefore, the contact time of MB adsorbed on the surface of the catalyst was investigated.

The effect of contact time on the adsorption capacity of the silica support and the catalyst was determined within the range of 0-150 min under pH 7.0. **Figure 34** shows the result of MB adsorption in the presence of silica support and the catalyst. The y axis is $C/C_0 \times 100$ (%), which represents the removal percentage of MB.

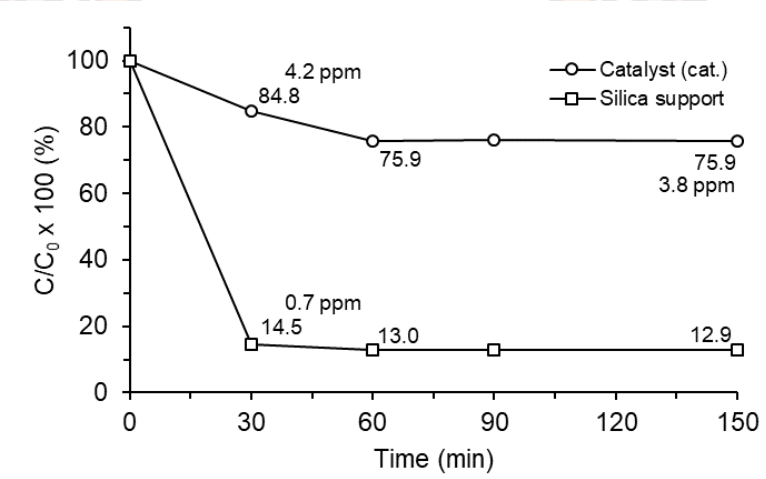

Figure 34 Contact time of MB adsorbed on the surface of the silica support and the catalyst under the selected condition; MB solution, 5 ppm, 5 mL; silica support or cat. 0.2 g L^{-1} (0.0010 g); pH 7.0; 28 ˚C

The initial adsorption was observed within 30 min. This occurrence of rapid adsorption of silica support was related to the high surface area (527.3 m^2/g) as calculated in the BET study. Due to the greater adsorption capacity, 87.1% of MB was removed in 150 min.

On the other hand, only 15.2% of MB was removed by the catalyst, and the equilibrium was finally reached in 60 min. The adsorption rate of the catalyst is lower than the silica support because of the lower surface area (102.3 m^2/g). In addition, the site for the adsorption process decreased by the amino functionalization and the immobilized Cu(II) complex. This unavailable site leads to a slower adsorption rate. Although, the maximum dye removal percentage of the catalyst was found at 60 min. The contact time for the adsorption of MB was used for 30 min in the photocatalysis section.

The adsorption capacity (q_t) was calculated by the following formula [134].

$$q_t = (C_0 - C_t) \times V/ W$$

where C_t is the concentration of MB solution at the reaction time t in mg/L, C_0 is the initial concentration of MB solution at 0 min, V is the volume of MB solution in L, W is the weight of the silica or the catalyst.

It was found that the adsorption capacity of the silica was 21.4 mg/g which is approximately 5.6 times higher than the adsorption capacity of the catalyst (3.8 mg/g).

3.2 Photocatalytic activities for degradation of MB

The catalytic activities of the catalyst were evaluated by degradation of MB under UV light irradiation within 150 min. The concentration of MB was reduced because of possible factors, such as the adsorption, the Fenton-like reaction, and the photo-Fenton-like reaction. Therefore, the control experiments, including MB/cat. (UV) and MB/cat./H_2O_2 (dark), were observed under identical conditions. Generally, the catalytic experiment was carried out under the conditions as following: MB, 5 ppm (5 mL); pH 7.0; 28 ˚C; catalyst loading, 0.2 g L^{-1}.

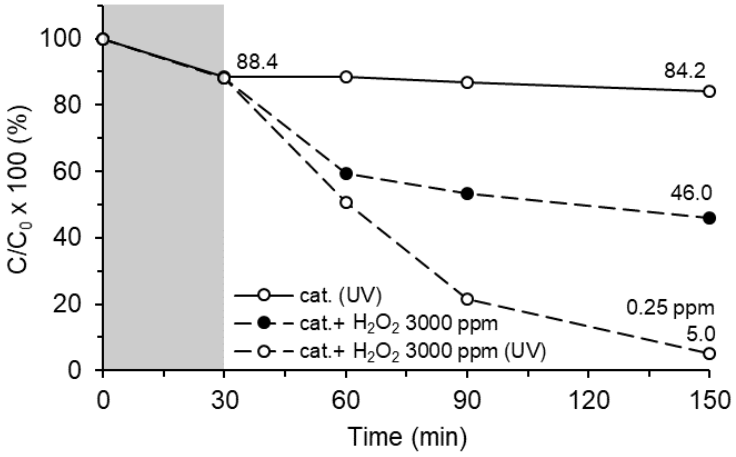

Figure 35 Catalytic efficiency for degradation of MB in different reaction systems under the general condition; MB solution, 5 ppm, 5 mL; cat. 0.2 g L^{-1} (0.0010 g); pH 7.0; 28 ˚C

The time profile of MB degradation over the catalyst in different conditions was shown in **Figure 35**. The y axis in these processes is $C/C_0 \times 100$ (%), which represents the removal percentage of MB in a term of degradation. It was found that MB was hardly decomposed in MB/cat. (UV). Only 15.8% of MB was removed after 150 min of total reaction time. A better result of degradation was found after the addition of H_2O_2. Approximately 54% of MB was degraded through the Fenton-like reactions, as described in Eq. (34)-(37).

$$\equiv L\text{–}Cu^{2+} + H_2O_2 \longrightarrow \equiv L\text{–}Cu^{2+}(O_2H)^- + H^+ \quad (34)$$

$$\equiv L\text{–}Cu^{2+}(O_2H)^- \longrightarrow \equiv L\text{–}Cu^{+}(O_2H)^{\bullet} \quad (35)$$

$$\equiv L\text{–}Cu^{+}(O_2H)^{\bullet} + H_2O_2 \longrightarrow \equiv L\text{–}Cu^{+} + HO^{\bullet} + O_2 + H_2O \quad (36)$$

$$\equiv L\text{–}Cu^{+} + H_2O_2 \longrightarrow \equiv L\text{–}Cu^{2+} + HO^{\bullet} + HO^- \quad (37)$$

Note: Cu-organic ligand immobilized on the silica support; ≡L–Cu.

The best result was observed when MB/catalyst/H_2O_2 was operated under UV light irradiation. The concentration of MB was significantly decreased to 5% within 150 min. The catalyst performed as a photo-Fenton-like catalyst in the

presence of H_2O_2. The radicals were generated through the reaction as described in Eq. (38)-(42) [57].

$$\equiv L–Cu^{2+} + h\nu \longrightarrow \equiv L^{+\bullet}–Cu^{\bullet 2+} \quad (38)$$

$$\equiv L^{+\bullet}–Cu^{\bullet 2+} \longrightarrow \equiv L^{+\bullet}–Cu^{+} \quad (39)$$

$$\equiv L^{+\bullet}–Cu^{+} \longrightarrow \equiv L–Cu^{2+} + \text{heat} \quad (40)$$

$$\equiv L^{+\bullet}–Cu^{+} + H_2O_2 \longrightarrow \equiv L^{+\bullet}– Cu^{2+} + HO^{\bullet} + HO^{-} \quad (41)$$

$$\equiv L^{+\bullet}– Cu^{2+} + Sub \longrightarrow \equiv L– Cu^{2+} + Sub^{*} \quad (42)$$

The reaction was allowed because UV light enhanced the catalytic capacity of the catalyst. In the heterogeneous photocatalytic system, the photo-induced reductive dissolution of the catalyst was performed [135, 136]. Firstly, the conversion of light into chemical energy was operated by the photoinduced charge separation (Eq. (38)). It is also called a charge transfer process from organic ligand to metal (Eq. (39)), which results in the oxidized form of the ligand ($L^{+\bullet}$) and the reduced form of the metal ion (Cu^{+}). The original form ($\equiv L–Cu^{2+}$) also performs in the reaction by Fenton-like reaction to generate the radicals (Eq. (41)). During these processes, dyes could be excited by the substrate to metal charged transfer (SMCT) process (E1. (42)). This result contributed to the degradation of dyes via the loss of conjugation of the double bonds in the molecule. In addition, the dye was also oxidized by the radical generated through this photo-Fenton-like reaction. Moreover, the radical intermediate could react with another H_2O_2 molecule to give the radicals and result in the improvement in the degradation of MB.

The photocatalytic activity was investigated quantitatively by the calculation of the apparent rate constant (*k*) of the catalyst. When the concentration of organic dye is low, the process of photodegradation accords with a pseudo-first-order kinetic equation:

$$-\ln(C_t/C_{30}) = kt$$

where C_t is the concentration in mg/L of MB solution at the reaction time t, C_{30} is the concentration of MB solution at 30 min, *k* is the apparent reaction rate constant.

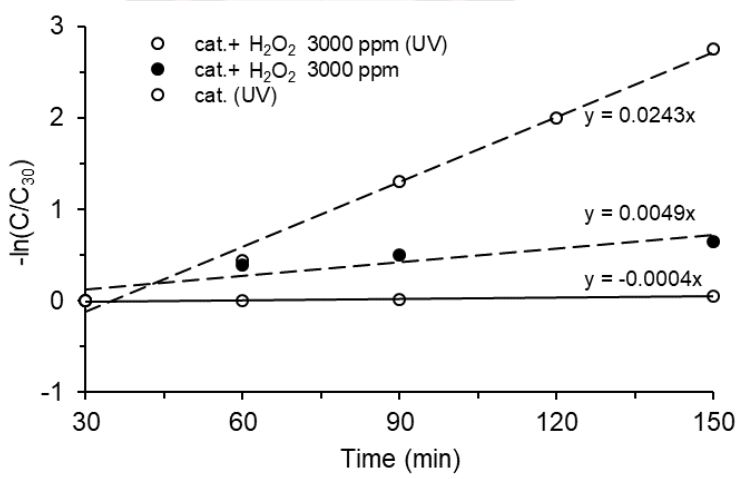

Figure 36 Pseudo-first-order kinetic plot for degradation of MB in different reaction systems under the general condition; MB solution, 5 ppm, 5 mL; cat. 0.2 g L^{-1} (0.0010 g); pH 7.0; 28 ˚C

The slope (*k* value in min^{-1}) was obtained by the linear plot of $-\ln(C_t/C_{30})$ with t, as shown in **Figure 36**. The *k* values of MB/cat. (UV), MB/cat./H_2O_2 (dark) and MB/cat./H_2O_2 (UV) were -0.04, 0.49 and 2.43 (10^{-2} min^{-1}), respectively. It was confirmed that the reaction rate was enhanced in the presence of MB/cat. combined with H_2O_2 under UV light irradiation.

Figure 37 displays the temporal changes of UV-vis spectra of MB in the MB/catalyst/H_2O_2 (UV) system. In general, the UV-vis spectra of MB showed only one characteristic band at 662 nm in the visible region (400-800 nm). The band was attributed to a conjugated structure formed by the thiazine center with two rings of benzene. This structure allows the electronic transition due to the π-π* transition associated with the resonance of the π electrons in the thiazine [137, 138]. In this present study, the maximum absorption band of MB in the visible region was decreased dramatically in 150 min with no new absorption band appearing and was not shifted to a shorter wavelength. This result indicates that the chromophore in the molecule of MB was decomposed during the reaction [139, 140].

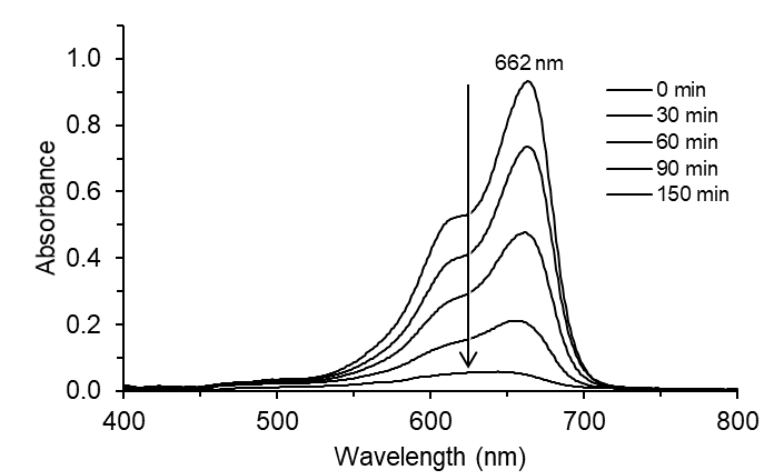

Figure 37 Changes in spectra of MB in the photo-Fenton-like reaction under the selected condition; MB solution, 5 ppm, 5 mL; cat. 0.2 g L^{-1} (0.0010 g); H_2O_2, 3000 ppm; pH 7.0; 28 ºC; UV (30 W)

3.3 Effect of hydrogen peroxide concentration

The time profile and the pseudo-first-order kinetic model of MB degradation were displayed in **Figure 38-39**. The *k* values for MB degradation increased with hydrogen peroxide content from – 0.07 to 2.35 × 10^{-2} min^{-1}. Meanwhile, the degradation efficiency in 2.50 h increased from 15.8% to 95.0%. As the increased rate of reaction, an alternative way for the reaction might happen with lower activation energy (E_a). This finding suggests that H_2O_2 performs as the second catalyst cooperating with the SiO_2-Cu(II) complex.

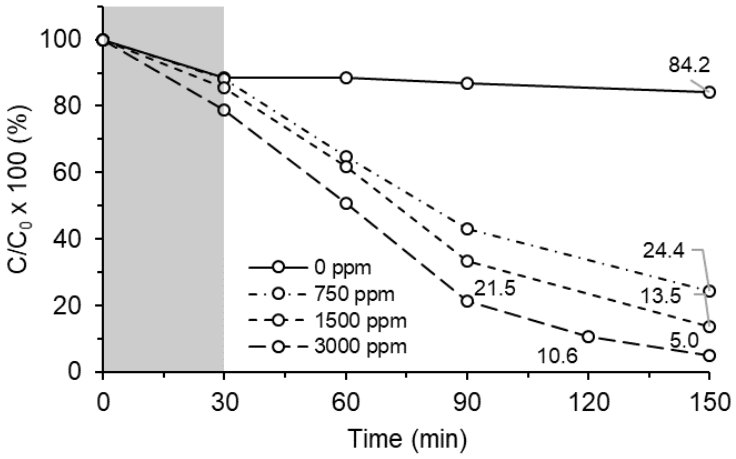

Figure 38 Catalytic efficiency for degradation of MB in different concentration of H_2O_2 under the general condition; MB solution, 5 ppm, 5 mL; cat. 0.2 g L^{-1} (0.0010 g); pH 7.0; 28 ˚C; UV (30W)

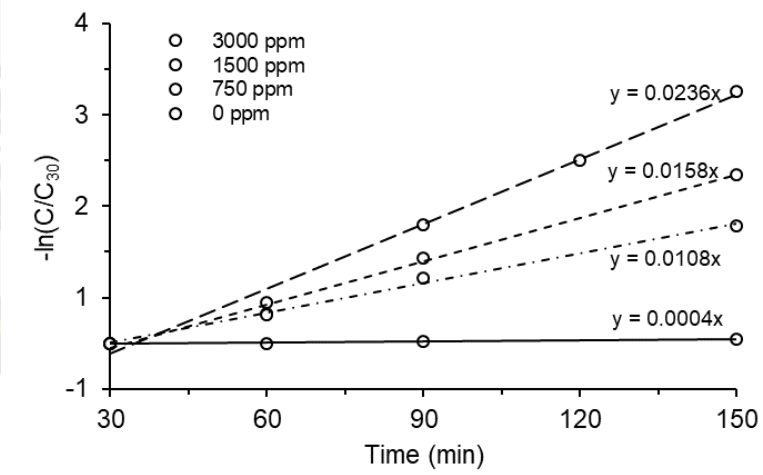

Figure 39 Pseudo-first-order kinetic plot for MB degradation in different concentration of H_2O_2 under the general condition; MB solution, 5 ppm, 5 mL; cat. 0.2 g L^{-1} (0.0010 g); pH 7.0; 28 ˚C; UV (30W)

3.4 Active species trapping experiments

Various radical species involved in the Fenton-base reaction were found. The possible active species such as hydroxyl radicals ($HO^{\bullet}$), and superoxide radicals ($O_2^{\bullet-}$) were detected as a key role in the Fenton process. Therefore, the type of radical species in the MB degradation was determined by coumarin, IPA, and p-BQ.

Coumarin

Coumarin is a poorly fluorescent molecule that was used as a probe for detection of the HO•. The highly fluorescent compound, 7-hydroxycoumarin, was produced by the reaction between coumarin and HO•, as shown in **Scheme 21**. The amount of 7-hydroxycoumarin reflects the amount of generated HO• in the system.

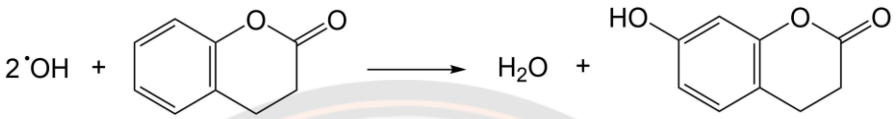

Scheme 21 Formation of 7-hydroxycoumarin by the reaction between coumarin and hydroxyl radicals

The variation of fluorescence intensity with the reaction time (0-150 min) was shown in **Figures 40**-**41**. Firstly, there was an emission band of coumarin at 400 nm with an intensity of 150 (**Figure 40**). It can be observed that there was no change in the spectrum at 30 min compared to 0 min. After exposing the UV light for 30 min (60 min of the total reaction time), coumarin was hydroxylated to 7-hydroxy-coumarin. The strong emission band at 460 nm was observed as shown in **Figure 41**. The band increased continuously upon the exposure time. The fluorescence intensity of 150 min reaction time was steadily increased at maximum with the intensity of approximately 6,000 (**Figure 42**). Also, it was highly enhanced when compared to without the irradiation of UV light. These results suggest that the HO• was generated by the condition of catalyst/H_2O_2 under UV irradiation.

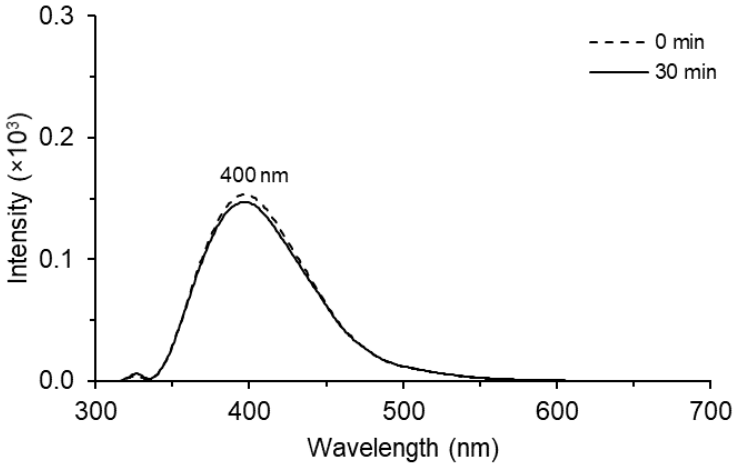

Figure 40 Changes in fluorescence spectrum of coumarin in 0-30 min under the selected condition; coumarin solution, 1 mM (5 mL); cat. 0.2 g L^{-1} (0.0010 g); H_2O_2, 3000 ppm; pH 7.0; 28 ºC; UV (30 W)
ex. 332 em. 456 nm

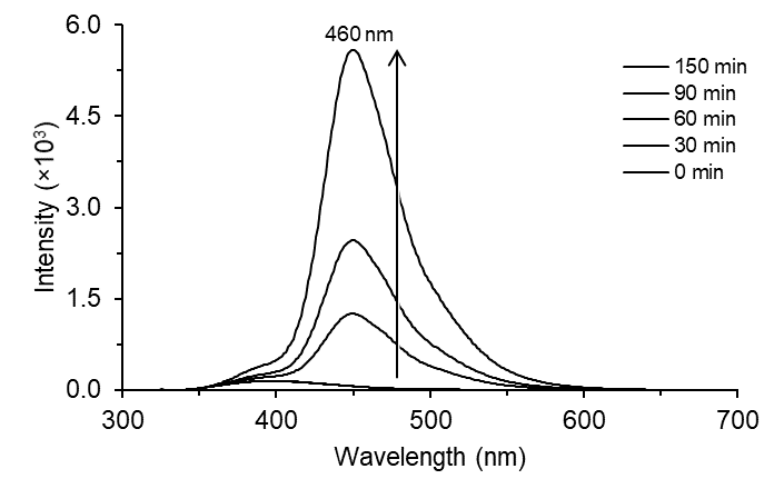

Figure 41 Changes in fluorescence spectrum of coumarin in 0-150 min under the selected condition; coumarin solution, 1 mM (5 mL); cat. 0.2 g L^{-1} (0.0010 g); H_2O_2, 3000 ppm; pH 7.0; 28 ºC; UV (30 W)
ex. 332 em. 456 nm

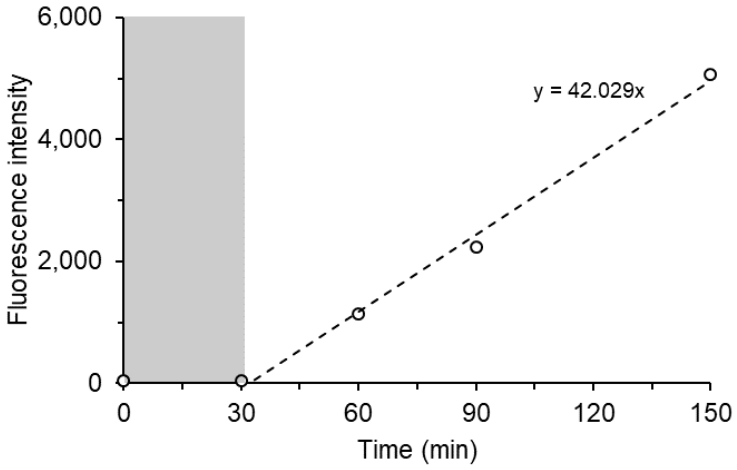

Figure 42 Fluorescence intensity of 7-hydroxycoumarin in 0-150 min under the selected condition; coumarin solution, 1 mM (5 mL); cat. 0.2 g L^{-1} (0.0010 g); H_2O_2, 3000 ppm; pH 7.0; 28 ^oC; UV (30 W) ex. 332 em. 456 nm

Isopropyl alcohol (IPA)

IPA (isopropanol) is an aliphatic alcohol, which is known as an $HO^{\bullet}$ scavenger [141]. It was commonly used as a competitor in the degradation processes. The corresponding reactions can be described in **Scheme 22**.

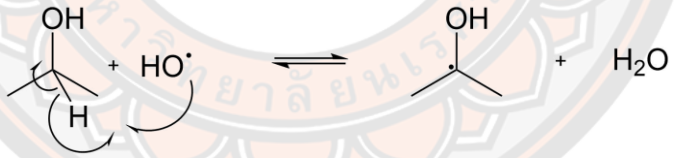

with $k = 2 \times 10^9\ M^{-1}\ s^{-1}$

Scheme 22 Hydrogen abstraction of IPA

0.1 M and 0.3 M of IPA were used to detect the hydroxyl radical involved in the reaction. The experiments were carried out under the same reaction condition of MB/cat./H_2O_2 (UV) except for the addition of IPA before the irradiation of UV light. As shown in **Figure 43**, the photocatalytic degradation efficiency was not influenced by the presence of IPA at both concentrations. The $\ln(C/C_{30})$ was plotted against time displaying the linear relationship as seen in **Figure 44**. The rates of reactions with/without the addition of IPA were not different. This finding suggests

that HO• maybe not a major active radical species influenced in this MB degradation under the selected condition.

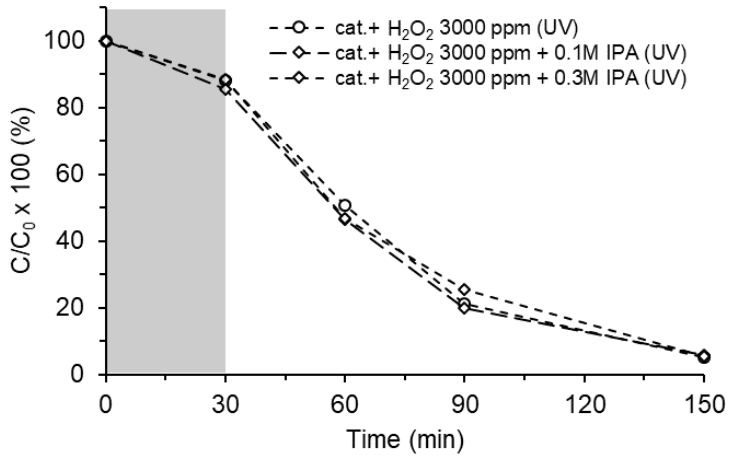

Figure 43 Catalytic efficiency of the catalyst in the presence of IPA under the selected condition; MB solution, 5 ppm, 5 mL; cat. 0.2 g L^{-1} (0.0010 g); H_2O_2, 3000 ppm; pH 7.0; 28 ºC; UV (30 W), IPA 0.1 and 0.3 M

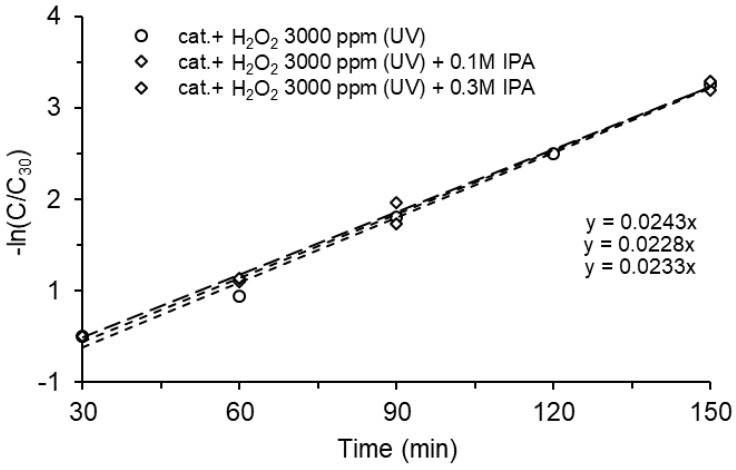

Figure 44 Pseudo-first-order kinetic plot of the catalyst in the presence of IPA under the selected condition; MB solution, 5 ppm, 5 mL; cat. 0.2 g L^{-1} (0.0010 g); H_2O_2, 3000 ppm; pH 7.0; 28 ºC; UV (30 W), IPA 0.1 and 0.3 M

p-Benzoquinone (BQ)

There are several scavengers for the determination of superoxide radicals. For its competition-based detection, terephthalic acid [142], superoxide dismutase (enzyme) [143], benzoic acid [144], and *p*-BQ [143, 145-147] was used as a basic scavenger. The simple one, *p*-BQ was used for the determination of the role of $O_2^{\bullet-}$. The hydroquinone was generated by the reaction of *p*-BQ with the superoxide anion, as shown in **Scheme 23**.

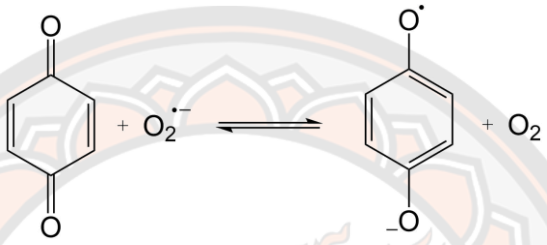

with $k = 9.8 \times 10^8\ M^{-1}\ s^{-1}$ [148]

Scheme 23 Proposed reaction of *p*-BQ with $O_2^{\bullet-}$

The experiments were carried out under the same reaction condition of MB/cat./H_2O_2 (UV) except for the addition of *p*-BQ before the irradiation of UV light. The active species trapping result was shown in **Figure 45**.

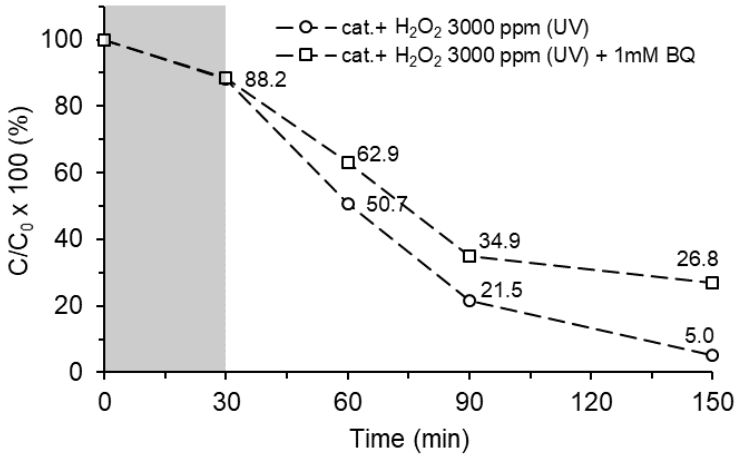

Figure 45 Catalytic efficiency of the catalyst in the presence of *p*-BQ under the selected condition; MB solution, 5 ppm, 5 mL; cat. 0.2 g L^{-1} (0.0010 g); H_2O_2, 3000 ppm; pH 7.0; 28 ºC; UV (30 W), *p*-BQ 1 mM

The photocatalytic degradation efficiency was influenced by the presence of *p*-BQ. The $\ln(C/C_{30})$ was plotted against time displaying the linear relationship as seen in **Figure 46**. The *k* value for MB degradation was decreased to 0.88×10^{-2} min^{-1} (2.7 times lower) compared to the control (2.36×10^{-2} min^{-1}). Therefore, this result suggests that $O_2^{\bullet-}$ was involved in the degradation of MB.

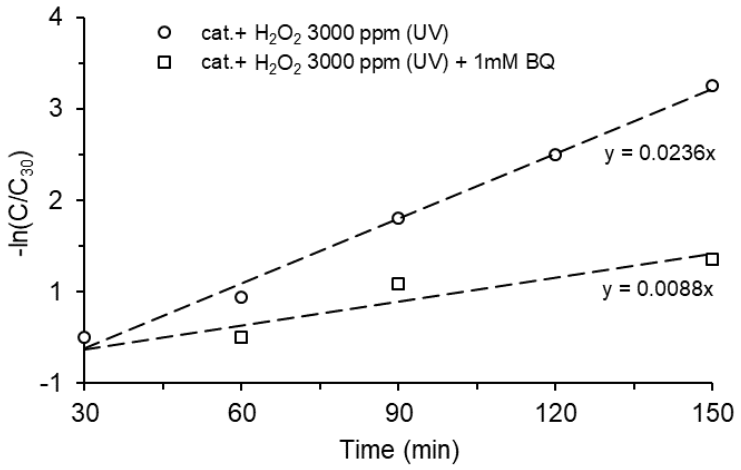

Figure 46 Pseudo-first-order kinetic plot of the catalyst in the presence of *p*-BQ under the selected condition; MB solution, 5 ppm, 5 mL; cat. 0.2 g L^{-1} (0.0010 g); H_2O_2, 3000 ppm; pH 7.0; 28 ºC; UV (30 W), *p*-BQ 1 mM

Although, $HO^{\bullet}$ was not found in the radical trapping experiment of IPA. It was still involved in the MB degradation as confirmed by the production of 7-hydroxycoumarin. In addition, $O_2^{\bullet-}$ trapped by *p*-BQ was interesting because of its competitiveness in MB degradation. 95.0% of MB degradation found in the control experiment was decreased to 73.2% in 2.5 h. This finding suggests that $O_2^{\bullet-}$ plays a key role in MB degradation using the prepared catalyst. As a result, the mechanism of the catalyst performed in the photo-Fenton-like reaction was purposed in **Scheme 24** [149].

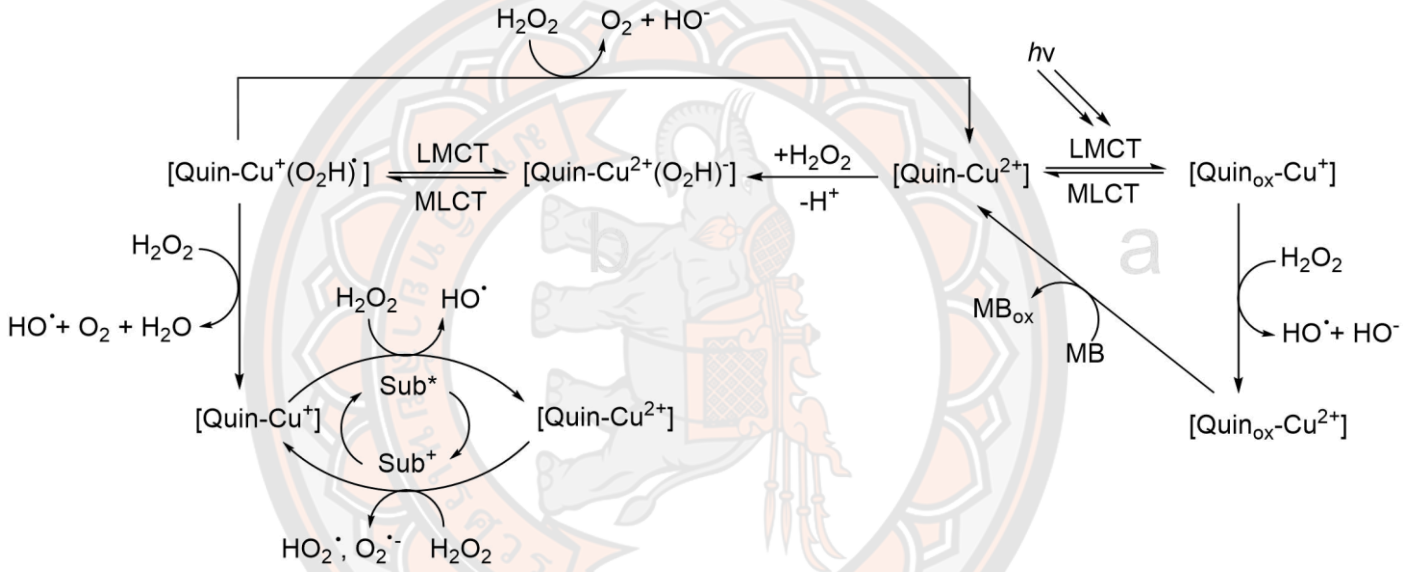

Scheme 24 Proposed mechanisms involved in heterogeneous Cu-quinoline complexes photo-Fenton-like systems

3.5 Photocatalytic stability

The photocatalytic stability of the prepared catalyst was performed by two consecutive experiments at the same reaction condition. **Figure 47** compared the result of MB degradation at the first and second runs of the catalysis. MB was removed from the solution by adsorption in dark. A large capacity of the adsorption was found and increased from 19.6% to 76.7% (30 min).

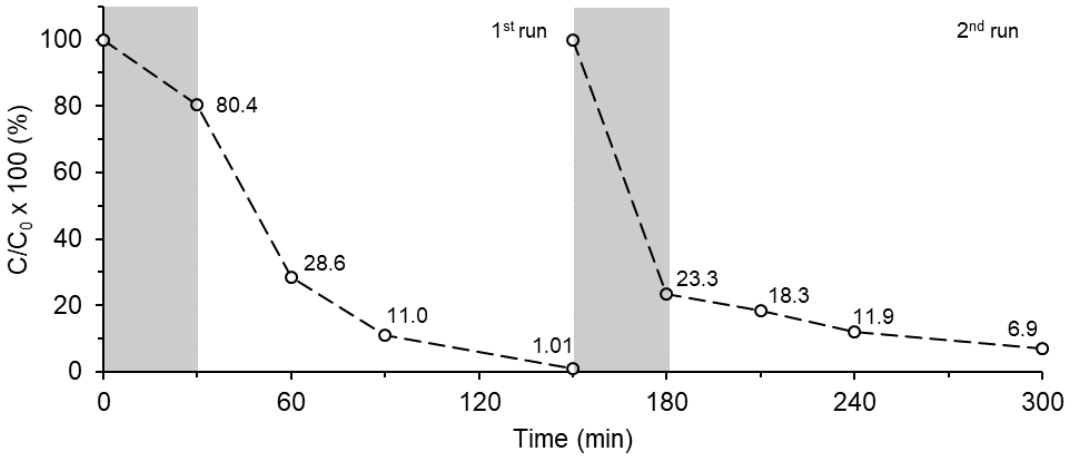

Figure 47 Catalyst stability under the selected condition; MB solution, 5 ppm, 100 mL; cat. 0.2 g L^{-1} (0.0200 g); H_2O_2, 3000 ppm; pH 7.0; 28 ^oC; UV (30 W)

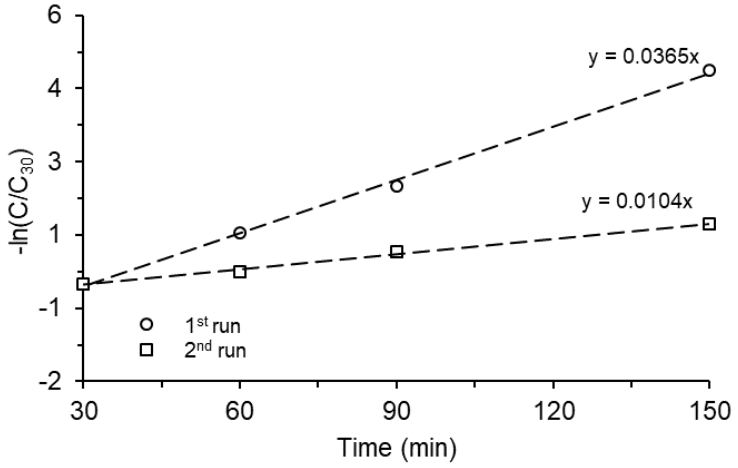

Figure 48 Pseudo-first-order kinetic plot under the selected condition; MB solution, 5 ppm, 100 mL; cat. 0.2 g L^{-1} (0.0200 g); H_2O_2, 3000 ppm; pH 7.0; 28 ^oC; UV (30 W)

This adsorption behavior suggested that the catalytic capacity could be mainly affected by the leaching of active sites on the catalyst surface. On the other hand, there was a loss in a photocatalytic activity that occurred in the second run. The *k* value of the second run was decreased from 3.65×10^{-2} to 1.04×10^{-2} min^{-1}, which was about 3.5 times lower compared to the first run (**Figure. 48**). It can be concluded that the catalyst cannot be reused under this condition because it may be decomposed by self-degradation during the MB degradation.

CHAPTER V

CONCLUSIONS

In conclusion, the new photo-Fenton-like catalyst was prepared by immobilizing a Cu(II) complex with quinoline on a silica support. The catalyst was monitored for the complex immobilization by FTIR, XRD, BET, FESEM, EDS, XPS, and DRS. The results observed from FTIR and XRD were lack of information because the low amount of the additional complex was too low. There were changes on the surface of silica support observed by BET, FESEM, and EDS. The coordination between Cu(II) and quinoline was confirmed by XPS. In addition, the prepared silica support acted as a photocatalyst after the Cu(II)-quinoline complex immobilization confirmed by DRS.

The catalytic activity in the decomposition of hydrogen peroxide for the generation of ROS was performed by heterogeneous degradation of MB under UV light irradiation. 95% of MB (5 mg L^{-1}) was efficiently decolorized in 2.5 h under the experiment's condition; the catalyst, 0.2 g L^{-1}; H_2O_2, 3000 mg L^{-1}; pH 7.0; UV light 30 W. The ROS involved in the MB degradation were $HO^{\bullet}$ and $^{\bullet}O_2^-$ confirmed by the radical trapping experiments. Based on these results, a possible mechanism of the catalyst for MB degradation through a photo-Fenton-like reaction was proposed.

The photocatalytic stability of the catalyst was also determined in two cycles. Unfortunately, there was a loss in the activity of photocatalysis after the first run. Based on the literature, the Cu(II)-quinoline complex may leach out of the surface of silica support. In addition, self-degradation of the catalyst may occur. However, there is still a challenge to develop this catalyst in the future.

REFERENCES

1. Heinz, M., *Dyes, General Survey*, in *Ullmann's Encyclopedia of Industrial Chemistry*. 2014. p. 1-38.
2. Bafana, A., S.S. Devi, and T. Chakrabarti, *Azo dyes: past, present and the future.* Environmental Reviews, 2011. **19**(NA): p. 350-371.
3. Gürses, A., et al., *Classification of Dye and Pigments*, in *Dyes and Pigments*, A. Gürses, et al., Editors. 2016, Springer International Publishing: Cham. p. 31-45.
4. McMullan, G., et al., *Microbial decolourisation and degradation of textile dyes.* Applied Microbiology and Biotechnology, 2001. **56**(1): p. 81-87.
5. Pearce, C.I., J.R. Lloyd, and J.T. Guthrie, *The removal of colour from textile wastewater using whole bacterial cells: a review.* Dyes and Pigments, 2003. **58**(3): p. 179-196.
6. Lee, J.-W., et al., *Evaluation of the performance of adsorption and coagulation processes for the maximum removal of reactive dyes.* Dyes and Pigments, 2006. **69**(3): p. 196-203.
7. Konstantinou, I.K. and T.A. Albanis, *TiO2-assisted photocatalytic degradation of azo dyes in aqueous solution: kinetic and mechanistic investigations: A review.* Applied Catalysis B: Environmental, 2004. **49**(1): p. 1-14.
8. Deng, F., et al., *Visible-light photocatalytic degradation performances and thermal stability due to the synergetic effect of TiO2 with conductive copolymers of polyaniline and polypyrrole.* Nanoscale, 2013. **5**(18): p. 8703-8710.
9. Xu, S., et al., *Visible Light Induced Photocatalytic Degradation of Methyl Orange by Polythiophene/TiO2 Composite Particles.* Water, Air, & Soil Pollution, 2010. **213**(1): p. 151-159.
10. Wang, D., et al., *Sunlight photocatalytic activity of polypyrrole–TiO2 nanocomposites prepared by 'in situ' method.* Catalysis Communications, 2008. **9**(6): p. 1162-1166.
11. Tsuda, S., et al., *DNA Damage Induced by Red Food Dyes Orally Administered to Pregnant and Male Mice.* Toxicological Sciences, 2001. **61**(1): p. 92-99.
12. K Walthall, W. and J. D Stark, *The acute and chronic toxicity of two xanthene dyes, fluorescein sodium salt and phloxine B, to Daphnia pulex*. Vol. 104. 1999. 207-215.
13. Shore, J., *Advances in direct dyes*. Vol. 21. 1996. 1-29.
14. Bafana, A., T. Chakrabarti, and S.S. Devi, *Azoreductase and dye detoxification activities of Bacillus velezensis strain AB.* Applied Microbiology and Biotechnology, 2008. **77**(5): p. 1139-1144.
15. Wanida, C., *Color Removal Technology in Industrial Wastewater.* Burapa Sci. J., 2012. **17**: p. 181-191.
16. Wang, J.L. and L.J. Xu, *Advanced Oxidation Processes for Wastewater*

Treatment: Formation of Hydroxyl Radical and Application. Critical Reviews in Environmental Science and Technology, 2012. **42**(3): p. 251-325.

17. Oturan, M.A. and J.-J. Aaron, *Advanced Oxidation Processes in Water/Wastewater Treatment: Principles and Applications. A Review.* Critical Reviews in Environmental Science and Technology, 2014. **44**(23): p. 2577-2641.
18. Wang, J. and L.E. Jin Xu, *Advanced Oxidation Processes for Wastewater Treatment: Formation of Hydroxyl Radical and Application*. Vol. 42. 2012. 251-325.
19. Garrido-Ramírez, E.G., B.K.G. Theng, and M.L. Mora, *Clays and oxide minerals as catalysts and nanocatalysts in Fenton-like reactions — A review.* Applied Clay Science, 2010. **47**(3): p. 182-192.
20. Feng, J., X. Hu, and P.L. Yue, *Effect of initial solution pH on the degradation of Orange II using clay-based Fe nanocomposites as heterogeneous photo-Fenton catalyst.* Water Research, 2006. **40**(4): p. 641-646.
21. Madhavan, J., et al., *Sonophotocatalytic degradation of monocrotophos using TiO2 and Fe3+*. Journal of Hazardous Materials, 2010. **177**(1): p. 944-949.
22. Sharma, S., M. Mukhopadhyay, and Z.V.P. Murthy, *Treatment of Chlorophenols from Wastewaters by Advanced Oxidation Processes.* Separation & Purification Reviews, 2013. **42**(4): p. 263-295.
23. Ghatak, H.R., *Advanced Oxidation Processes for the Treatment of Biorecalcitrant Organics in Wastewater.* Critical Reviews in Environmental Science and Technology, 2014. **44**(11): p. 1167-1219.
24. Amat, A.M., et al., *Ozonisation coupled with biological degradation for treatment of phenolic pollutants: a mechanistically based study.* Chemosphere, 2003. **53**(1): p. 79-86.
25. Karunakaran, C. and P. Anilkumar, *Semiconductor-catalyzed solar photooxidation of iodide ion.* Journal of Molecular Catalysis A: Chemical, 2007. **265**(1): p. 153-158.
26. El Hajjouji, H., et al., *Photochemical UV/TiO2 treatment of olive mill wastewater (OMW).* Bioresource Technology, 2008. **99**(15): p. 7264-7269.
27. Kallel, M., et al., *Removal of organic load and phenolic compounds from olive mill wastewater by Fenton oxidation with zero-valent iron.* Chemical Engineering Journal, 2009. **150**(2): p. 391-395.
28. Lucas, M.S. and J.A. Peres, *Removal of COD from olive mill wastewater by Fenton's reagent: Kinetic study.* Journal of Hazardous Materials, 2009. **168**(2): p. 1253-1259.
29. Lee, E., et al., *Hydrogen peroxide interference in chemical oxygen demand during ozone based advanced oxidation of anaerobically digested livestock wastewater.* International Journal of Environmental Science & Technology, 2011. **8**(2): p. 381-388.

30. Bokare, A.D. and W. Choi, *Review of iron-free Fenton-like systems for activating H2O2 in advanced oxidation processes.* Journal of Hazardous Materials, 2014. **275**: p. 121-135.

31. Bigda, R.J., *Consider Fenton`s chemistry for wastewater treatment.* Chemical Engineering Progress, 1995. **91**: p. 62-66.

32. Mesquita, I., et al., *Treatment of azo dye-containing wastewater by a Fenton-like process in a continuous packed-bed reactor filled with activated carbon.* Journal of Hazardous Materials, 2012. **237-238**: p. 30-37.

33. Nidheesh, P.V., R. Gandhimathi, and S.T. Ramesh, *Degradation of dyes from aqueous solution by Fenton processes: a review.* Environ Sci Pollut Res Int, 2013. **20**(4): p. 2099-132.

34. Gazi, S., R. Ananthakrishnan, and N.D.P. Singh, *Photodegradation of organic dyes in the presence of [Fe(III)-salen]Cl complex and H2O2 under visible light irradiation.* Journal of Hazardous Materials, 2010. **183**(1-3): p. 894-901.

35. Ran, J., et al., *Synthesis, structures and photocatalytic properties of a mononuclear copper complex with pyridine-carboxylato ligands.* Inorganic Chemistry Communications, 2010. **13**(4): p. 526-528.

36. Babuponnusami, A. and K. Muthukumar, *Removal of phenol by heterogenous photo electro Fenton-like process using nano-zero valent iron.* Separation and Purification Technology, 2012. **98**: p. 130-135.

37. Fan, X., et al., *Fenton-like degradation of nalidixic acid with Fe3+/H2O2.* Environmental Science and Pollution Research, 2013. **20**(6): p. 3649-3656.

38. Maekawa, J., K. Mae, and H. Nakagawa, *Fenton•Cu2+ system for phenol mineralization.* Journal of Environmental Chemical Engineering, 2014. **2**(3): p. 1275-1280.

39. Ensing, B., F. Buda, and E.J. Baerends, *Fenton-like Chemistry in Water: Oxidation Catalysis by Fe(III) and H2O2.* The Journal of Physical Chemistry A, 2003. **107**(30): p. 5722-5731.

40. Català, M.S., A.C. Sevilla, and A.M.P. Roqué, *Herramientas de Trabajo Colaborativo. Elaboración de un Banco de Buenas Prácticas.* Procedia - Social and Behavioral Sciences, 2015. **196**: p. 198-205.

41. Lucas, M.S. and J.A. Peres, *Decolorization of the azo dye Reactive Black 5 by Fenton and photo-Fenton oxidation.* Dyes and Pigments, 2006. **71**(3): p. 236-244.

42. Heckert, E.G., S. Seal, and W.T. Self, *Fenton-Like Reaction Catalyzed by the Rare Earth Inner Transition Metal Cerium.* Environmental Science & Technology, 2008. **42**(13): p. 5014-5019.

43. Solomon, E.I., U.M. Sundaram, and T.E. Machonkin, *Multicopper Oxidases and Oxygenases.* Chemical Reviews, 1996. **96**(7): p. 2563-2606.

44. Yruela, I., *Copper in plants: acquisition, transport and interactions.* Functional Plant Biology, 2009. **36**(5): p. 409-430.

45. Rorabacher, D.B., *Electron Transfer by Copper Centers.* Chemical Reviews, 2004. **104**(2): p. 651-698.

46. Moffett, J.W. and R.G. Zika, *Measurement of copper(I) in surface waters of the subtropical Atlantic and Gulf of Mexico.* Geochimica et Cosmochimica Acta, 1988. **52**(7): p. 1849-1857.

47. Halliwell, B. and J.M.C. Gutteridge, *[1] Role of free radicals and catalytic metal ions in human disease: An overview*, in *Methods in Enzymology*. 1990, Academic Press. p. 1-85.

48. Donnelly, P.S., Z. Xiao, and A.G. Wedd, *Copper and Alzheimer's disease.* Current Opinion in Chemical Biology, 2007. **11**(2): p. 128-133.

49. Nieto-Juarez, J.I., et al., *Inactivation of MS2 coliphage in Fenton and Fenton-like systems: role of transition metals, hydrogen peroxide and sunlight.* Environmental Science & Technology, 2010. **44**(9): p. 3351-3356.

50. Miles, C.J. and P.L. Brezonik, *Oxygen consumption in humic-colored waters by a photochemical ferrous-ferric catalytic cycle.* Environmental Science & Technology, 1981. **15**(9): p. 1089-1095.

51. Bali, U. and B. Karagözoğlu, *Performance comparison of Fenton process, ferric coagulation and H2O2/pyridine/Cu(II) system for decolorization of Remazol Turquoise Blue G-133.* Dyes and Pigments, 2007. **74**(1): p. 73-80.

52. Dinius, R.H., *Kinetics of the reaction between 1,3-dihydroxybenzene, hydrogen peroxide and copper(II) ions.* Inorganica Chimica Acta, 1985. **99**(2): p. 217-221.

53. Gray, R.D., *Kinetics of oxidation of copper(I) by molecular oxygen in perchloric acid-acetonitrile solutions.* Journal of the American Chemical Society, 1969. **91**(1): p. 56-62.

54. Skounas, S., et al., *Kinetic Studies and Mechanism of Hydrogen Peroxide Catalytic Decomposition by Cu(II) Complexes with Polyelectrolytes Derived from L-Alanine and Glycylglycine.* Bioinorganic Chemistry and Applications, 2010. **2010**: p. 643120.

55. Verma, P., et al., *Copper–ligand complex for the decolorization of synthetic dyes.* Chemosphere, 2004. **57**(9): p. 1207-1211.

56. Lázaro Martínez, J.M., et al., *Studies on the activation of hydrogen peroxide for color removal in the presence of a new Cu(II)-polyampholyte heterogeneous catalyst.* Applied Catalysis B: Environmental, 2008. **82**(3): p. 273-283.

57. Masarwa, M., et al., *Reactions of low-valent transition-metal complexes with hydrogen peroxide. Are they "Fenton-like" or not? 1. The case of Cu+aq and Cr2+aq.* Journal of the American Chemical Society, 1988. **110**(13): p. 4293-4297.

58. Moss, G.P., P.A.S. Smith, and D. Tavernier, *Glossary of class names of organic compounds and reactivity intermediates based on structure (IUPAC Recommendations 1995).* Pure and Applied Chemistry, 1995. **67**(8-9): p. 1307-1375.

59. Schiff, H., *Mittheilungen aus dem Universitätslaboratorium in Pisa: Eine neue Reihe organischer Basen.* Justus Liebigs Annalen der Chemie, 1864. **131**(1): p. 118-119.

60. Fernández-G, J.M., et al., *The structures and cyclic voltammetry of three copper(II) complexes derived from bulky ortho-hydroxy Schiff bases.* Journal of Molecular Structure, 2002. **612**(1): p. 69-79.

61. Khandar, A.A. and K. Nejati, *Synthesis and characterization of a series of copper(II) complexes with azo-linked salicylaldimine Schiff base ligands.: Crystal structure of Cu5PHAZOSALTN·CHCl3.* Polyhedron, 2000. **19**(6): p. 607-613.

62. Md Yusof, E.N., et al., *Synthesis, Characterization and Biological Evaluation of Transition Metal Complexes Derived from N, S Bidentate Ligands.* International Journal of Molecular Sciences, 2015. **16**(5): p. 11034-11054.

63. Pedreño, E., et al., *Protecting or promoting effects of spermine on DNA strand breakage induced by iron or copper ions as a function of metal concentration.* Journal of Inorganic Biochemistry, 2005. **99**(10): p. 2074-2080.

64. Yoon, T.P. and E.N. Jacobsen, *Privileged Chiral Catalysts.* Science, 2003. **299**(5613): p. 1691-1693.

65. Dalia, S., et al., *A short review on chemistry of schiff base metal complexes and their catalytic application.* International Journal of Chemical Studies, 2018. **6**: p. 2859-2866.

66. Hunashal, R.D. and D. Satyanarayana, *One pot synthesis of 3-(substituted phenoxymethyl)-6-phenyl/substituted phenoxymethyl-1,2,4-triazolo[3,4-b][1,3,4] thiadiazole derivatives as antimicrobial agents.* International Journal of Pharma and Bio Sciences, 2012. **3**: p. 183-192.

67. Shivakumar, K., et al., *Synthesis, spectral characterization and biological activity of benzofuran Schiff bases with Co(II), Ni(II), Cu(II), Zn(II), Cd(II) and Hg(II) complexes.* Journal of Coordination Chemistry, 2008. **61**(14): p. 2274-2287.

68. Tarafder, M., et al., *Complexes of a tridentate ONS Schiff base. Synthesis and biological properties.* Transition Metal Chemistry, 2000. **25**: p. 456-460.

69. Faber, P., A. Ronald, and B.W. Millar, *Methylthioninium chloride: pharmacology and clinical applications with special emphasis on nitric oxide mediated vasodilatory shock during cardiopulmonary bypass.* Anaesthesia, 2005. **60**(6): p. 575-587.

70. WIKLUND, L., et al., *Neuro- and Cardioprotective Effects of Blockade of Nitric Oxide Action by Administration of Methylene Blue.* Annals of the New York Academy of Sciences, 2007. **1122**(1): p. 231-244.

71. Ghosh, D. and K.G. Bhattacharyya, *Adsorption of methylene blue on kaolinite.* Applied Clay Science, 2002. **20**(6): p. 295-300.

72. Schirmer, R.H., et al., *Methylene blue as an antimalarial agent.* Redox Report,

2003. **8**(5): p. 272-275.

73. Oz, M., et al., *Cellular and molecular actions of Methylene Blue in the nervous system.* Medicinal research reviews, 2011. **31**(1): p. 93-117.

74. Cawein, M., et al., *Hereditary Diaphorase Deficiency and Methemoglobinemia.* Archives of Internal Medicine, 1964. **113**(4): p. 578-585.

75. Appavu, B., et al., *BiVO4 /N-rGO nano composites as highly efficient visible active photocatalyst for the degradation of dyes and antibiotics in eco system.* Ecotoxicology and Environmental Safety, 2018. **151**: p. 118-126.

76. Bhuvaneswari, K., et al., *Photocatalytic Performance on Visible Light Induced ZnS QDs-MgAl Layered Double Hydroxides Hybrids for Methylene Blue Dye Degradation.* ChemistrySelect, 2018. **3**(47): p. 13419-13426.

77. Deriase, S.F., et al., *Statistical optimization of photocatalytic degradation process of methylene blue dye by SnO–TiO2–AC composite using response surface methodology.* Environmental Progress & Sustainable Energy. **n/a**(n/a): p. e13639.

78. Ji, Z., et al., *Enhanced Photocatalytic Activity of ZnO Toward the Degradation of Methylene Blue Dye: Effects of Fe3+ and Sn4+ Doping.* physica status solidi (a), 2019. **216**(7): p. 1800947.

79. Kumar Venkatraman, S., et al., *Photocatalytic Degradation of Methylene Blue Dye by Calcium-and Magnesium-Based Silicate Ceramics.* ChemistrySelect, 2020. **5**(39): p. 12198-12205.

80. Parangusan, H., et al., *Nanoflower-like Yttrium-doped ZnO Photocatalyst for the Degradation of Methylene Blue Dye*. Photochemistry and Photobiology, 2018. **94**(2): p. 237-246.

81. Yuan, W., et al., *In situ synthesis and immobilization of a Cu(ii)–pyridyl complex on silica microspheres as a novel Fenton-like catalyst for RhB degradation at near-neutral pH*. RSC Advances, 2017. **7**(37): p. 22825-22835.

82. Watanabe, T., K. Koller, and K. Messner, *Copper-dependent depolymerization of lignin in the presence of fungal metabolite, pyridine.* Journal of Biotechnology, 1998. **62**(3): p. 221-230.

83. Nerud, F., et al., *Decolorization of synthetic dyes by the Fenton reagent and the Cu/pyridine/H2O2 system.* Chemosphere, 2001. **44**(5): p. 957-961.

84. Shah, V., et al., *Decolorization of dyes with copper(II)/organic acid/hydrogen peroxide systems.* Applied Catalysis B: Environmental, 2003. **46**(2): p. 287-292.

85. Bali, U. and B. Karagözoğlu, *Decolorization of Remazol-Turquoise Blue G-133 and other dyes by Cu(II)/pyridine/H2O2 system.* Dyes and Pigments, 2007. **73**(2): p. 133-140.

86. Gemeay, A.H., et al., *Kinetics and mechanism of the heterogeneous catalyzed oxidative degradation of indigo carmine.* Journal of Molecular Catalysis A: Chemical, 2003. **193**(1): p. 109-120.

87. Gemeay, A.H., et al., *Catalytic effect of supported metal ion complexes on the*

induced oxidative degradation of pyrocatechol violet by hydrogen peroxide. Journal of Colloid and Interface Science, 2003. **263**(1): p. 228-236.

88. Gemeay, A.H., et al., *Kinetics of the oxidative degradation of thionine dye by hydrogen peroxide catalyzed by supported transition metal ions complexes.* Journal of Chemical Technology & Biotechnology, 2004. **79**(1): p. 85-96.

89. Li, J.-M., et al., *Oxidation of 4-chlorophenol catalyzed by Cu(II) complexes under mild conditions: Kinetics and mechanism.* Journal of Molecular Catalysis A: Chemical, 2009. **299**(1): p. 102-107.

90. Baldrian, P., et al., *Degradation of polycyclic aromatic hydrocarbons by hydrogen peroxide catalyzed by heterogeneous polymeric metal chelates.* Applied Catalysis B: Environmental, 2005. **59**(3): p. 267-274.

91. Ray, S., S.F. Mapolie, and J. Darkwa, *Catalytic hydroxylation of phenol using immobilized late transition metal salicylaldimine complexes.* Journal of Molecular Catalysis A: Chemical, 2007. **267**(1): p. 143-148.

92. Baldrian, P., et al., *Synthesis of zirconia-immobilized copper chelates for catalytic decomposition of hydrogen peroxide and the oxidation of polycyclic aromatic hydrocarbons.* Chemosphere, 2008. **72**(11): p. 1721-1726.

93. Fei, B.-L., et al., *Simple Copper(II) Schiff Base Complex as Efficient Heterogeneous Photo-Fenton-like Catalyst.* Chemistry Letters, 2014. **43**(7): p. 1158-1160.

94. Fei, B.-L., et al., *Green Oxidative Degradation of Methyl Orange with Copper(II) Schiff Base Complexes as Photo-Fenton-Like Catalysts.* Zeitschrift für anorganische und allgemeine Chemie, 2014. **640**(10): p. 2035-2040.

95. Solomon Legese Hailu, B.U.N., Mesfin Redi-Abshiro, Isabel Diaz, Rathinam Aravindhan, Merid Tessema, *Oxidation of 4-chloro-3-methylphenol using zeolite Y-encapsulated iron(III)-, nickel(II)-, and copper(II)-N,N'-disalicylidene- 1,2-phenylenediamine complexes.* Chinese Journal of Catalysis, 2016. **37**(1): p. 135-145.

96. Rao, K.S., et al., *A novel method for synthesis of silica nanoparticles.* Journal of Colloid and Interface Science, 2005. **289**(1): p. 125-131.

97. Hernández-Morales, V., et al., *Adsorption of lead (II) on SBA-15 mesoporous molecular sieve functionalized with –NH2 groups.* Microporous and Mesoporous Materials, 2012. **160**: p. 133–142.

98. Ishibashi, K.-i., et al., *Detection of active oxidative species in TiO2 photocatalysis using the fluorescence technique.* Electrochemistry Communications, 2000. **2**(3): p. 207-210.

99. Náfrádi, M., et al., *Application of coumarin and coumarin-3-carboxylic acid for the determination of hydroxyl radicals during different advanced oxidation processes.* Radiation Physics and Chemistry, 2020. **170**: p. 108610.

100. Talukdar, S. and R.K. Dutta, *A mechanistic approach for superoxide radicals and singlet oxygen mediated enhanced photocatalytic dye degradation by selenium doped ZnS nanoparticles.* RSC Advances, 2016. **6**(2): p. 928-936.

101. Wang, J., et al., *Two-Phase Synthesis of Monodisperse Silica Nanospheres with Amines or Ammonia Catalyst and Their Controlled Self-Assembly.* ACS Applied Materials & Interfaces, 2011. **3**(5): p. 1538-1544.

102. Koźlecki, T., et al., *Improved Synthesis of Nanosized Silica in Water-in-Oil Microemulsions.* Journal of Nanoparticles, 2016. **2016**: p. 1-9.

103. Al-Noor, T., L. Abdul Karem, and f. Alsalami, *Schiff Base And Ligand Metal Complexes of Some Amino Acids and Drug*. 2016.

104. Bose, A., R.K. Gilpin, and M. Jaroniec, *Adsorption and Thermogravimetric Studies of Mesoporous Silica Coated with Siloxane Polymer.* Journal of Colloid and Interface Science, 2001. **240**(1): p. 224-228.

105. Morrow, B.A., I.A. Cody, and L.S.M. Lee, *Infrared studies of reactions on oxide surfaces. 7. Mechanism of the adsorption of water and ammonia on dehydroxylated silica.* The Journal of Physical Chemistry, 1976. **80**(25): p. 2761-2767.

106. Peri, J.B., *Infrared Study of Adsorption of Carbon Dioxide, Hydrogen Chloride, and Other Molecules on "Acid" Sites on Dry Silica—Alumina and γ-Alumina1*. The Journal of Physical Chemistry, 1966. **70**(10): p. 3168-3179.

107. Hentschke, R., C. Ballnus, and J. Meyer, *Remarks on the Interpretation of IR-Absorption Studies Applied to the Surfaces of Silica Nanoparticles.* The Journal of Physical Chemistry C, 2016. **120**(17): p. 9229-9235.

108. Jal, P., et al., *Synthesis and characterization of nanosilica prepared by precipitation method.* Colloids and Surfaces A-physicochemical and Engineering Aspects - COLLOID SURFACE A, 2004. **240**: p. 173-178.

109. Bell, R.J., N.F. Bird, and P. Dean, *The vibrational spectra of vitreous silica, germania and beryllium fluoride.* Journal of Physics C: Solid State Physics, 1968. **1**(2): p. 299-303.

110. Boccuzzi, F., et al., *Infrared study of surface modes on silica.* The Journal of Physical Chemistry, 1978. **82**(11): p. 1298-1303.

111. Morrow, B.A. and A.J. McFarlan, *Surface vibrational modes of silanol groups on silica.* The Journal of Physical Chemistry, 1992. **96**(3): p. 1395-1400.

112. Morrow, B.A. and S.J. Lang, *Infrared and Solid-State NMR Studies of the Adsorption of PMe2Cl on Silica.* The Journal of Physical Chemistry, 1994. **98**(50): p. 13319-13322.

113. Benesi, H.A. and A.C. Jones, *An Infrared Study of the Water-Silica Gel System.* The Journal of Physical Chemistry, 1959. **63**(2): p. 179-182.

114. Fukui, K.-i., H. Miyauchi, and Y. Iwasawa, *Highly sensitive detection of adsorbed species on a SiO2 surface by reflection-absorption infrared spectroscopy.* Chemical Physics Letters, 1997. **274**(1): p. 133-139.

115. Orcel, G., J. Phalippou, and L.L. Hench, *Structural changes of silica xerogels during low temperature dehydration.* Journal of Non-Crystalline Solids, 1986. **88**(1): p. 114-130.

116. Valle, R.G.D. and A. Brillante, *Lattice dynamics of halogenated anthracene derivatives under pressure.* The Journal of Chemical Physics, 1994. **100**(10): p. 7640-7647.

117. Wilson, M., et al., *Polarization Effects, Network Dynamics, and the Infrared Spectrum of Amorphous ${\mathrm{SiO}}_{2}$.* Physical Review Letters, 1996. **77**(19): p. 4023-4026.

118. Sarnthein, J., A. Pasquarello, and R. Car, *Origin of the High-Frequency Doublet in the Vibrational Spectrum of Vitreous SiO<sub>2</sub&gt.* Science, 1997. **275**(5308): p. 1925.

119. Taraskin, S.N. and S.R. Elliott, *Nature of vibrational excitations in vitreous silica.* Physical Review B, 1997. **56**(14): p. 8605-8622.

120. Brinker, J. and W. Sherer, *Sol–Gel Science, The Physics and Chemistry of Sol–Gel Processing*. 1990: New York: Academic Press. Chapter 9.

121. Chen, K., et al., *Model construction of micro-pores in shale: A case study of Silurian Longmaxi Formation shale in Dianqianbei area, SW China.* Petroleum Exploration and Development, 2018. **45**: p. 412-421.

122. Lee, H. and J. Yi, *REMOVAL OF COPPER IONS USING FUNCTIONALIZED MESOPOROUS SILICA IN AQUEOUS SOLUTION*. Separation Science and Technology, 2001. **36**(11): p. 2433-2448.

123. Bogush, G.H., M.A. Tracy, and C.F. Zukoski, *Preparation of monodisperse silica particles: Control of size and mass fraction.* Journal of Non-Crystalline Solids, 1988. **104**(1): p. 95-106.

124. Green, D.L., et al., *Size, volume fraction, and nucleation of Stober silica nanoparticles.* Journal of Colloid and Interface Science, 2003. **266**(2): p. 346-358.

125. Huang, L., et al., *Preparation and controlled drug delivery applications of mesoporous silica polymer nanocomposites through the visible light induced surface-initiated ATRP*. Applied Surface Science, 2017. **412**: p. 571-577.

126. Blinov, A.V., et al., *Influence of the dispersion medium type in the sol-gel synthesis of silicon dioxide.* AIP Conference Proceedings, 2019. **2188**(1): p. 040012.

127. Joseph, G., *Scanning Electron Microscopy and X-Ray Microanalysis*, ed. 3. 2003: Springer US.

128. Abouliatim, Y., et al., *Optical characterization of stereolithography alumina suspensions using the Kubelka–Munk model.* Journal of the European Ceramic Society, 2009. **29**(5): p. 919-924.

129. Bayazit, M.K., et al., *Pyridine-Functionalized Single-Walled Carbon Nanotubes as Gelators for Poly(acrylic acid) Hydrogels.* Journal of the American Chemical Society, 2010. **132**(44): p. 15814-15819.

130. Silva, Ana R., et al., *Anchoring of Copper(II) Acetylacetonate onto an Activated Carbon Functionalised with a Triamine.* European Journal of Inorganic

Chemistry, 2004. **2004**(10): p. 2027-2035.

131. Technologies, P., *Diffuse Reflectance – Theory and Applications*. 2017.

132. CORPORATION, S., *Measurements of Band Gap in Compound Semiconductors - Band Gap Determination from Diffuse Reflectance Spectra.*

133. Habibi, M.H. and M.H. Rahmati, *Fabrication and characterization of ZnO@CdS core–shell nanostructure using acetate precursors: XRD, FESEM, DRS, FTIR studies and effects of cadmium ion concentration on band gap.* Spectrochimica Acta Part A: Molecular and Biomolecular Spectroscopy, 2014. **133**: p. 13-18.

134. Dimos, K., et al., *Naphthalene-based periodic nanoporous organosilicas: I. Synthesis and structural characterization.* Microporous and Mesoporous Materials, 2012. **158**: p. 324-331.

135. Pehkonen, S.O., R.L. Siefert, and M.R. Hoffmann, *Photoreduction of Iron Oxyhydroxides and the Photooxidation of Halogenated Acetic Acids.* Environmental Science & Technology, 1995. **29**(5): p. 1215-1222.

136. Pulgarin, C. and J. Kiwi, *Iron Oxide-Mediated Degradation, Photodegradation, and Biodegradation of Aminophenols.* Langmuir, 1995. **11**(2): p. 519-526.

137. Pahang, F., et al., *Fluorescence properties of methylene blue molecules coupled with metal oxide nanoparticles.* OSA Continuum, 2020. **3**(3): p. 688-697.

138. Tardivo, J.P., et al., *Methylene blue in photodynamic therapy: From basic mechanisms to clinical applications.* Photodiagnosis and Photodynamic Therapy, 2005. **2**(3): p. 175-191.

139. Zhuang, J., et al., *Photocatalytic Degradation of RhB over TiO2 Bilayer Films: Effect of Defects and Their Location.* Langmuir, 2010. **26**(12): p. 9686-9694.

140. Zhou, W., et al., *Influence of a reagents addition strategy on the Fenton oxidation of rhodamine B: control of the competitive reaction of ·OH.* RSC Advances, 2016. **6**(110): p. 108791-108800.

141. Grieser, F., *Free radical formation and scavenging by solutes in the sonolysis of aqueous solutions.* Proceedings of Meetings on Acoustics, 2013. **19**(1): p. 045093.

142. Kwon, B.G., J.-O. Kim, and J.-K. Kwon, *An Advanced Kinetic Method for HO2·/O2-· Determination by Using Terephthalate in the Aqueous Solution.* Environmental Engineering Research, 2012. **17**(4): p. 205-210.

143. Pelaez, M., et al., *Use of selected scavengers for the determination of NF-TiO2 reactive oxygen species during the degradation of microcystin-LR under visible light irradiation.* Journal of Molecular Catalysis A: Chemical, 2016. **425**: p. 183-189.

144. Fernández-Castro, P., et al., *Insight on the fundamentals of advanced oxidation processes. Role and review of the determination methods of reactive oxygen species.* Journal of Chemical Technology & Biotechnology, 2015. **90**(5): p. 796-820.

145. Kaur, S. and V. Singh, *Visible light induced sonophotocatalytic degradation of Reactive Red dye 198 using dye sensitized TiO2.* Ultrasonics Sonochemistry, 2007. **14**(5): p. 531-537.

146. Xiao, J., et al., *Superoxide radical-mediated photocatalytic oxidation of phenolic compounds over Ag+/TiO2: Influence of electron donating and withdrawing substituents.* Journal of Hazardous Materials, 2016. **304**: p. 126-133.

147. Wysocka, I., et al., *UV-Vis-Induced Degradation of Phenol over Magnetic Photocatalysts Modified with Pt, Pd, Cu and Au Nanoparticles.* Nanomaterials, 2018. **8**(1): p. 28.

148. Rao, P.S. and E. Hayon, *Experimental determination of the redox potential of the superoxide radical •O2−.* Biochemical and Biophysical Research Communications, 1973. **51**(2): p. 468-473.

149. Li, J., et al., *Recent advances in Cu-Fenton systems for the treatment of industrial wastewaters: Role of Cu complexes and Cu composites.* Journal of Hazardous Materials, 2020. **392**: p. 122261.